

Anisotropic plasmonic nanoparticle arrays for surface-enhanced biosensors

vorgelegt von
Master of Science (M. Sc.)
Dimitra Gkogkou
aus Komotini, Griechenland

Von der Fakultät II – Mathematik und Naturwissenschaften
der Technischen Universität Berlin
zur Erlangung des akademischen Grades

Doktor der Naturwissenschaften
Dr. rer. nat.
genehmigte Dissertation

Promotionsausschuss:

Vorsitzende: Prof. Dr. Birgit Kanngießer (Technische Universität Berlin)
Gutachter: Prof. Dr. Norbert Esser (Technische Universität Berlin)
Gutachter: Prof. Dr. Peter Hildebrandt (Technische Universität Berlin)
Gutachterin: Prof. Dr. Janina Kneipp (Humboldt-Universität zu Berlin)

Tag der wissenschaftlichen Aussprache: 12 May 2017

Berlin 2017

“Nothing in life is to be feared, it is only to be understood. Now is the time to understand more, so that we may fear less.”

Marie Curie

Abstract

Plasmonic structures exhibiting surface enhancement properties can lead to hypersensitive, label-free and analyte-specific detection of organic molecules. The motivation of this work is the realization and study of optically anisotropic plasmonic substrates for combining SERS (surface enhanced Raman scattering) and SEIRA (surface enhanced infrared absorption) spectroscopy. These properties can be ultimately used for chemical- and bio-sensing purposes.

Silver was deposited on pre-patterned rippled silicon surface, with ripple periodicity in the range of 40-50 nm. The silver nanoparticles grow preferentially in the direction along the ripples forming arrays. The structural anisotropy introduces optical anisotropy, investigated with ellipsometry. A smaller, narrower resonance appears in the direction across the ripples and a red-shifted, stronger and broader resonance in the direction along the ripples. Chemical functionalization was achieved by the adsorption of the 4-mercaptobenzonitrile (4-MBN) self-assembled monolayer (SAM) to the silver surface.

The position of the plasmonic resonances can be tuned by controlling the size and aspect ratio of the nanoparticles. One combination involves both of the resonances in the visible range, employed for SERS. SERS measurements at varying excitation wavelengths and polarization angles, exhibited a sinusoidal profile of the 4-MBN peak intensity. The signal modulates according to the polarization angle and laser wavelength, exciting the respective resonances. The SERS polarization dependency has been confirmed up to the NIR range. It was applied for the signal differentiation between surface-attached molecules (4-MBN) and solution molecules (cyclohexane), demonstrating potential sensing uses. The SERS enhancement factors were estimated to be in the range of 10^4 . A second combination involves both resonances red-shifted to the MIR region demonstrating considerable SEIRA properties. The enhancement factor was estimated to be 170, with the peaks exhibiting a Fano-shaped profile. IR ellipsometry and IR polarized microscopy demonstrated the polarization dependence, according to the excitation direction, of the SEIRA activity. The combination of this type of substrate and characterization techniques introduces new possibilities in the structural characterization of molecules with high sensitivity. The third combination involves the resonance in the direction across the ripples peaking in the visible range and the resonance in the direction along the ripples peaking in the NIR. Due to broadening, the longitudinal resonance extends to the MIR enhancing the vibrational signal and potentially allowing the dual detection of SERS and SEIRA on a single spot.

An additional method for the combination of SERS and SEIRA properties on a single substrate is proposed by the evaporation of a silver layer of gradient thickness on silicon. The variation of the surface morphology and therefore optical activity along the sample, results in SERS and SEIRA active areas. The proximity of these sites can be controlled by the deposition parameters. The presented gradient thickness substrate is an alternative solution for combined SERS and SEIRA detection by performing a line scan.

The presented results demonstrate the controlled design and characterization of plasmonic nanostructures with specific surface enhancement properties and investigate their potential bio-sensing applications. The combined SERS and SEIRA properties allow for acquisition of the maximum vibrational information of an analyte in high sensitivity and selectivity.

Zusammenfassung

Plasmonische Strukturen mit oberflächen-verstärkenden Eigenschaften ermöglichen die hypersensitive, label-freie und analyten-spezifische Detektion von organischen Molekülen. Die Motivation dieser Arbeit ist die Realisierung und Untersuchung von optisch anisotropen plasmonischen Substraten für kombinierte SERS (oberflächen-verstärkte Raman Streuung) und SEIRA (oberflächen-verstärkte Infrarot Absorption) Spektroskopie. Diese Eigenschaften sollen im Fernziel in chemischen und bio-sensorischen Anwendungen verwendet werden.

Silber wurde auf vorstrukturierte wellige Siliziumoberflächen, mit einer Periode von 40-50 nm, aufgedampft. Hierbei lagern sich die Silberatome bevorzugt entlang der Wellen an und formen Reihen von Nanopartikeln. Die strukturelle Anisotropie bedingt eine optische Anisotropie, wie durch ellipsometrische Messungen gezeigt wurde. Die ellipsometrischen Messungen zeigen eine schwächere, schmalere Resonanz quer zu den Wellen und eine rotverschobene, stärkere und breitere Resonanz in Richtung der Wellen. Eine chemische Funktionalisierung der Silberoberfläche wurde durch die Formierung einer selbst-organisierten Monolage (SAM) vom 4-Mercaptobenzonitril (4-MBN) erzielt.

Durch die Kontrolle der Partikelgröße und des Aspektverhältnisses kann die Position der plasmonischen Resonanzen gezielt eingestellt werden. In einer Anwendung für SERS finden solche Substrate, bei denen beide Resonanzen im sichtbaren Spektralbereich liegen eine Anwendung. SERS Messungen wurden unter Variation der Wellenlänge und der Polarisationsrichtung relativ zu der Wellenorientierung des Anregungslasers durchgeführt und zeigen eine sinusförmiges Profil in der Peak-Intensität des 4-MBN. Die Signalmodulation ist hierbei mittels der angeregten Resonanzen direkt mit dem Polarisationswinkel bzgl. der Wellenorientierung und der Laserwellenlänge gekoppelt. Diese Abhängigkeit des SERS Signals von der Polarisation konnte bis in den nahinfraroten Spektralbereich (NIR) gezeigt werden. Als Anwendungsbeispiel für mögliche Sensoranwendungen wurde diese Eigenschaft genutzt um eine Differenzierung zwischen oberflächen-gebundenen Molekülen (4-MBN) und Molekülen in der Lösung (Cyclohexan) demonstriert. Der durch die beschriebenen Substrate erzielte SERS-Verstärkungsfaktor wurde zu 10^4 abgeschätzt.

In einer zweiten Probengeometrie wurde ein Substrat verwendet bei dem die Resonanz quer zu den Wellen ihr Maximum im sichtbaren und die Resonanz entlang der Wellen ihr Maximum im NIR aufweisen. Auf Grund ihrer starken Verbreiterung erstreckt sich die Resonanz entlang der Wellen bis in den MIR-Bereich und führt daraus resultierend zu einer Verstärkung der vibronischen Signale in diesem Spektralbereich. Eine solche Geometrie kann für die duale Detektion von SERS und SEIRA an einer einzelnen Position eingesetzt werden. Mittels IR Ellipsometrie und polarisationsabhängige IR-Mikroskopie konnte die Polarisationsabhängigkeit der SEIRA Aktivität entsprechen der Anregungsrichtungen gezeigt werden.

Bei der dritten Probengeometrie wurden beide Resonanzen mittels geometrie-abhängiger Rotverschiebung in den MIR-Bereich verschoben. Diese Probengeometrie ermöglicht die Realisierung von nennenswerten SEIRA Eigenschaften mit einem abgeschätzten Verstärkungsfaktor von 170 und einer für SEIRA Experimenten typischen Fano-Form der Vibrationsbanden.

Eine alternativ vorgeschlagene Methode um SERS und SEIRA Eigenschaften auf einem Substrat zu erzielen, wird durch die Deposition einer Silber-Schicht mit einem Schichtdickengradienten realisiert. Die Variation der Oberflächenmorphologie und daraus resultierend der optischen Aktivität entlang des Gradienten resultiert sowohl in einem SERS als auch in einem SEIRA aktiven Bereich auf der Probe. Der Abstand zwischen diesen Bereichen kann dabei mittels der Depositionsparameter kontrolliert werden. Diese Gradienten-Substrate stellen somit einen alternativen Ansatz für die kombinierte SERS und SEIRA Messung durch Variation der Messposition da.

Die gezeigten Ergebnisse zeigen eine Möglichkeit eines rationalen Designs von plasmonischen Nanostrukturen und die Charakterisierung selbiger mit spezifischen oberflächen-verstärkenden Eigenschaften und untersuchen ihre potentiellen Einsatzmöglichkeiten für Biosensoranwendungen.

Publications

Parts of this work are published in the following articles and reprinted with permission:

D. Gkogkou, T. Shaykhutdinov, T.W.H Oates, U. Gernert, B. Schreiber, S. Facsko, P. Hildebrandt, I. Weidinger, N. Esser, K. Hinrichs, '[Characterization of anisotropic silver nanoparticle arrays via spectroscopic ellipsometry supported by numerical optical modeling](#)', *Applied Surface Science* (In Press, Available online 19 October 2016).

DOI: 10.1016/j.apsusc.2016.10.105.

D. Gkogkou, B. Schreiber, T. Shaykhutdinov, H.K. Ly, U. Kuhlmann, U. Gernert, S. Facsko, P. Hildebrandt, N. Esser, K. Hinrichs, I. Weidinger, T.W.H Oates, '[Polarization- and Wavelength-Dependent Surface-Enhanced Raman Spectroscopy Using Optically Anisotropic Rippled Substrates for Sensing](#)', *ACS Sensors*, 1 (2016), 318-23. DOI: 10.1021/acssensors.5b00176.

Contributions at academic conferences

D. Gkogkou, T. Shaykhutdinov, P. Hildebrandt, N. Esser, K. Hinrichs, T.W.H. Oates, I.M. Weidinger, 'Ellipsometric Vis and IR characterization of anisotropic plasmonic Ag nanoparticle arrays for biosensing', 7th International Conference on Spectroscopic Ellipsometry (ICSE-7), June 2016, Poster presentation.

D. Gkogkou, T. Shaykhutdinov, P. Hildebrandt, N. Esser, K. Hinrichs, I.M. Weidinger, 'SERS substrates with optically anisotropic properties for analytical applications', Horiba International RamanFest 2016, May 2016, Poster presentation.

D. Gkogkou, P. Hildebrandt, N. Esser, K. Hinrichs, T.W.H. Oates, I.M. Weidinger, 'Anisotropic nanoparticle arrays for SERS and SEIRA detection', 2nd International Conference on Enhanced Spectroscopies-ICES, Oct. 2015, Oral presentation.

D. Gkogkou, H.K.Ly, P. Hildebrandt, K. Hinrichs, N. Esser, I.M. Weidinger, T.W.H. Oates, 'Ellipsometric Characterization Of Metal Island Films For Surface- Enhanced Substrates', 9th Ellipsometry Workshop, Twente, the Netherlands, Feb. 2015, Poster presentation.

D. Gkogkou, I.M. Weidinger, H.K.Ly, P. Hildebrandt, K. Hinrichs, N. Esser, T.W.H. Oates, 'Combinatorial Investigation of Silver Island Films as SERS and SEIRA Substrates', Surface-Enhanced Spectroscopies, Chemnitz, Aug. 2014, Poster presentation.

D. Gkogkou, I.M. Weidinger, H.K.Ly, P. Hildebrandt, K. Hinrichs, N. Esser, T.W.H. Oates, 'Spectroscopic Ellipsometry Characterization of Plasmonic Films for Surface Enhanced Sensors', Poster, 8th Workshop Ellipsometry, Dresden, May 2014, Poster presentation.

Table of Contents

| | |
|--|----|
| Abstract | I |
| Publications | V |
| Abbreviations..... | IX |
| 1 Introduction and motivation | 1 |
| 2 Theoretical introduction | 5 |
| 2.1.1 Refractive index | 5 |
| 2.1.2 Light polarization | 6 |
| 2.2 Ellipsometry | 8 |
| 2.2.1 Oscillator models..... | 10 |
| 2.3 Plasmonics | 11 |
| 2.4 Vibrational spectroscopy | 14 |
| 2.4.1 Raman scattering..... | 16 |
| 2.4.2 Infrared absorption | 21 |
| 2.5 Thin metal film growth | 24 |
| 2.6 Rippled silicon substrates..... | 25 |
| 3 Experimental setup | 27 |
| 3.1 Thermal evaporation | 27 |
| 3.2 Self-assembled monolayer | 28 |
| 3.3 Ellipsometry | 28 |
| 3.4 Raman scattering spectroscopy | 28 |
| 3.5 Infrared spectroscopy setup..... | 29 |
| 3.6 Topographic characterization..... | 30 |
| 3.7 Enhancement factor calculations..... | 31 |
| 4 Enhancement substrates..... | 35 |
| 4.1.1 Silver deposition on plain silicon..... | 35 |
| 4.1.2 Silver deposition on rippled silicon | 38 |
| 4.2 Optical properties | 41 |
| 5 Self-assembled monolayer | 46 |
| 6 Optical characterization of anisotropic nanoparticle arrays..... | 48 |
| 6.1 Ellipsometry supported by computational electromagnetic calculations | 48 |
| 6.2 Raman scattering..... | 55 |
| 6.3 Infrared absorption..... | 67 |
| 7 Gradient thickness silver islands as unified SERS and SEIRA substrates..... | 76 |

| | | |
|----|---|-----|
| 8 | Conclusions and outlook | 88 |
| 9 | Bibliography..... | 92 |
| 10 | Appendix | 102 |
| | 10.1.1 Supplementary graphs to Chapter 7 | 102 |
| | 10.1.2 EF calculation of Chapter 7 | 103 |
| 11 | List of figures | 105 |
| | Acknowledgments..... | 109 |
| | Statement of authorship | 111 |

Abbreviations

| | |
|-------|---|
| AFM | Atomic Force Microscopy |
| BT | Benzenethiol |
| DMSO | Dimethyl sulfoxide |
| EF | Enhancement Factor |
| EMA | Effective Medium Approximation |
| FDTD | Finite-difference Time-domain |
| FFT | Fast Fourier Transformation |
| FTIR | Fourier Transform Infrared spectroscopy |
| GE | Generalized Ellipsometry |
| LSPR | Localized Surface Plasmon Resonance |
| 4-MBN | 4-mercaptobenzonitrile |
| MME | Mueller Matrix Ellipsometry |
| MSE | Mean Squared Error |
| OPA | Optical Plane Aperture |
| RCWA | Rigorous Coupled Wave Analysis |
| RF | Roughness Factor |
| SAM | Self-Assembled Monolayer |
| SEM | Scanning Electron Microscopy |
| SEIRA | Surface Enhanced Infrared Absorption |
| SERRS | Surface Enhanced Resonance Raman Scattering |
| SERS | Surface Enhanced Raman Scattering |
| SPP | Surface Plasmon Polariton |

1 Introduction and motivation

In the last few decades, biomedical sciences are moving towards an era of miniaturization and high performance. Specifically, medical diagnostics aim at increasing the sensitivity of analytical systems while decreasing their size, targeting for portable and versatile devices, e.g. lab-on-a-chip microfluidic cells [1]. Such an analytical setup, which measures chemical response in a biological system is called a biosensor [2, 3]. Apart from medical diagnostics, the use of biosensors serves analytical purposes in pharma industry, food safety, environmental control and defense. Due to a broad area of (bio)sensing applicability, there is a high demand for improvement of the detection limits and selectivity for target analytes while reducing the interaction area to the nano scale.

Depending on the transducing process, biosensors can be broadly classified as electrochemical, optical and the less common mechanical, acoustic and calorimetric types [4]. Electrochemical biosensors are the most prevalent type in the diagnostics market where the best example is that of the glucose electrochemical sensor, which revolutionized patient monitoring [5, 6]. Optical biosensors involve an optical transducer detecting changes in the optical properties induced by the analyte. A common application is that of surface plasmon resonance (SPR), utilized e.g. on prisms in order to detect the changes of refractive index when the analyte is bound to the surface [7].

The targeted downscaling of optical biosensors is effectively achieved with the utilization of localized surface plasmon resonances (LSPR). Detection limits have been dramatically increased by the use of localized plasmons, allowing even single molecule detection in the case of surface enhanced Raman scattering (SERS) [8]. In the light of these remarkable enhancing properties of the LSPR structures, a great amount of research is performed towards the rational fabrication of plasmonic nanostructures with tailored optical properties [9] and their application in vibrational spectroscopy techniques, specifically surface enhanced Raman scattering (SERS) and surface enhanced infrared absorption (SEIRA). Raman scattering and infrared absorption provide chemical fingerprints of the molecule due to its characteristic vibrational energy levels. The two techniques are complementary due to different selection rules and, when combined, can provide valuable information for the identification of molecules [10].

The aim of the present thesis is to elucidate the possibilities of preparing an optical sensor with tunable LSPR properties to allow for SERS and SEIRA detection of an analyte on a single substrate. The prepared rippled silicon substrates guide the formation of silver nanoparticle arrays along the ripples, thus introducing optical anisotropy that can be optimized for SEIRA in one excitation direction and for SERS in the perpendicular direction. The ultimate goal is to attain complete vibrational information of an analyte in ultra-low concentrations by measuring a single position with Raman and then changing the polarization and excitation wavelength to attain IR signals. Even though the technical status quo does not include a unified Raman and IR setup, the present thesis is a proof of concept that this combined approach is feasible and the substrate can be used in separate setups until such instrumentation is available. Furthermore, properties deriving from the optical anisotropy introduce additional prospects in polarized and wavelength dependent SERS

and polarized IR absorption measurements. Moreover, an alternative unifying substrate is presented, in which silver nanoislands of gradient thickness present variable SERS and SEIRA properties along the surface. This versatile substrate lacks the polarization dependency, but can provide areas with combined and separated SERS and SEIRA properties that can fit to different experimental demands.

The proposed method of fabrication, both of tunable nanoarrays as well as of gradient thickness nanoislands, provides a biosensing platform that occupies the middle ground between plasmonic enhancement control and cost/time efficiency. The current platforms vary from sophisticated cost-demanding structures produced by electron-beam lithography [11, 12] and elaborate arrangements of nanoparticle dimers with the help of origami DNA [13] to cheaper but harder-to-tune colloidal aggregates [14]. In spite of the growing research in SERS and SEIRA over the recent years, rarely were substrates tailored for use in both techniques [15-17]. The present thesis is a contribution to this specific field. The results presented examine the case of label-free detection [18], where a silver surface is functionalized by a self-assembled monolayer (SAM). The SAM molecules contain thiol groups on one side, which bind to the silver, and a functional group on the other side, through which immobilization via electrostatic or covalent binding of biomolecules can occur [19, 20]. In principle, the same substrate could be used in combination with fluorescent dyes for label enhanced sensing [21].

The thesis is composed of eight chapters which are organized as follows: Part A, including chapters 2 and 3, introduces the theoretical background of this work and in part B, including chapters 4-8, the results are presented and discussed. Chapter 2 presents basic light properties, the concept of ellipsometry, plasmonics and the mechanisms of (surface enhanced) vibrational spectroscopic methods, while a brief description of the metal film growth mechanisms as well as the rippled silicon substrates is given. Chapter 3 presents the experimental techniques used, including the evaporation process, self-assembly of chemical monolayers, ellipsometry, Raman scattering, infrared absorption, atomic force microscopy and scanning electron microscopy. Additionally, the methods used for the calculation of enhancement factors are presented. Chapter 4 presents the methods used for the fabrication and characterization of the substrates. The properties of the chemical monolayer are presented in Chapter 5. Chapter 6 presents the main results of the optical properties of the anisotropic nanoparticle arrays. Part 6.1 uses ellipsometry and numerical calculations to study the connection of morphology and optical properties of silver deposited rippled substrates. Part 6.2 studies the application of the unique optically anisotropic attributes of the substrate for surface enhanced Raman scattering, revealing polarization- and wavelength- dependent properties. Chapter 6.3 studies the effect of the optical anisotropy of the nanostructures regarding the surface enhancement in the infrared region, with the use of IR absorption spectroscopy, polarized FTIR microscopy as well as IR ellipsometry. Finally, chapter 7 presents the unification of surface enhancement in Raman and IR with the use of gradient thickness samples and a comparison between plain and rippled silicon substrates. Chapter 8 concludes the results and discusses a further outlook. The appendix contains supplementary graphs for chapter 7.

Part A: Theoretical background

2 Theoretical introduction

Light plays a crucial role in our understanding of the world. Since Newton analyzed light through a prism in 1666 [22], humans have been using it in order to study the nature of matter. The scientific field that studies the interaction of electromagnetic radiation with materials is called optical spectroscopy. The electromagnetic spectrum consists of frequencies as high as gamma rays to lower than those of radio waves. According to the optical spectroscopic techniques used in the present thesis, the spectral areas of interest include the ultraviolet, visible and infrared wavelengths.

The main principles of light propagation are introduced. Ellipsometry that is used for substrate characterization, as well as infrared absorption and Raman scattering spectroscopies are briefly presented. In addition, a basic introduction to the field of plasmonics is given.

Deriving from Maxwell equations, the wave equation in the paraxial limit for the case of linear optics describes the propagation of the electric field of light, as a transverse wave, across the z axis [23]:

$$E = E_o \exp[\omega t - Kz + \delta] \quad 2-1$$

where E_o stands for the maximum amplitude of the electric field, ω for the angular frequency, t for time, K is the wave vector and δ the initial phase. In case of conflicting use of symbols in literature the formalism from Fujiwara is followed [24].

2.1.1 Refractive index

The refractive index is a material property related to the phase velocity when light is travelling through a medium. It is classically described as

$$n \equiv \frac{c}{s} \quad 2-2$$

where c is the speed of light in vacuum and s the speed of light in the medium.

During light propagation in media, absorption of light may occur. The complex refractive index describes this case by introducing the absorption index k [25]

$$N \equiv n - ik \quad 2-3$$

k is connected to the absorption coefficient, α , through:

$$\alpha = \frac{4\pi k}{\lambda} \quad 2-4$$

where λ is the wavelength.

The refractive index is connected with another frequency dependent value, the complex dielectric function ϵ

$$\varepsilon = \varepsilon_1 - i\varepsilon_2 \quad 2-5$$

through the formulas

$$\begin{aligned} N^2 &= \varepsilon & 2-6 \\ \varepsilon_1 &= n^2 - k^2 \\ \varepsilon_2 &= 2nk \end{aligned}$$

The imaginary part of the dielectric function is related directly to the loss in the medium, leading to the expression for a lossless medium:

$$\varepsilon_1 = n^2 \quad \text{and} \quad \varepsilon_2 = 0 \quad 2-7$$

2.1.2 Light polarization

The electric field of the light traveling along the z direction $E(z,t)$ can be analyzed by two superimposed electric fields in the cartesian x and y directions and is described as:

$$\begin{aligned} \mathbf{E}(z,t) &= \mathbf{E}_x(z,t) + \mathbf{E}_y(z,t) & 2-8 \\ &= \{E_{x0} \exp[i(\omega t - Kz + \delta_x)]\} \mathbf{x} \\ &+ \{E_{y0} \exp[i(\omega t - Kz + \delta_y)]\} \mathbf{y} \end{aligned}$$

When the amplitude of the waves in the x and y directions is equal and the phase difference between them is 0 or π the resulting light is linearly polarized (Figure 2.1, top). In the special case where the wave amplitude is equal and the phase difference is $\pi/2$, the resulting field is circularly polarized. For every other case the resulting polarization is elliptical (Figure 2.1, bottom).

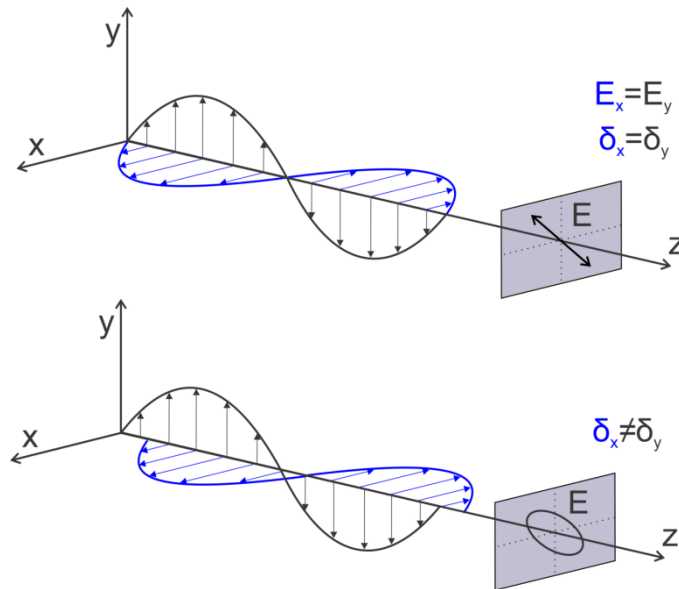


Figure 2.1: Representation of linear light polarization (top), in the case of equal wave amplitude of the E_x and E_y fields and phase difference 0 or π . In the general case (bottom), the resulting light polarization is elliptical.

When light is travelling through a medium with refractive index n_i and meets the surface of a medium with refractive index n_t at angle θ_i , a part of the light is reflected (θ_r) and another part is transmitted at a certain angle θ_t , depending on the optical properties of the mediums (Figure 2.2). The relationship between the angle of incidence and refracted angle is expressed by Snell's law:

$$n_i \sin \theta_i = n_t \sin \theta_t \quad 2-9$$

The two superimposed electric fields of the propagating light can be expressed with respect to the plane of incidence, leading to the definition of p and s polarized light. p declares the direction where the light field oscillates parallel to the plane of incidence while s denotes the perpendicular to the plane of incidence (from the German word senkrecht) (Figure 2.2).

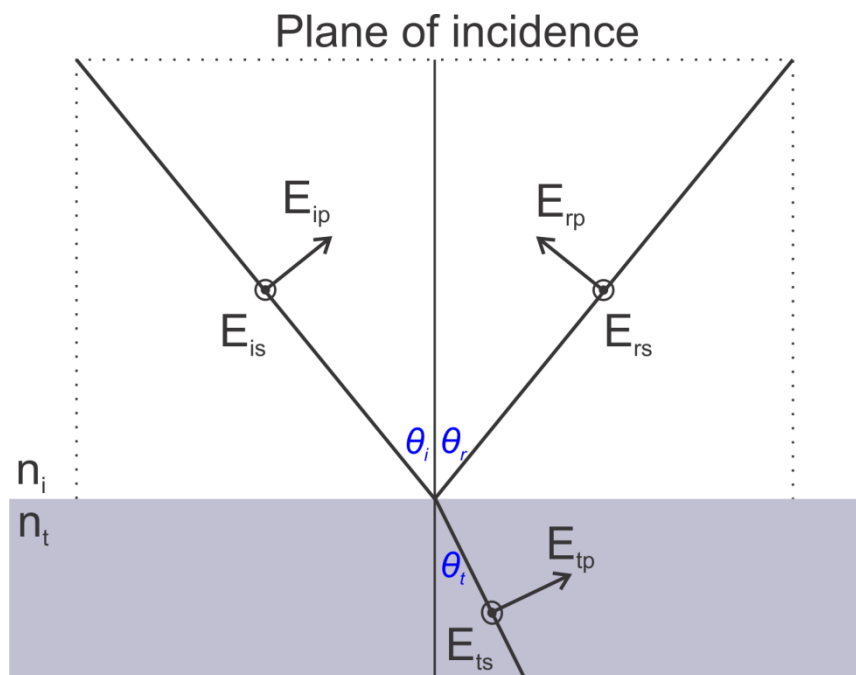


Figure 2.2: Reflection and transmission of the electric field E at the planar interface. The p-polarization component is parallel to the plane of the paper and the s-polarization perpendicular to it.

Solving Maxwell's equations with boundary conditions at an interface results in the Fresnel equations. They help determine the amplitude of reflection (r) and transmission (t) coefficients for the s- and p- polarized components. The equations for a single interface between two isotropic homogenous media take the following form:

$$r_p \equiv \frac{E_{rp}}{E_{ip}} = \frac{n_t \cos \theta_i - n_i \cos \theta_t}{n_t \cos \theta_i + n_i \cos \theta_t} \quad 2-10$$

$$r_s \equiv \frac{E_{rs}}{E_{is}} = \frac{n_i \cos \theta_i - n_t \cos \theta_t}{n_i \cos \theta_i + n_t \cos \theta_t}$$

$$t_p \equiv \frac{E_{tp}}{E_{ip}} = \frac{2n_i \cos \theta_i}{n_t \cos \theta_i + n_i \cos \theta_t}$$

$$t_s \equiv \frac{E_{ts}}{E_{is}} = \frac{2n_i \cos \theta_i}{n_i \cos \theta_i + n_t \cos \theta_t}$$

The refractive index can be real or complex without changing the relations in the equations.

2.2 Ellipsometry

Ellipsometry is a spectroscopic technique that collects valuable optical information from the reflection (or transmission) of light from a surface. The name derives from the elliptically polarized light that is reflected and holds the information of the interaction with the sample [25].

Specifically, incoming light passes through optical elements, such as a polarizer and a compensator resulting in a known polarization state. It meets the sample at an oblique angle, and the material interacts with the light, changing its polarization state. The reflected light passes through a second polarizer (analyzer) and is collected by a detector. The change of the amplitude of the two polarizations, p- and s-, as well as their phase difference after the reflection is expressed by the basic ellipsometric values Ψ and Δ , respectively. They are connected with the ratio of the complex reflection coefficients for p- and s- polarization by

$$\rho \equiv \tan \Psi \exp(i\Delta) \equiv \frac{r_p}{r_s} \equiv \frac{E_{rp}/E_{ip}}{E_{rs}/E_{is}} \quad 2-11$$

With the measurement of only those two values and by applying the Fresnel equations, the complex refractive index and the dielectric function can be determined (2-3, 2-5), assuming a sample that has no over-layers or roughness. The pseudodielectric function is determined as follows:

$$\langle \varepsilon \rangle = \langle \varepsilon_1 \rangle - i \langle \varepsilon_2 \rangle = \langle N \rangle^2 = (\langle n \rangle - i \langle k \rangle)^2 \quad 2-12$$

$$= \sin(\theta_i)^2 \left[1 + \tan(\theta_i)^2 \left(\frac{1 - \tan(\Psi) e^{i\Delta}}{1 + \tan(\Psi) e^{i\Delta}} \right)^2 \right]$$

The pseudodielectric function describes the optical activity of the sample as a whole, but for complicated samples with stack of layers or inhomogeneity, in order to extract the optical information of the separate layers, rigorous models have to be applied to fit to the measured data.

Ellipsometry is a popular technique for optical measurements of the thickness of thin films due to its extreme sensitivity, which can detect nanometer thicknesses. Besides the definition of the optical constants n and k , the technique can provide values of surface

roughness, anisotropy, crystallinity, chemical composition. It has the advantages of being fast and reliable, as it is self-referencing, while it is non-destructive due to the use of polarized light. For those advantages, it is used under ex-situ as well under in-situ conditions and has found broad applications from the semiconductor industry to biology [26-28].

The disadvantage and limitation of this technique is the necessity of a model for determining the quantities by the application of fitting procedures. The complexity of the sample may hinder the construction of an appropriate model.

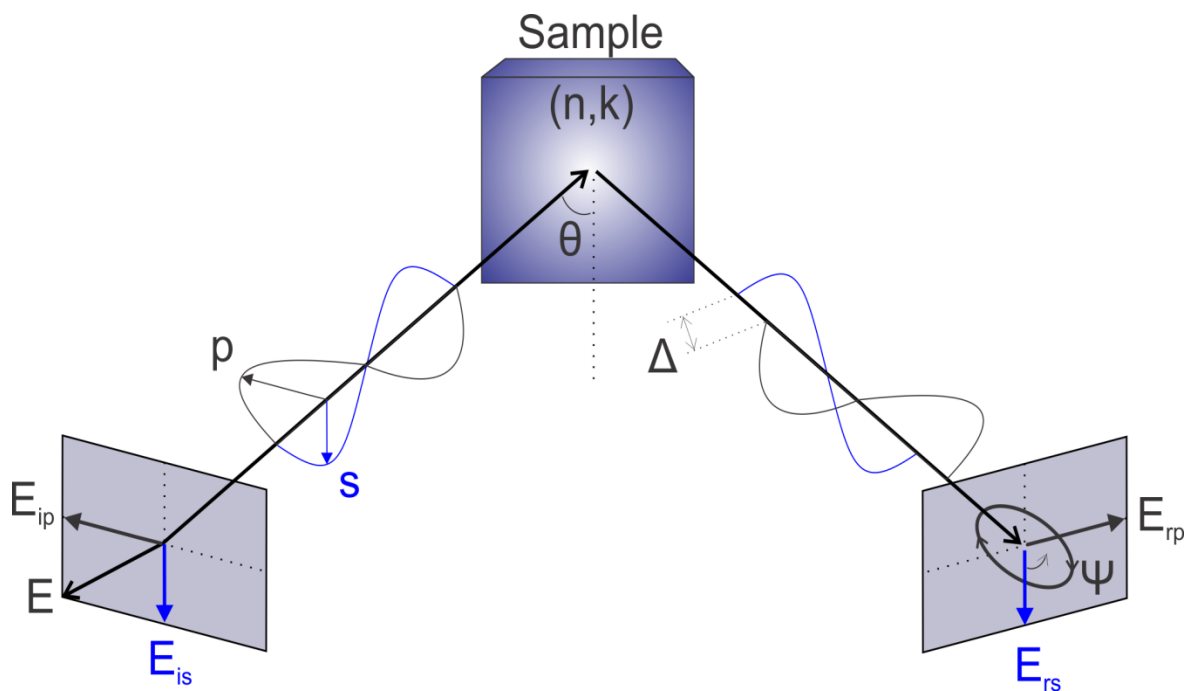


Figure 2.3: Principle of ellipsometry. Linearly polarized light is reflected off the sample's surface resulting in elliptically polarized light. The amplitude ratio and phase difference of p- and s- components are the measured ellipsometric quantities Ψ and Δ .

Reflection from a homogenous surface can be described by four complex reflection coefficients comprising the *Jones matrix* [29].

$$\mathbf{J} = \begin{bmatrix} r_{pp} & r_{ps} \\ r_{sp} & r_{ss} \end{bmatrix} \quad 2-13$$

The Jones matrix is useful for describing polarization and ellipsometric measurements mathematically. For example, the optical element of a linear polarizer is expressed as:

$$\mathbf{J} = \begin{bmatrix} 1 & 0 \\ 0 & 0 \end{bmatrix} \quad 2-14$$

In isotropic materials the off-diagonal values of r_{ps} and r_{sp} are zero, enabling the direct definition of ρ . For anisotropic materials, a part of p- polarized light is converted to s-polarized light and the other way around and subsequently the off-diagonal Jones matrix elements are non-zero. In this case, Generalized Ellipsometry (GE) is used to define all the matrix elements [30].

Whereas the Jones matrix is useful for describing fully polarized light, there are several sources that could create depolarization, such as rough surfaces; interfaces between inhomogeneous thickness films; non ideal polarizers; backside reflection from a weakly absorbing substrate; divergent light beam; insufficient spectral resolution [31]. A more general description that includes the unpolarized and partially polarized cases can be given by the Mueller matrix formalism, which provides the most general and complete information of how the light interacts with a sample [32]. In the examined samples no significant depolarization was measured therefore the use of Mueller Matrix Ellipsometry was not necessary.

2.2.1 Oscillator models

As mentioned above, modelling is critical for extracting information from ellipsometric measurements. In the following part are presented some basic models that describe mathematically the interaction of the electric field of light with the electrons of the material. Another approach to ellipsometric modelling is the Effective Medium Approximation models (EMAs) [33].

Lorentz model

In the presence of an electric field the electron bound to a nucleus experiences a linear restoring force. The *Lorentz model* derives from Newton's second law for a spring that connects a bound nucleus and a moving electron:

$$\varepsilon(\omega) = 1 + \frac{e^2 N_e}{\varepsilon_0 m_e} \cdot \frac{1}{\omega_0^2 - \omega^2 - i\Gamma\omega} \quad 2-15$$

where N_e stands for the number of electrons per unit volume, m_e the electron mass and e its charge. ω_0 represents the resonance frequency of the oscillator and Γ is the damping coefficient, describing the degree of the oscillation damping due to material properties such as defects [29, 34].

Drude model

In metals, the electrons of the conduction band are moving freely, unbound to any nucleus and subsequently the restoring force is zero. The electrons move following the phase of the imposed electric field described by the *Drude model* [35]:

$$\varepsilon(\omega) = 1 - \frac{\omega_p^2}{\omega^2 + i\Gamma\omega} \quad 2-16$$

The Drude plasma frequency is defined by:

$$\omega_p = \sqrt{\frac{e^2 N_e}{\epsilon_0 m_e}} \quad 2-17$$

This is the plasma oscillation resonance that will be further discussed in chapter 2.3.

The electron mass, m_e , can be substituted by the effective mass in order to account for the coupling to the ion core.

Tauc-Lorentz

Among the numerous optical models, the *Tauc-Lorentz* model is used for describing the interband transitions because it includes the density of states, which contribute to the curve shape [29, 36]. Initially it was developed for amorphous and crystalline materials but modifications of this formula can also be used to describe the interband transitions in gold and silver [37, 38].

At an interband transition with optical band gap $\hbar\omega_g$, the imaginary part of the dielectric function is zero for frequencies equal or below the gap, while for frequencies above is expressed as:

$$\epsilon_2(\omega) = \frac{1}{\omega} \cdot \frac{A\omega_0\Gamma(\omega - \omega_g)^2}{(\omega^2 - \omega_0^2)^2 + \Gamma^2\omega^2} \quad 2-18$$

with A , ω_0 and Γ as the amplitude, center frequency and broadening respectively. The real part of the dielectric function can be obtained by Kramers-Kronig equations, mathematic relations that connect the real with the imaginary part of a complex function [39].

2.3 Plasmonics

A plasmon is frequently described as the quantum of plasma oscillation [40]. The interaction of namely the electric field of light with a metal displaces charges in the material. The created electron cloud oscillates under the restoring force of the positive ion cores at the plasma frequency, ω_p .

For different conditions plasmons can be generated in the bulk of the metal (Volume plasmon), in the interface between a metal and dielectric (Surface Plasmon Polariton) and in metal structures with sizes in the sub-wavelength limit (Localized Surface Plasmonic Resonances) [29, 41-48].

The plasma model is described by the Drude equation 2-16. The damping constant Γ , is defined as inversely proportional to the relaxation time of free electron gas, τ [41]

$$\Gamma = \frac{1}{\tau} \quad 2-19$$

Combining the equations 2-5, 2-16 and 2-19, the complex dielectric function is analyzed to the real and imaginary components

$$\varepsilon_1(\omega) = 1 - \frac{\omega_p^2 \tau^2}{1 + \omega^2 \tau^2} \quad 2-20$$

$$\varepsilon_2(\omega) = \frac{\omega_p^2 \tau}{\omega(1 + \omega^2 \tau^2)}$$

There are two frequency regions in metals, one for $\omega < \omega_p$, where the metal retains its metallic character with a negative real part of the dielectric function ($\varepsilon_1 < 0$). In the regime where frequencies are quite lower than the ω_p , $\varepsilon_2 \gg \varepsilon_1$ and the metal is strongly absorbing. At incoming light frequencies above the plasma frequency, $\omega > \omega_p$, the metal acts like a dielectric ($\varepsilon_1 > 0$, with $\varepsilon_1 \rightarrow 1$ for $\omega \gg \omega_p$) because the electrons cannot follow the rapid oscillation of the incoming field [41].

The dielectric constant ε_∞ is introduced in the Drude equation to sum up the higher energy contributions to the dielectric function:

$$\varepsilon(\omega) = \varepsilon_\infty - \frac{\omega_p^2}{\omega^2 + i\Gamma\omega} \quad 2-21$$

The geometrical conditions of the metal structure result in the creation of different kind of plasmons. In the case of a field oscillating at the plasma frequency in a homogenous metal media a *volume plasmon* is created. It is described as a longitudinal oscillation of the electron gas that moves in phase against the restoring force of the fixed ion background.

In the case of an interface between a dielectric and a metal under certain conditions a *surface plasmon polariton* is created. According to boundary conditions, when the real part of the dielectric permittivities of the two media have opposing signs, i.e. conductor and insulator, the electrons of the metal oscillate in conjunction with the wave creating a surface wave.

From the case of semi-infinite planar material, the focus shifts to the special case of sub-wavelength metal particles. The plasmons resulting from this geometry are called *localized surface plasmons*. In contrast to volume and surface plasmons, the localized plasmons involve electrons confined in nanosized material.

The small size of the metal introduces the quasistatic approximation $a_0 \ll \lambda$ (a_0 is the particle radius), meaning that the particle is much smaller than the wavelength of light and a simplified case of the particle being in an electrostatic field can be applied. Gustav Mie's solutions of the Maxwell equations for an arbitrary sized sphere predict the absorption and scattering properties [49]. For the quasistatic limit, where no retardation effects are considered and the field is constant, the polarizability (α) of the sphere is

$$\alpha = 4\pi a_0^3 \frac{\varepsilon - \varepsilon_m}{\varepsilon + 2\varepsilon_m} \quad 2-22$$

a_0 is the particle radius, ε_m is the dielectric constant of the embedding medium and ε the metal's complex dielectric function. The polarizability will be resonantly enhanced when the denominator is minimum. Provided that $\text{Im}(\varepsilon)$ is small or non-dependent on ω , the formula leads to the Fröhlich condition for the existence of the dipole surface plasmon:

$$\text{Re}[\varepsilon(\omega)] = -2\varepsilon_m \quad 2-23$$

There is strong connection of the plasmon resonance and the surrounding dielectric medium. For a Drude pure metal the localized surface resonance is at $\omega_o = \omega_p/\sqrt{3}$ but for real metals like gold and silver the frequency is considerably reduced.

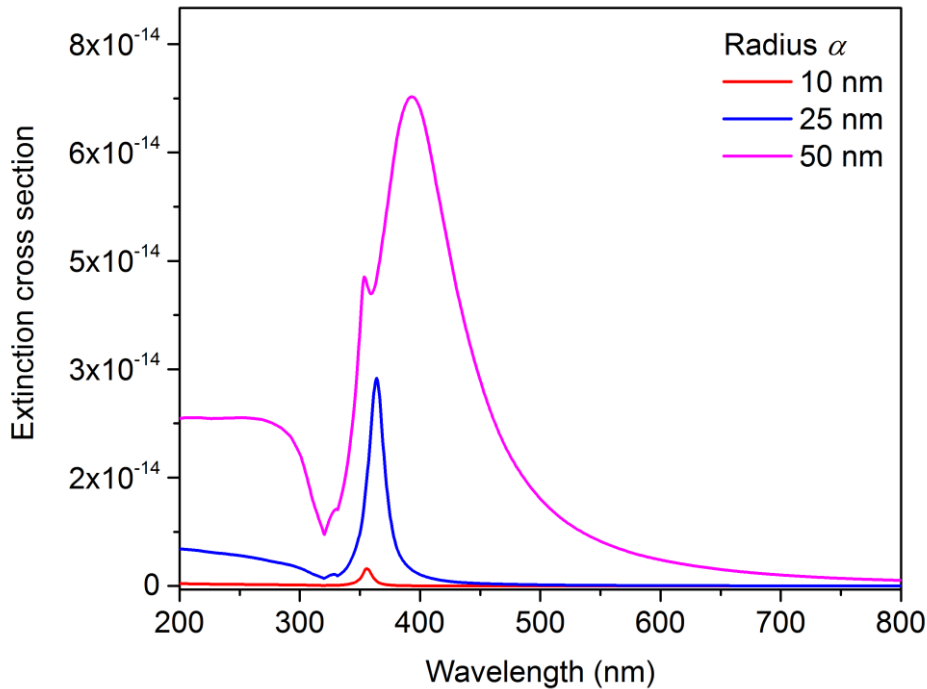


Figure 2.4: Extinction cross section of Mie scattering for a single Ag sphere in vacuum (Calculated by MiePlot v4.5 @Philip Laven)

The plasma frequency relates to the size and shape of the nanoparticle. The increasing size of nanoparticles causes a red-shift of the dipolar mode due to retardation and the appearance of the quadrupolar mode [50]. Additionally, broadening of the oscillation is observed that is due to intraparticle absorption effects (Figure 2.4). Furthermore, by breaking the spherical symmetry shape effects are introduced. An example is that of an ellipsoid, with its major and minor axis. The electron oscillation along these two axes results in two separated resonances, with the major axis resonance being red-shifted according to the particle aspect ratio [51].

Nanoparticles can be isolated or they can be found in ensembles that result in coupled plasmon resonances. In the case of more than one nanoparticle, the localized modes electromagnetically interact with each other resulting in a variety of intricate optical behaviors that depend on the ensemble geometry. In simple ensemble geometry, near-field coupling results in blue-shifting resonance when the polarization direction light excites the transverse modes. Correspondingly, the resonance red-shifts when the light excites the longitudinal modes (Figure 2.5). Owing to this coupling the confined inter-particle spaces can achieve the highest field enhancement, at positions termed as “hot-spots”.

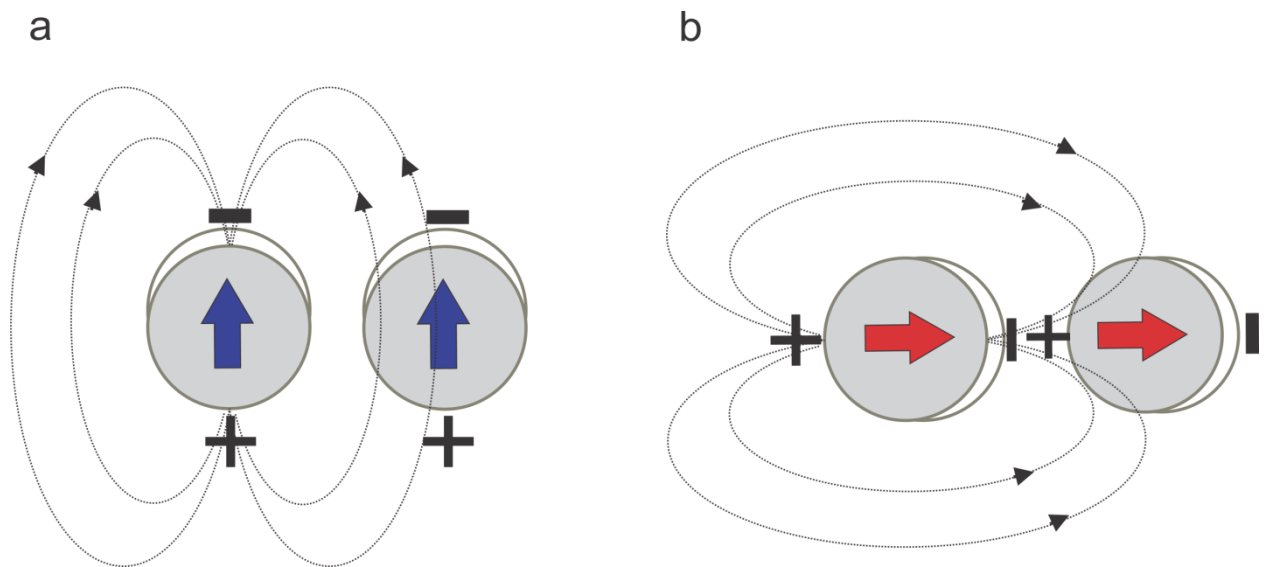


Figure 2.5: Near-field coupling between metallic nanoparticles, resulting in blue (a) or red (b) shifting of the dipole resonance frequency.

The significance of the dipole particle plasmon resonance is that the resonantly enhanced polarization leads to field-enhancement that drastically augments the absorption and scattering of the light in the area of the particle. This effect finds applications in a variety of significant fields: e.g. the exploitation of SPP to create waveguides, sensing on the surface of prisms with attenuated total reflection, manufacturing of sophisticated LSPR structures with metamaterial properties and the use of LSPRs in high sensitivity and selectivity sensing, with field enhancements enabling single molecule detection [8]. For further understanding of the vast field of plasmonics and its applications the reader is referenced to in-depth literature such as [41] and [46].

2.4 Vibrational spectroscopy

In the field of linear optics, when a photon interacts with a molecule it can either scatter elastically, retaining its wavenumber (Rayleigh scattering) [52], scatter inelastically resulting in photons with altered wavenumbers (Raman scattering) or it can be absorbed [53]. The probability of these events depends on the wavenumber of the photon and on the cross section of each interaction. Light at the visible or infrared region induces transitions to the vibrational and rotational modes of the molecule, resulting in Raman scattering or IR

absorption, respectively and providing crucial information about the nature of compounds. The possible transitions are schematically presented by the Jablonski diagram in Figure 2.6.

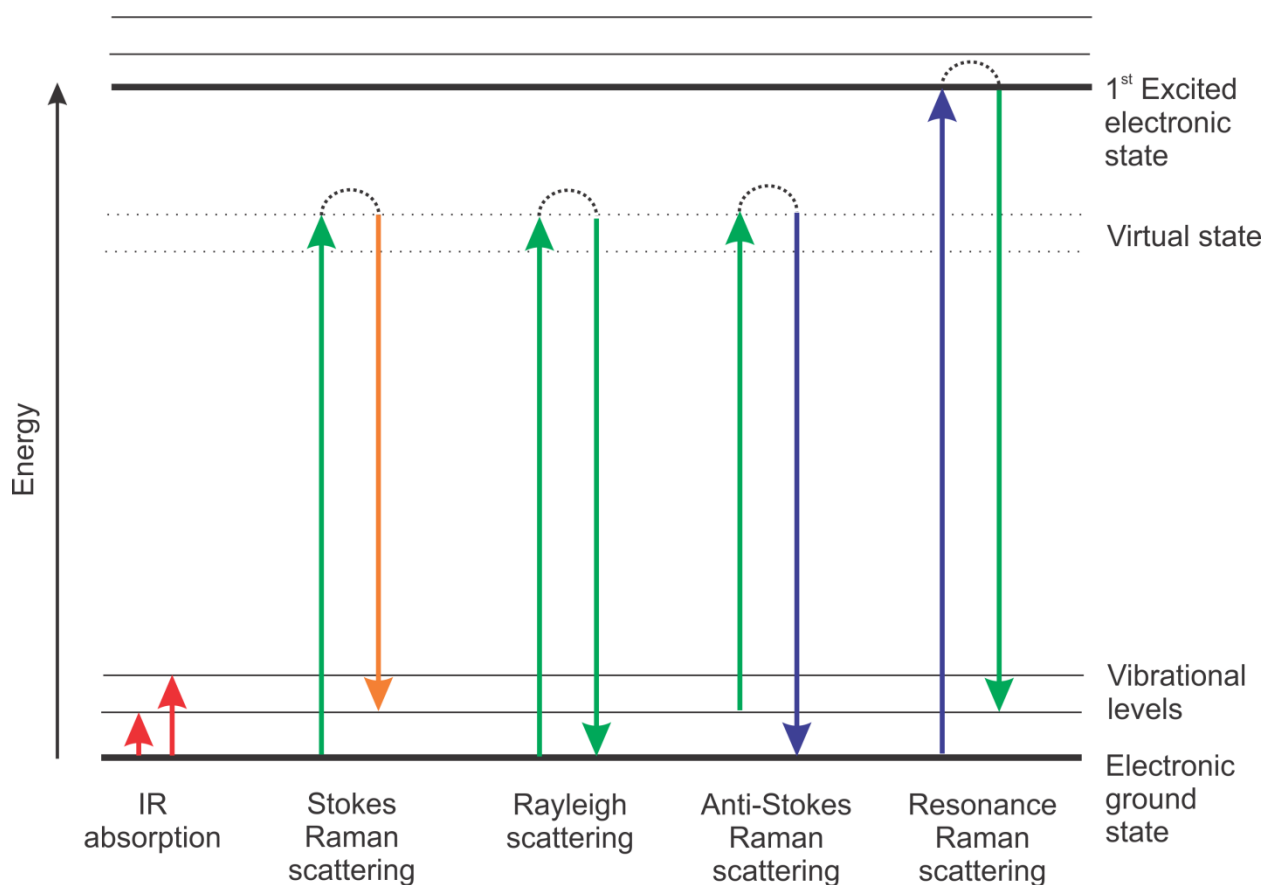


Figure 2.6: Jablonski diagram of transitions in vibrational spectroscopy

[54].

These vibrational-rotational transitions belong to the IR and far-IR region and are equivalent for the two techniques. Due to different mechanisms though, IR and Raman follow different selection rules which define different probabilities of the active modes for each technique. The selection rules can be determined from symmetry and group theory. The combination of both techniques would provide the complete vibrational information of optically active modes of a molecule [55].

Both of the techniques are considered to be powerful analytical tools for applications in industry and research, in numerous fields such as pharmaceuticals, life sciences and material physics. IR absorption is an established technique for a longer time compared to Raman scattering since the involved intensities are comparatively too low. But in the more recent years technical developments of laser light sources gave Raman a significant boost. Furthermore, the discovery of surface enhanced techniques made surface enhanced Raman scattering (SERS) more applicable as it leads to signal enhancements orders of magnitude stronger than the counterpart surface enhanced infrared absorption (SEIRA).

In the following part the fundamentals of the techniques and the phenomena involved in the surface enhancement are briefly introduced.

2.4.1 Raman scattering

The phenomenon is named after the Indian physicist C.V. Raman, who was the first to discover the frequency shift of scattered light, granting him a Nobel prize in 1930 [56]. The mechanism of Raman scattering can be described with a classical or quantum mechanical approach.

This chapter follows the formalism of Vibrational Spectroscopy in Life Science by F. Siebert and P. Hildebrandt [57].

A molecule can be depicted with the classical image of the ball and string model. The atoms are connected to each other and displace in a way that can be described with the harmonic oscillator equation. The degrees of freedom for non-linear molecules of N atoms are 3N-6 (3N-5 for linear). The characteristic vibrations of the molecule are denoted as normal modes (k) in which some or all atoms vibrate together with the same frequency, $\widetilde{\nu}_k$, but different amplitudes:

$$\widetilde{\nu}_k = \frac{\nu_k}{c} \quad (cm^{-1}) \quad 2-24$$

Upon interaction of the light with the molecule, the electric field induces an oscillating dipole which subsequently produces radiation at frequencies modulated by the normal modes. From a quantum perspective, a photon with frequency $\widetilde{\nu}_0$ is scattered by the molecule, producing a phonon at the normal mode frequency $\widetilde{\nu}_k$ and a photon with frequency $\widetilde{\nu}_0 - \widetilde{\nu}_k$ (Stokes Raman scattering). In the case where a phonon is annihilated the resulting frequency of the scattered photon is $\widetilde{\nu}_0 + \widetilde{\nu}_k$ (anti-Stokes scattering) [10].

The induced dipole moment, μ , is proportional to the polarizability of the molecule α and the applied electric field

$$\mu = \alpha \cdot E \quad 2-25$$

The polarizability tensor α can be described by a 3x3 matrix

$$\begin{bmatrix} a_{xx} & a_{xy} & a_{xz} \\ a_{yx} & a_{yy} & a_{yz} \\ a_{zx} & a_{zy} & a_{zz} \end{bmatrix} \quad 2-26$$

where x, y, z are the directions of the Cartesian axis. The matrix is symmetric for the case of non-resonant Raman.

The selection rule for Raman scattering requires that for a certain transition the polarizability tensor has to change with the normal coordinates, Q_k ,

$$\left(\frac{\partial \alpha_{\rho, \sigma}}{\partial Q_k} \right)_0 \neq 0 \quad 2-27$$

where ρ and σ denote molecule fixed coordinates.

In the quantum mechanical treatment the induced dipole amplitude is the transition moment amplitude for a $i \rightarrow f$ transition

$$[\mu_0]_{fi} = \langle \psi_f | \boldsymbol{\alpha} | \psi_i \rangle \cdot \mathbf{E}_0 \quad 2-28$$

where ψ_f and ψ_i are vibrational wavefunctions .

The polarizability tensor for a transition between the $|i\rangle$ and $\langle f|$ vibrational states in the ground electronic state, G, is described by the Kramers-Heisenberg-Dirac dispersion theory [10, 58]:

$$[\alpha_{\rho\sigma}]_{if} = \frac{1}{\hbar} \sum_{R,r} \left(\frac{\langle iG | M_\rho | Rr \rangle \langle rR | M_\sigma | Gf \rangle}{\nu_{Rr} - \nu_k - \nu_0 + i\Gamma_{Rr}} + \frac{\langle rR | M_\sigma | Gf \rangle \langle iG | M_\rho | Rr \rangle}{\nu_{Rr} - \nu_k + \nu_0 + i\Gamma_{Rr}} \right) \quad 2-29$$

M_σ and M_ρ refer to the electronic transition dipole moment expressed in the fixed coordinate system. R and r refer to the electronic and vibronic states, respectively with Γ_{Rr} being the damping constant of the Rr vibronic state and ν_{Rr} its frequency. ν_0 is the excitation photon frequency and ν_k is the normal mode frequency. In non-resonant conditions ν_0 is effectively smaller than the electronic transition frequency, leading to increased denominators and therefore low values of polarizability [58, 59].

As it is mentioned above, the Raman scattering cross section is quite low compared to elastic scattering. The polarizability tensor is correlated with the vibrational $i \rightarrow f$ transition cross section by [60]

$$\sigma_{i \rightarrow f} \propto (\nu_0 \pm \nu_k)^4 \cdot \sum_{\rho, \sigma} |\alpha_{\rho, \sigma}|^2 \quad 2-30$$

The cross section of Raman scattering is therefore inversely proportional to the fourth power of excitation wavelength. This rule plays a role in the choice of excitation laser line. Additionally, resonance Raman scattering may define in some molecules the choice of laser line in order to increase the cross section of the effect. The significant increase in the Raman signal takes place when the incident light's frequency is close to that of an electronic transition. The underlying mechanism is connected to an enlargement of the induced dipole moment generated by the electronic-vibronic transition coupling. Resonance Raman is a significant part of Raman spectroscopy but falls outside of the scope of the present thesis. The topic is extensively studied in the cited literature [10, 58-61].

2.4.1.1 *Surface Enhanced Raman Scattering (SERS)*

The typical Raman cross-section is between 10^{-30} - 10^{-25} cm²/molecule, a low value compared to other techniques, e.g. fluorescence at 10^{-17} - 10^{-16} cm²/molecule. With the introduction of surface enhanced Raman scattering (SERS), the low sensitivity due to cross-section is counterbalanced by the surface enhancement, favoring the use of the technique in prominent fields such as bioanalytics [62].

In the 1970s, scientists noticed that the molecular Raman signal was increased in the proximity of metal structures [63, 64]. The proposed mechanism involves a strongly enhancing electromagnetic effect, deriving from the surface plasmon resonance and, in

special cases, a weaker enhancing chemical effect, deriving from metal-molecule charge-transfer resonance that induces changes to the polarizability tensor. A significant enhancement can be added up with the choice of a molecule with molecular resonance at the excitation wavelength. In that case the technique is called surface enhanced resonance Raman scattering (SERRS) [65].

The exact calculation of the enhancement factor (EF) is a controversial matter, partly on account of the contribution of the mentioned factors above and partly for the difficulty of estimating parameters such as the number of excited molecules. Regardless of the estimations of EFs as big as 10^{14} or arguments pointing to 10^7 - 10^8 , single molecule detection has been achieved since 1997 [8, 66, 67]. Since then, progress has been made into observing single molecules in structures other than colloidal solutions [68] and debates on actual single molecule detection have led to invention of verification techniques [69]. Generally the EF could be divided into (i) the maximum/local SERS EF that is assigned for hot-spots and (ii) an average EF for molecules generally on the metallic surface.

The electromagnetic enhancement originates from the spatial localization of the electric field of light. The existence of metal at a certain spot changes the intensity of the incident field, $|E_{inc}|$. The generated local field intensity is proportional to the square of the electric field amplitude at that point, $|E_L|^2$. Depending on the metal, the incoming electric field wavelength and the geometry, the local field can be weaker or stronger by several orders of magnitude. The local field intensity enhancement factor can therefore be described as

$$LFIEF(\omega_L) = \frac{|E_L|^2}{|E_{inc}|^2} \quad 2-31$$

The strongest enhancements are achieved for interspaces between metal nanoparticles with the incident electric field vector matching the orientation of the nanocavity and the according wavelength in order to couple the dipole resonances of the nanoparticles. These positions of maximum localized field are called 'hot-spots' (Figure 2.7). By placing a molecule in that spot the result will be the emission of scattered photons at ω_R . The Raman scattered field will be further enhanced by the metallic surface in the same way as the incident field.

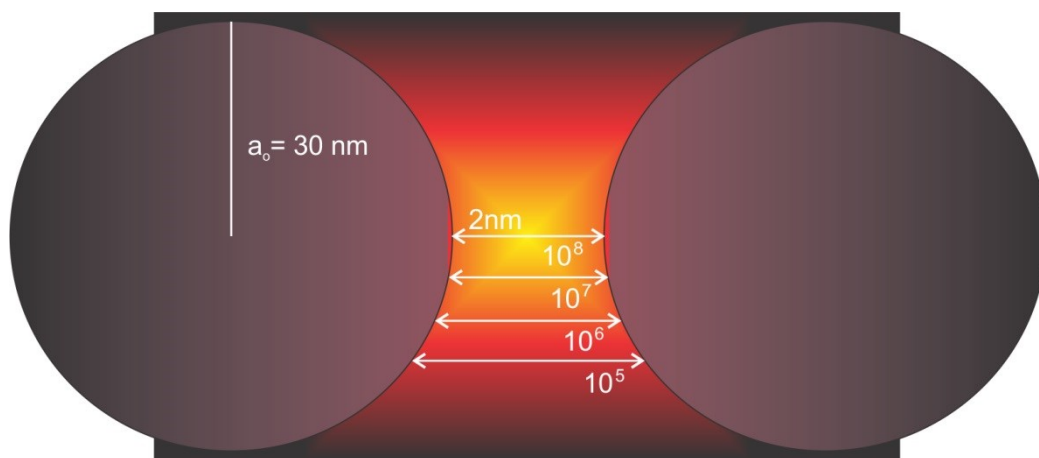


Figure 2.7: A 'hot-spot' created in the cavity between a dimer and the rapid change of enhancement factor with the distance. Adapted from [70].

Through series of approximations regarding polarization dependence, angular dependence, molecular symmetry, and the symmetry of the metallic nanostructure as well as the difference between the local field frequency ω_L and the scattered Raman frequency ω_R , the SERS enhancement factor can be estimated by the so-called $|E|^4$ approximation [44, 71]

$$EF \sim LFIEF^2(\omega_L) = \frac{|E_L|^4}{|E_{inc}|^4} \quad 2-32$$

The distance from the metal surface is essential to the enhancement of the molecule, may it be adsorbed or simply in the vicinity of the metal. For spherical colloids of radius a_0 the decrease of EF with the distance d from the surface is

$$EF_{SERS}(d) = EF(0) \cdot \left(\frac{a_0}{a_0 + d}\right)^{12} \quad 2-33$$

where $EF(0)$ is the enhancement factor of molecules directly adsorbed on the surface. Along with the size, the shape of the nanostructures is another factor that influences the enhancement, as discussed in chapter 2.3. Those two factors are used to tailor LSPR absorption in the desired ranges. Effects of size were shown in Figure 2.4, while shape effects are presented at Figure 2.8. It is shown that for deviation from spherical shape multipolar modes are introduced, related to the different light polarization possibilities in the nanoparticle. These modes are red-shifted in comparison to a spherical structure, while the change of the aspect ratio, as seen for the rods in Figure 2.8, can result in simultaneous absorptions in the visible and infrared region.

The experimental approach for estimating the EF is the analytical enhancement factor [66]

$$AEF = \frac{I_{SERS}}{I_R} \frac{N_R}{N_{SERS}} \quad 2-34$$

where I_R and I_{SERS} are the Raman intensities of probe molecules in solution and adsorbed on the metal surface respectively. N_R and N_{SERS} refer to the number of excited molecules.

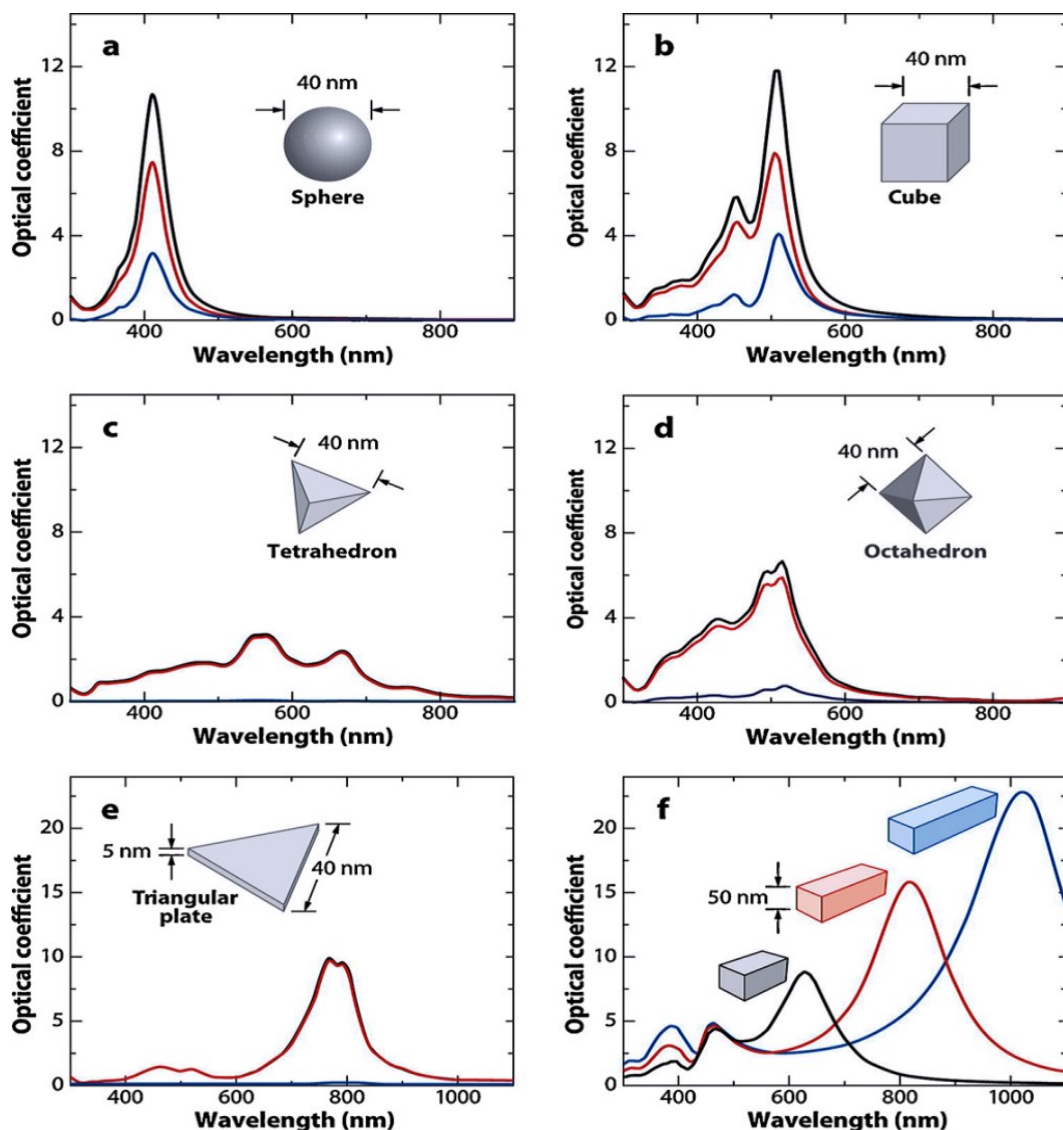


Figure 2.8: Extinction (black), absorption (red), and scattering (blue) spectra calculated for Ag nanoparticles of different shapes. (f) shows extinction spectra of rectangular bars with aspect ratios of 2 (black), 3 (red), and 4 (blue). Note that the nonspherical particles typically exhibit multiple, red-shifted resonance peaks. Reprinted with permission from [45].

The chosen metals for SERS applications in the Visible and NIR are traditionally the Group-11 metals Au, Ag and Cu. Pt and Pb can provide reasonable enhancements for the ultraviolet region. The need, though, for broader applicability drives research on creating non-Group 11 SERS active substrates [72]. Apart from the metal of choice, there is a variety in substrate structures as well. The main trends in the fabrication of SERS-active substrates are these of [73]:

- metallic nanoparticles in solution (e.g. colloidal solutions)
- planar metallic structures (e.g. nano-particle arrays on silicon substrate)
- metallic electrodes

At this point it has to be mentioned that a typical Raman tensor study through polarized experiments cannot be performed in the same way for SERS as in typical Raman spectroscopy. For the case of molecules attached on a rough metal surface, the macroscopic SERS signal averages over excitation on many directions leading to depolarized results. In the case of a molecule placed in a hot-spot, the coupling of the incoming electric field to the dipole and the polarization modulation when rotating on the dipole axis, plays a more significant role in the Raman intensities than that of the molecule Raman tensor [74].

2.4.2 Infrared absorption

In the year 1800 Sir William Herschel discovered the infrared radiation in the spectrum of the sunlight. That led to the foundation of infrared spectroscopy. During 1905 an extended catalogue of IR spectra was published by Coblentz, supporting that certain groups of molecules have absorption at certain wavelengths, establishing IR as a fingerprint technique [75]. Later, the introduction of Fourier Transform technique combined with a Michelson interferometer increased measurement sensitivity, establishing IR as a broad commercial application [76].

When light in the infrared region interacts with matter, it is absorbed when its energy ($h\nu$) matches that of a fundamental excitation (electronic states, vibrational states, plasmons). Specifically in molecules, the resonant absorption of a photon with energy that matches that of an excited vibrational state takes place (Figure 2.6). The process can be described simply by:

$$h\nu = h\nu_f - h\nu_i \quad 2-35$$

Where h is the Planck constant, ν_i and ν_f the frequencies of the initial and final states, respectively.

The probability of the transition between the initial and final state is given by the transition dipole moment

$$[\mu_q]_{fi} = \langle \psi_f | \mu_q | \psi_i \rangle \quad 2-36$$

The expansion of the operator μ_q in Taylor series with respect to the normal coordinates Q_k leads to the two conditions for an IR active transition within the harmonic approximation. The first is that there has to be a unit change in the quantum number, $i \neq f$, meaning that the transition should happen between two discrete vibrational states. Second, IR absorption is possible when there is a change in the dipole moment with the normal coordinate

$$\left(\frac{\partial \mu_q}{\partial Q_k} \right)_0 \neq 0 \quad 2-37$$

$(q = x, y, z)$

Therefore, if those conditions are met, polarized light propagating in the x direction would induce absorption from the vibrations that have transition dipole moment along the x axis.

For unpolarized light, absorbance A is proportional to the transition probabilities of all the axes [77].

$$A \propto (|\mu_{fi}|_x^2 + |\mu_{fi}|_y^2 + |\mu_{fi}|_z^2) \quad 2-38$$

As it is already discussed, the Raman effect requires change in polarizability with the normal coordinate. These two discrete conditions can be derived from group theory, which can prove a demanding task for polyatomic molecules. The simplest case is a homonuclear diatomic molecule that has a center of symmetry along the bond. The rule of mutual exclusion states that a centrosymmetric molecule cannot be both Raman and IR active. The homonuclear molecule during stretching of the bond length does not induce dipole moment (IR inactive), whereas the volume of the electron cloud increases inducing modulation in the polarizability (Raman active) [10, 61, 78].

2.4.2.1 *Surface enhanced infrared absorption (SEIRA)*

In 1980 Hartstein et al. discovered the enhancement of molecular layers on metal structures in attenuated-total-reflection setup as a result of collective electron resonances due to the island nature of thin metal films [79]. This realization signaled the beginning of SEIRA. Its mechanism remains more obscure than the SERS counterpart and is not so widely used due to lower enhancement factors (10-1000), even though the cross-section σ for infrared absorption 10^{-20} cm^2 counterweights the lower EF. Nevertheless, it has played a significant role in electrochemistry [20, 59, 80] and during the recent years is gaining momentum in various analytical applications [81, 82], including biosensing [83].

The types of supports that have been extensively used for SEIRA purposes are evaporated nano-islands, electrochemical deposited substrates and metal colloids [84]. SEIRA enhancements can be achieved for coinage metals as well as transition metals [85], while it has been demonstrated that the use of the phonon resonance can lead to equivalent plasmon resonance enhancements [86].

The metal islands of the SEIRA substrate are mainly represented as metal ellipsoids on a surface covered by an adsorbed molecular layer (Figure 2.9). The incident EM field induces dipole oscillation (p) at the plasmonic resonance region that generates a local field stronger than the incident field. As only the field of the incident radiation is enhanced, the enhancement factor with respect to the distance from the metallic surface is not as strongly correlated as in the case of SERS.

$$EF_{SEIRA}(d) = EF(0) \cdot \left(\frac{a_0}{a_0 + d}\right)^6 \quad 2-39$$

Furthermore, the adsorbed molecules induce additional dipoles (δp) changing the optical properties of the metal. In that condition, the molecule's strong perturbation at the vibrational frequencies in combination with the metal's strong absorption leads to amplification of the absorption. These conditions summarize the *electromagnetic origin* of the enhancement [87, 88]. The *chemical origin* of the enhancement lies in chemical

interactions that increase the $\left|\frac{\partial \mu_q}{\partial Q_k}\right|^2$ and therefore the absorption. The absorption is proportional to

$$A \propto \left|\frac{\partial \mu_q}{\partial Q_k}\right|^2 \cdot |\mathbf{E}|^2 \cos^2 \theta \quad 2-40$$

where θ is the angle between dipole moment derivative and the electric field. As a result of the chemical interactions, chemisorbed layers manifest larger enhancements than the physisorbed ones.

As can be derived from the $\cos^2 \theta$ in 2-40, SEIRA is strongly influenced by the orientation of adsorbed species. The *surface selection rule* denotes that the vibrational modes enhanced are the ones with dipole moment derivative components perpendicular to the surface [89, 90].

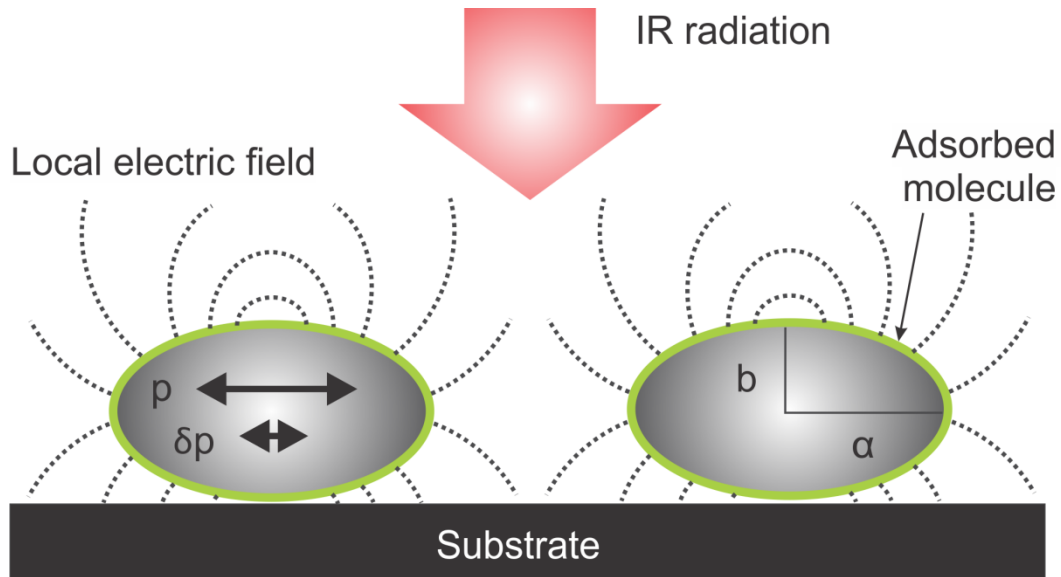


Figure 2.9: Electromagnetic mechanism of SEIRA. The electric field of incident IR light induces a dipole p in the metal island generating an enhanced local electric field around the particles. Also, the molecular vibrations induce an additional dipole δp and perturb the optical properties of the metal.

The SEIRA enhancement can be calculated by *Effective Medium Approximation (EMA) models* where the effective optical properties are estimated for a volume that is a mixture of metal and matrix material. The layer inhomogeneities are smaller than the wavelength and the material is treated as having homogenous effective permittivity therefore the Fresnel equations are applicable. The main models are based on the Bruggeman and the Maxwell-Garnet theory (MGT). Further investigation of the EMAs is outside the scope of the present thesis. Extensive information can be found in the cited literature [33, 87, 91].

2.5 Thin metal film growth

As discussed above, SERS and SEIRA active materials may be obtained by evaporated island films. For deposition of thin films, one must consider the source of the evaporated atoms as well as the substrates upon which they deposit. The growth of metal on a support surface falls under the rules of heterogenous nucleation. The nucleation process is driven by the minimization of Gibbs energy (ΔG) and promoted by the atom diffusion. A description is given by Young's equation:

$$\cos(\theta_{wet}) = \frac{\gamma_{sv} - \gamma_{fs}}{\gamma_{fv}} \quad 2-41$$

γ are the interfacial surface energies of the film f , substrate s , vapor v and θ_{wet} the wetting angle (Figure 2.10).

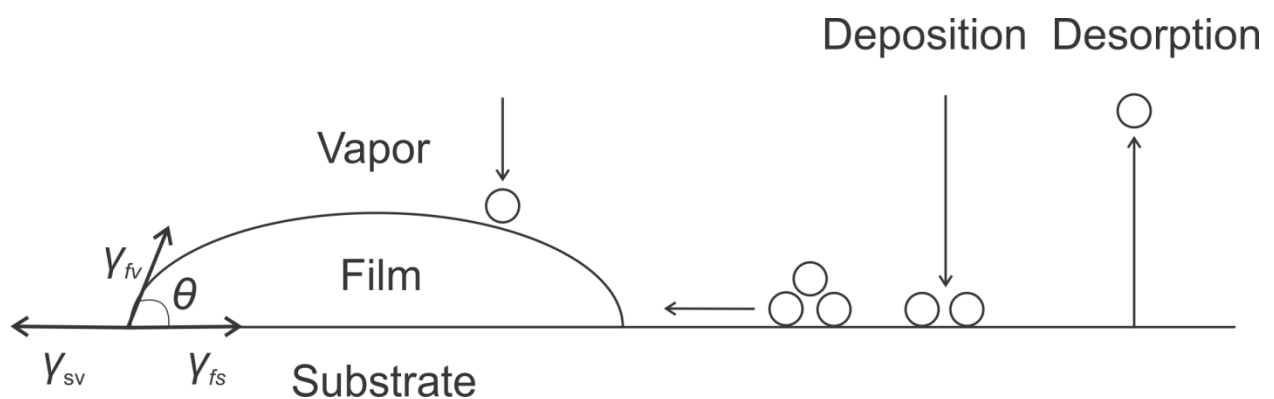


Figure 2.10: Heterogenous nucleation on substrate surface by vapor deposition.

The Young's equation leads to three growth models [92-94]:

- Layer-by-layer or Frank-van der Merwe growth, when $\theta_{wet} \cong 0$ and $\gamma_{sv} \geq \gamma_{fs} + \gamma_{fv}$. The deposit forms layers on the surface because the atoms of the deposit material are more strongly attracted to the substrate than to themselves.
- Island or Volmer-Weber growth, when $\theta_{wet} > 0$ and therefore $\gamma_{sv} < \gamma_{fs} + \gamma_{fv}$. If γ_{fs} is neglected the island growth occurs when the surface tension of the film exceeds that of the substrate. The deposited atoms are more strongly bound to each other than the substrate, tending to cluster up.
- Layer-plus-island or Stranski-Krastanov growth. This is an in-between growth mode where initially $\gamma_{sv} > \gamma_{fs} + \gamma_{fv}$ promoting the formation of a wetting layer and after the first monolayers the system switches to island growth.

The growth of evaporated silver on SiO_2 , due to weak interaction and adsorption, presumably promotes the island type, V-W growth [95].

2.6 Rippled silicon substrates

The processes for producing functional nanostructures vary from chemical processes, cheap but low in control; top-down procedures, high in detail but time and cost expensive; or bottom-up processes, with intermediate values regarding control and cost.

A bottom-up technique for manufacturing templates to be used in the creation of functional metallic nanostructures is *low energy ion bombardment*. During this *sputtering* process, energetic ions collide with the surface driving out the material. A competition between roughening by ion sputtering and surface smoothing mechanisms (e.g. surface diffusion), leads to the formation of ripples on the surface of the target material. The description of the underlying mechanisms for nanopatterned templates falls out of the scope of this thesis. Further details on the phenomenon can be found in references [95-99].

3 Experimental setup

In the following section the experimental setup used in this work is presented. This includes the fabrication process, where silver nanoparticles are deposited via thermal evaporation on the silicon surface followed by chemical functionalization with a self-assembled monolayer. Likewise, the characterization techniques are presented, specifically optical characterization via ellipsometry, spectroscopical characterization via Raman and IR setup and topographic characterization via atomic force microscopy and scanning electron microscopy.

3.1 Thermal evaporation

This technique is used in order to deposit silver nanoparticles on the surface of a substrate of choice. The substrates used were plain silicon wafers (100) or rippled silicon substrates patterned by ion-beam irradiation as described in [96, 100].

The metal film evaporation takes place in the atmosphere of a high vacuum chamber. The pressure during evaporation was kept below 3×10^{-7} mbar with the use of a turbo pump. The sample is mounted on a holder placed in the middle of the chamber. The holder can move in xyz direction as well as tilt in the z axis to enable deposition at a preferred position and angle. In order to achieve high angle of deposition to the surface normal, a wedge was used, on which the silicon substrate was mounted. The evaporator is mounted from a lower port. The electrons from a heated tungsten filament are attracted to the high positive potential of the crucible (Mo) that contains the silver. At 1kV voltage and 7A filament current, 20mA emission current and resulting temperatures over 900°C melt the silver and the vapors are directed to the target substrate. The geometry is controlled so that the incoming beam of evaporated material forms an incidence angle 70° in respect to the normal of the substrate's surface (Figure 3.1).

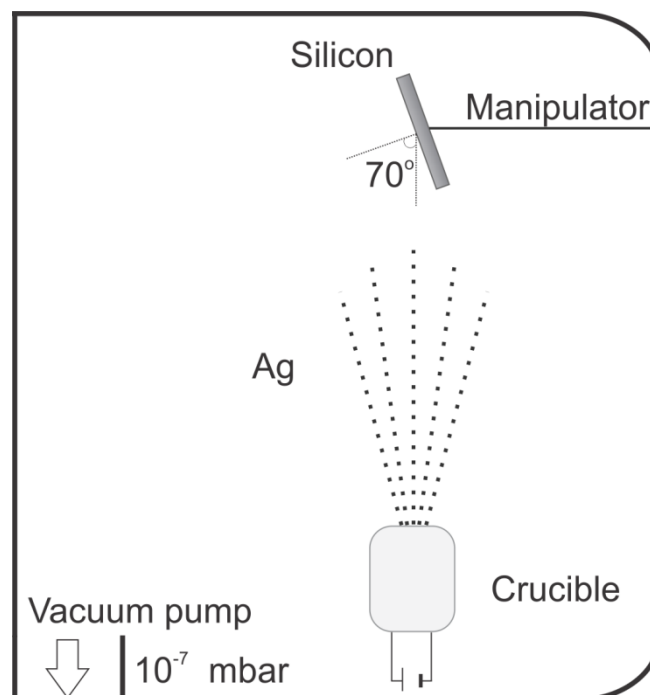


Figure 3.1: Ag evaporation schematics.

3.2 Self-assembled monolayer

Surface modification by adsorption of a self-assembled monolayer (SAM) is used in order to study the sensing applications of the substrate and additionally acts as protection for the nanoisland layer. Immediately following metal deposition, the samples were incubated in a 1 mM solution of 4-mercaptobenzonitrile (4-MBN, Sigma-Aldrich) and DMSO for 18 h, and subsequently washed with ethanol, pure water, and dried with N₂ [101].

3.3 Ellipsometry

The characterization of the optical properties in the UV-Vis region was performed with a SENTECH SE850 ellipsometer in reflectance mode with an incident angle of 70°. Micro-apertures were used to reduce the spot size to 250 µm. For the fitting procedure the SpectraRay3 and WVase software were used.

The separate infrared-ellipsometric setup is externally attached to a Bruker Vertex 70 FT-IR spectrometer, and the measurement was performed in reflectance mode at an incidence angle of 65° and a resolution of 4 cm⁻¹ [27]. As a reference sample an undeposited rippled silicon template was used. IR-ellipsometry involves a wide spot size of a few mm² and therefore a homogenous sample is necessary. The setup was purged with dry air to avoid absorption of the IR radiation by the water vapor.

3.4 Raman scattering spectroscopy

The Raman setup is equipped with an argon laser (Coherent Innova 300c Ar) as well as a Krypton Laser (Sabre Innova Kr) that can produce distinct laser excitation lines, from which mainly the 514 nm and 647 nm were used. An additional diode pumped solid state laser with a 594 nm excitation line was used (Cobolt Mambo 100). The laser beam was focused onto the sample by a Nikon 20× objective with a numerical aperture of 0.35 and a spot size of approximately 2 µm in radius. The laser power on the sample was 1 mW. All SERS spectra were normalized per mW laser power and per second of accumulation time. The spectrometer used is LabRam with a 1200 (1/mm) grating controlled by LabSpec software. It is coupled to an electrically cooled CCD Andor detector. For the spectral line calibration prior to measurements the 520 cm⁻¹ silicon phonon peak was used.

The setup of (Figure 3.2) depicts the laser beam path reflecting on the mirrors (M) and its polarization direction, indicated by the arrows. For enabling polarization measurements a detachable polarizer (P) at the laser output and analyzer (A) can be placed at the spectrometer entrance. The beam is incident on the sample with a specified polarization direction. The scattered light collected through the objective lens passes through the analyzer and is guided to the detector. In order to eliminate any polarization sensitivity of the spectrometer, the analyzed light passes through a quarter-wave plate ($\lambda/4$) transforming the linear light into circularly polarized light before it enters the spectrometer.

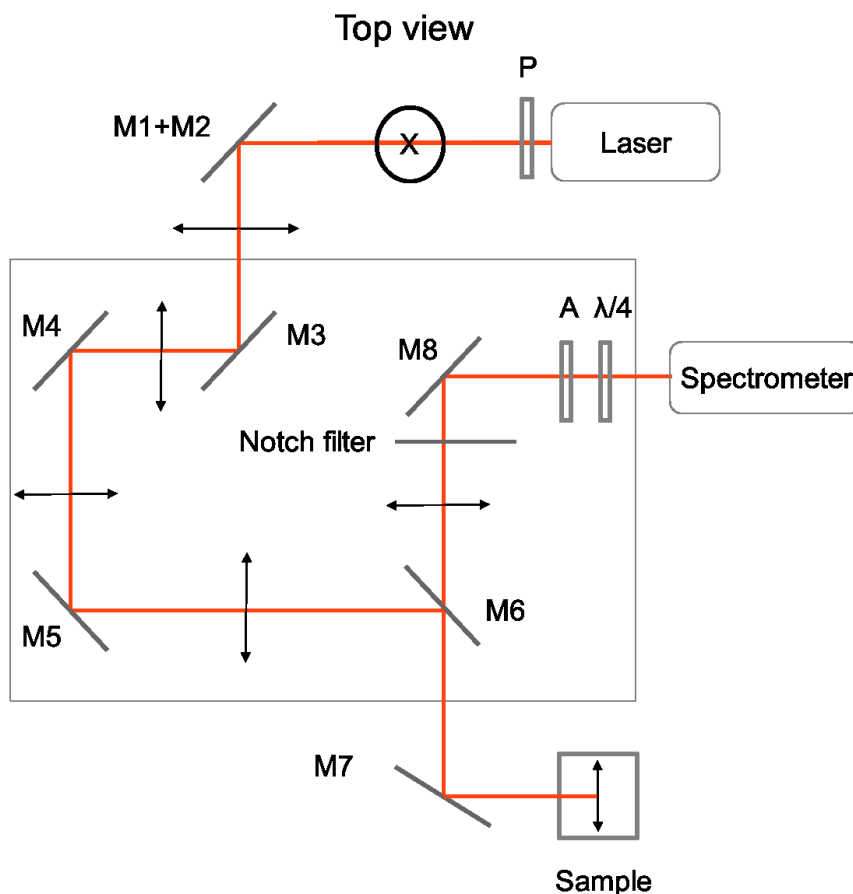


Figure 3.2: The Raman measuring setup following the laser path. M: reflection mirror, P: Polarizer, A: Analyzer. The beam polarization is indicated by the arrows.

3.5 Infrared spectroscopy setup

The infrared measurements in reflectance mode were performed at a Bruker Hyperion 3000 FT-IR microscope with a Cassegrain objective (15×) with numerical aperture of 0.4 and aperture size of 160 μm. A typical measurement had 4000 scans. The sample spectra were referenced to flat Au substrate. Au and Ag have similar behavior in the infrared region and therefore can be used for reference.

By converting the FTIR microscope there is the possibility to extract polarization information, which is useful in the characterization of the samples. A Bruker Hyperion 3000 FTIR is equipped with a set of polarizer and analyzer. Additionally, an Optical Plane Aperture (OPA) in the form of a slit was placed in the throughput of the objective. This slit defines the optical plane of the incident and reflected beam which subsequently can be measured in parallel and cross polarized conditions. As shown in Figure 3.3, the IR beam that passes through the polarizer, involves the polarization direction p , parallel to the plane of incidence while the polarization direction s , perpendicular to the plane of incidence is being blocked by the polarizer. The direction p consists of two contributions, the in-plane

E_{px} and a smaller out-of-plane E_{pz} . The origin of the small E_{pz} contribution is due to the small incidence angle (16°) of the Cassegrain objective. [102]

Both of the setups were purged with dry air to avoid absorption of IR radiation by water vapor.

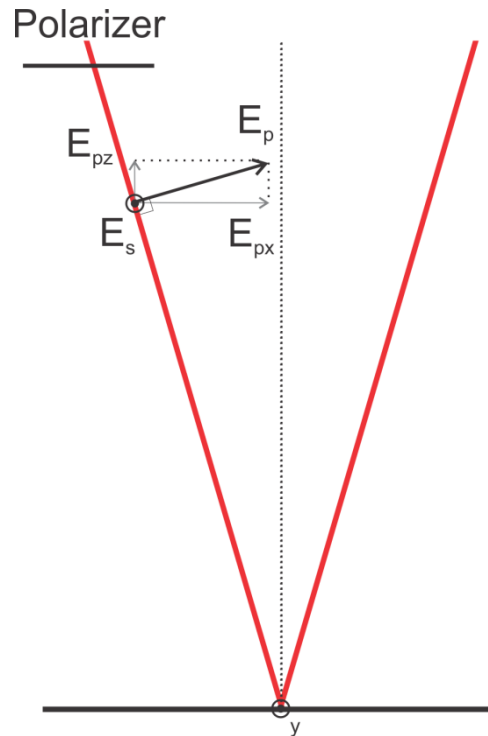


Figure 3.3: Polarization directions of the IR beam that passes through the polarizer.

3.6 Topographic characterization

The characterization of the periodicity of rippled silicon substrates and the thin metal films surface morphology was performed by two basic topographic techniques:

- Atomic force microscopy (AFM) in non-contact mode at a XE-100 atomic force microscope (Park Systems Corp., Suwon, Korea)
- Scanning electron microscopy (SEM) at a Hitachi SU8030 SEM with cold field emitter gun. The images were taken with the upper inlens detector at an accelerating voltage of 3 kV and a beam current of 100 pA.

Image analysis was performed with ImageJ [103] and Gwyddion [104] software, including the Fourier transformation analysis.

3.7 Enhancement factor calculations

SERS

The calculations of the enhancement factor are done according to Ly et al [105].

The Raman Enhancement Factor (REF) is determined by 3-1,

$$REF = \frac{I_{SERS}}{I_R} \frac{N_R}{N_{SERS}} = \frac{I_{SERS}}{I_R} \frac{c_R V}{\Gamma_{SERS} A} \quad 3-1$$

where I_R and I_{SERS} are the Raman intensities of probe molecules in solution and absorbed on the Ag surface respectively. N_R and N_{SERS} refer to the number of molecules in the focus of the laser beam. N_R equals to the concentration of molecules of the solution, $c_R=100$ mM, times the illuminated volume, N_{SERS} equals to the surface concentration Γ_{SERS} , times the illuminated area, A .

The irradiated volume V can be approximated by a cylinder of radius r and height h , while the radius of the focused beam is estimated by McFarland et al. to be $r=2 \mu\text{m}$ for the x20 objective independent of the wavelength [106]. The height of the cylinder can be approximated by the depth of focus of a Gaussian beam:

$$h = 2r^2 \frac{\pi}{\lambda} \quad 3-2$$

For Γ_{SERS} the largest packing density of benzenethiol (BT), $6.8 \cdot 10^{14}$ molecules/cm² [107] was used. The surface area probed by the measurement can be estimated from the SEM pictures. The population and average distribution of the size of nanoparticles is measured by ImageJ. The surface area (A_{REAL}) is calculated by considering silver hemi-ellipsoids and relate it to the area of the SEM picture ($A_{GEOMETRIC}$). In this way an analogy with the roughness factor $RF = \frac{A_{REAL}}{A_{GEOMETRIC}}$ [108] has been generated. Therefore, the interacting illuminating area A , from 3-1, is expressed as $A = RF \cdot \pi r^2$.

The choice of calculating the surface area of the hemi-ellipsoids instead of the flat surface area calculated by the SEM picture is done in order to avoid over-estimation of the EF. For example, analysis of an SEM area (Figure 6.8) gives flat area coverage at 50%, while calculating the silver surface of the ellipsoids, the real area coverage amounts to 60%. On the other hand using the largest packing density of BT could lead to underestimating the EF. As it can be seen, the estimation of EF withholds many presumptions and should be considered with caution [109].

In chapter 6.2, a comparison of the EF of anisotropic substrates with that of a roughened silver electrode is made, in order to compare the efficiency of the substrates with that of a typical SERS substrate. Nanostructured electrodes are extensively used for electrochemical and spectroelectrochemical studies with moderately good SERS properties. For the silver electrode the surface roughness factor is determined by BET measurements to be ca. 20 [105]. For comparison, the roughness factor of the evaporated nanoparticles in the measured SERS active areas varies between approximate values of 0.6 and 1.

SEIRA

Another important step is the evaluation of the molecular signal enhancement by the substrate in the IR region. In collaboration with Christoph Kratz (ISAS), a method to estimate and compare the enhancement of metal island films from the IR-ellipsometric data was found. Specifically, the parameters of the three main 4-MBN peaks at 1476, 1584, 2229 cm^{-1} were extracted by ellipsometric modelling of an 4-MBN monolayer on a flat gold surface. A model was built consisting of the layers Si/native SiO_2 /4-MBN monolayer. The 4-MBN layer was represented by a combination of three harmonic oscillators to account for the three main peaks, with their already specified parameters and the dielectric constant ϵ_∞ as a model parameter. The theoretically simulated $\tan\Psi$ graph was then compared to the experimental data, providing the ratio of the enhancement of the 4-MBN peaks by the existence of silver. The software used was the Sentech SpectraRay3.

Part B: Results

4 Enhancement substrates

The following chapter presents the fabrication process of SERS and SEIRA substrates via silver evaporation on plain and rippled silicon as well as the ellipsometric models that were used to optically characterize them.

4.1.1 Silver deposition on plain silicon

There are a great number of factors that influence the island growth of deposited silver via deposition on the surface of Si (100) with native oxide. These factors are e.g. the beam flux, angle of incidence, annealing or heating of the substrate during deposition, degradation due to atmospheric tarnishing. Below is given an overview of the effects of some of those factors on the silver films.

Deposition characteristics

The morphological evolution of silver nano-islands is strongly connected to factors such as the deposition rate and temperature. It is necessary to have control over the deposition rate that defines as well the growth curve. As discussed in 2.5, deposited silver grows on SiO₂ according to V-W growth, where the silver atoms selectively coalesce with each other forming islands. The incoming flux defines the nucleation and diffusion of the atoms on the surface.

Figure 4.1 shows the dependence of thickness and growth rate on the deposition time. The thickness was estimated using UV-Vis ellipsometry and a simple Si/SiO₂/Ag model in Spectra Ray 3. As expected the Ag layer thickness (black squares) increases over time but with a declining growth rate (blue triangles). The film growth process is mediated by Ostwald ripening where atoms of smaller clusters transfer to larger clusters, via vapor phase and surface diffusion [110]. After an initial rapid growth in nanoparticle size, the growth rate slows down while coarsening between the nanoparticles takes place [111]. The nanoparticle coarsening involves their growth also in the lateral direction, leading to formation of islands. The islands interconnect at increasing deposition time, resembling fractal geometry, and eventually forming a continuous film, which should in turn lead to a linear relation of the thickness over the deposition time [92, 112]. The last area was not observed in Figure 4.1, suggesting that the film is not fully closed yet.

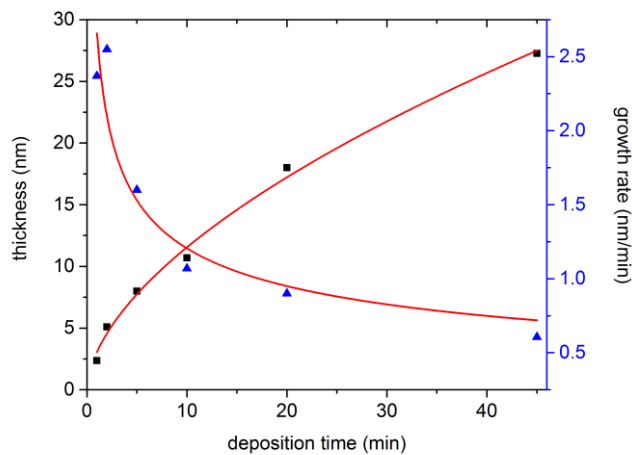


Figure 4.1: Ag layer thickness (black squares) and growth rate (blue triangles) as a function of deposition time.

Figure 4.2 shows the topography of a thick layer of approximate nominal thickness of 40 nm. The film is not entirely closed and the surface presents intense roughness. It has been reported that at room temperature it is difficult to grow continuous silver films of tens of nanometers and the film coalescence happens at hundredths of nanometers [113]. Nevertheless, in this area the film is already percolated. The percolation takes place when the isolated islands coalesce with each other resulting in an increase in electrical conductivity and a rapid change in the optical values, e.g. the effective dielectric function [112, 114].

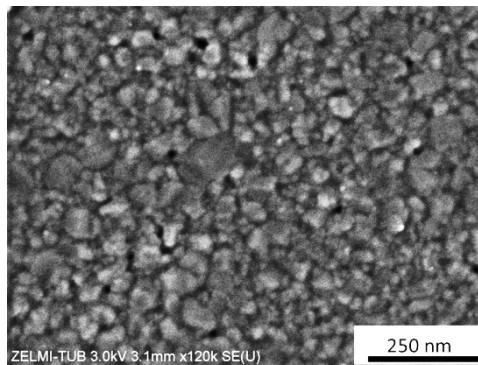


Figure 4.2: SEM image of evaporated Ag layer of nominal thickness 40 nm.

Annealing

In various preparation methods there is a thermal treatment step that involves the heating of the sample. Temperature is another important factor that controls the kinetics of the film growth. The effect is different when the annealing takes place during deposition, after the deposition without breaking the vacuum or after exposing the sample in atmospheric air. In general, high temperature leads to increased surface mobility of atoms and results in agglomeration of the islands [115].

Figure 4.3 shows the AFM topographic image of a deposited silver layer exposed in ambient air (left) and then annealed in 300° for 1 hour (middle). The increase of the nanoisland size is pronounced, from an average of 100 nm for the unannealed sample to 250 nm for the post-annealed sample, with a quasi-spherical shape. The increase of the particle size, changes the plasmonic response of the sample. In Figure 4.3, right, is shown the red-shifting of the imaginary part of the pseudodielectric function after the annealing procedure.

During exposure in ambient air the atmospheric oxygen is chemisorbed on the Ag nanoparticles, decreasing the surface energy. The annealing takes place after the growth process has ended, where the clusters are already formed. The main mechanism is not the diffusion of adatoms on the surface but the reshaping of the clusters in order to achieve minimal surface energy, which leads to spherical shape [95].

Regarding the deposition of Ag on rippled silicon substrates, the annealing-induced spherical shape would contradict the effort of producing anisotropic nanoparticles with aspect ratio. Therefore, the depositions were performed at room temperature.

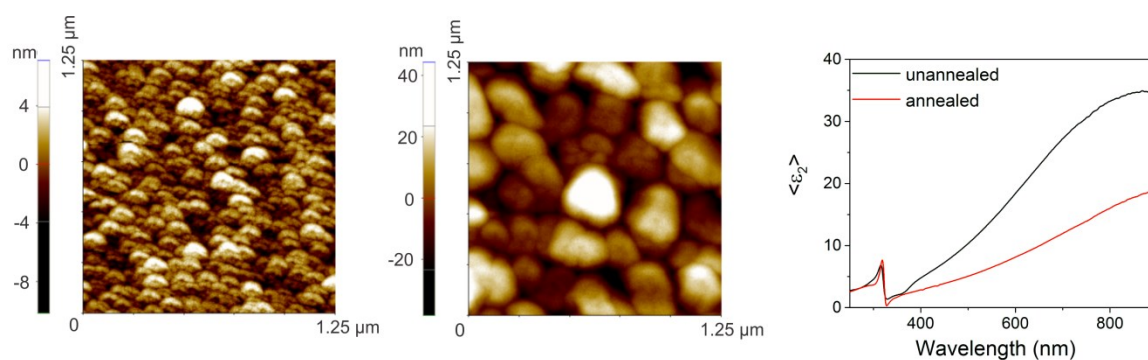


Figure 4.3: AFM topography of Ag nano-islands before (left) and after (middle) annealing for 1 hour at 300°. Right, is the corresponding imaginary part of the pseudodielectric function.

Time degradation

Compared to gold, which is inert, silver has the disadvantage of atmospheric tarnishing. The effect is quite influential for nanoparticles due to their high surface-to-volume ratio, where the nanoparticle size and distribution impacts the oxidation rate. Oates et al. have shown that for similarly produced samples left in ambient air, the tarnishing is due to oxidation rather than sulfidation [116]. Atomic oxygen combines with silver forming an AgO layer and catalyzes the recombination of more oxygen creating AgO₂ [117].

For sensing purposed devices it is important to define the extent of oxydation as it will in turn define the shelf-life of the product. It is well known that self-assembled monolayers can be used to protect silver from tarnishing [118]. Qi et al. report that benzenethiol layer protected the silver nanoparticles for more than ten days [119]. In this case the SAM has the dual role of protection and chemical functionalization for sensing purposes.

Measurements on the present samples (Figure 4.4) have shown a minor red shift of the resonance after ten days and a definitely oxidized state after two months of exposure to ambient air. To avoid signal deterioration due to oxidation, all measurements were performed to samples no older than two weeks.

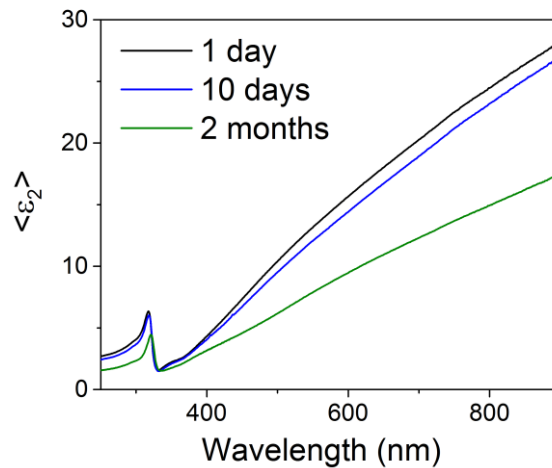


Figure 4.4: Optical response due to time degradation of Ag nanoparticles after 4-MBN adsorption.

4.1.2 Silver deposition on rippled silicon

Controlled silver deposition on silicon templates is one possibility for tailoring plasmonic properties. An additional possibility for tuning the plasmonic properties can be achieved with the surface modification of the supporting template, i.e. the use of a rippled silicon template. The metal deposition on plain silicon results in isotropic properties in the xy plane. With the use of rippled silicon instead, the plasmonic response differs in the x and y axes, creating optically anisotropic substrates.

The rippled surface is created by the bombardment of Ar⁺ ions on an epi-polished Si (100) substrate. Mukesh and Keller have concluded that the optimal ion incident angle is at 67° with respect to the surface normal (schematics in Figure 4.5) [95, 96]. The templates used in this study were bombarded by ion flux in the range of 10¹⁷-10¹⁸ cm⁻² and kinetic energies of 500 eV and 800 eV resulting in ripple periodicity of ~45 nm and ~30 nm, respectively. The fabrication of rippled silicon substrates has been extensively studied by the Ion induced Nanostructures group of Dr. Stefan Facsko, Helmholtz-Zentrum Dresden-Rossendorf. The templates used in the present work were fabricated in the same lab with the collaboration of Benjamin Schreiber.

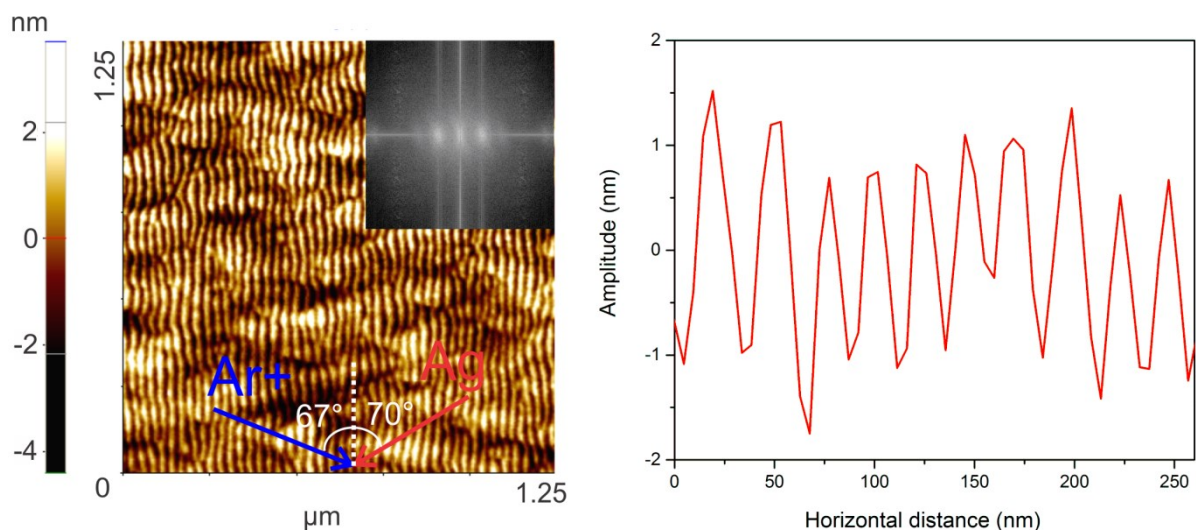


Figure 4.5: Left, AFM topography of a rippled substrate. The Fourier transform, inset, illustrates the strong periodicity. The colored arrows note the direction of the incoming ion beam and the Ag evaporation. Right, the ripple amplitude along a line scan. The ripple periodicity is ~25 nm.

Figure 4.5, left, shows the rippled surface pattern as a result of ion beam bombardment on silicon. The AFM-derived periodicity is ~25 nm, while the ripple height is around 2 nm (Figure 4.5, right). The Fast Fourier Transformation shown in the inset of Figure 4.5 displays the periodicity and ripple quality. The bright spots represent the characteristic spatial frequency and the direction of the spots stands for the direction of the wave vector of the periodic structure.

Extensive experiments by Dr. Ranjan Mukesh [95] concluded that the silver vapor deposition scheme producing better quality self-aligned nanoarrays is for deposition angle at 70°, with respect to the surface normal and direction opposite to that of the incoming ion beam that formed the ripples (schematics in Figure 4.5, left). The silver atoms nucleate on the ridges of the ripples and clustering is observed. Depending on the deposition rate and time, the nanoparticles, initially spherical (Figure 4.6, left) will grow and coalesce along the ridge forming aligned arrays of nanoparticles with various aspect ratios (Figure 4.6, right).

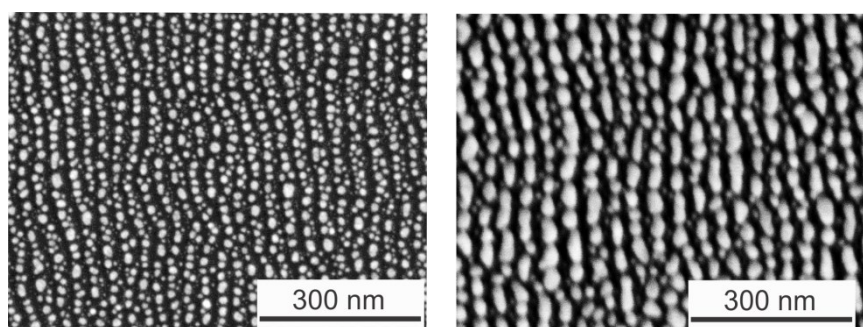


Figure 4.6: SEM images depicting the growth of silver on ripples with periodicity ~25 nm. The nominal thickness is 8 nm (left) and 16 nm (right).

Due to the preferential growth of the metal particles along the ripples, there are two optical axes created: one perpendicular (\perp) and one parallel (\parallel) to the ripples. Along these axes the optical resonances differ according to the different nanoparticle sizes (Figure 4.7, left). The perpendicular direction has a resonance at lower wavelengths while the one parallel to the ripples direction presents a red-shifted resonance, attributed to the increased nanoparticle length in this direction (Figure 4.7, right). Extended discussion on the optical properties of these structures takes place in chapter 6.1.

Ripples with lower periodicity exhibit better ripple quality compared to the larger periodicity ripples of $\sim 40\text{-}50$ nm that present increased roughness. Nevertheless, depositions with varying ripple periodicity and deposition time allow concluding that for samples with pronounced optical anisotropy, larger ripple periodicity is preferred. This can be attributed to the fact that during the nanoparticle growth, at a certain point the height and width will exceed the limited ridge area and grow above the ripples. Therefore at a template with smaller ripple periodicity the deposited silver will grow over the ripples and start coalescing in all directions, before the resonance in the direction along the ripples has reached the infrared region, therefore limiting the optical anisotropy range.

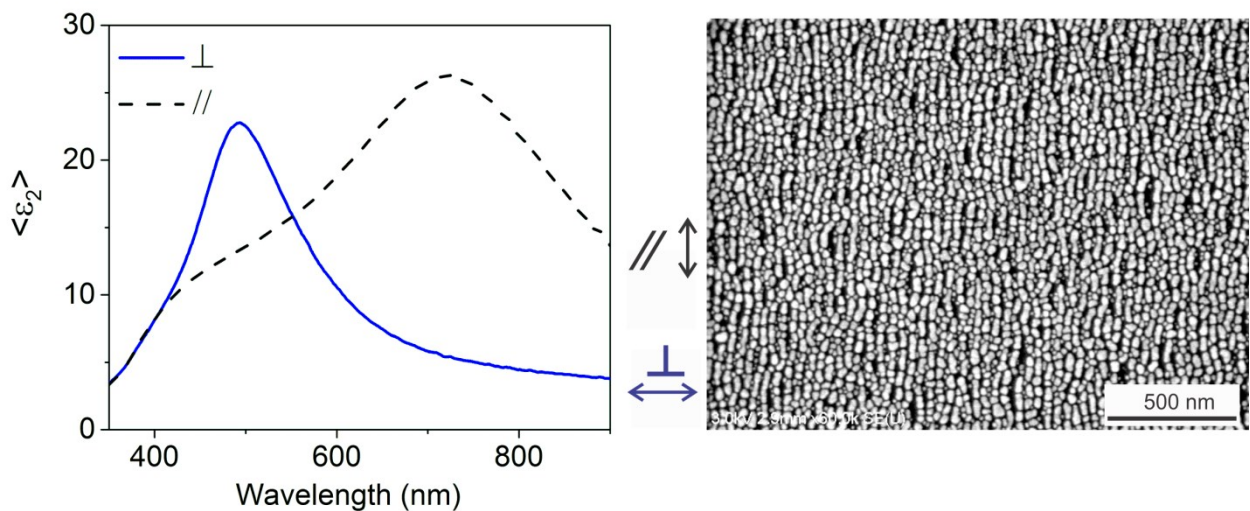


Figure 4.7: Left, imaginary part of the pseudodielectric function corresponding to the excitation direction perpendicular (blue solid line) and parallel (black dashed line) to the ripples. Right, SEM image of the corresponding topography.

4.2 Optical properties

Ellipsometry in the present work is used as a tool for determination of the silver layer thickness, important for the deposition control. Additionally, a simple measurement of ellipsometry can give an indication for the wavelength of the plasmonic resonances via the pseudodielectric function (see Eq.2-12). This provides a quick estimation of the sample suitability for Raman and IR purposes and the choice of excitation. Nevertheless, proper modelling is necessary for better thickness estimation as well as for extracting the effective dielectric function of the layer in order to further study the optical properties. The optical properties of similar structures have been thoroughly investigated with the use of ellipsometry by Oates et al. [38, 120]. However, a complete optical investigation is outside the scope of this work. In this chapter are presented the basic models used for extracting information from silver deposited on plain and rippled silicon.

Silver on plain silicon

A common approach to the modeling of metal island films is the effective medium approximation, Maxwell-Garnet for low coverage and Bruggeman for close-to-percolation layers [29, 121]. Alternatively, Oates et al. [38] proposed the use of an anisotropic layer model consisting of oscillators for improved fitting of Ag island films.

According to that approach, the fitting quality of an isotropic versus a uniaxial model for silver nanoisland layers of different thicknesses was compared. The isotropic model consisted of the layers Si/SiO₂(2 nm)/Ag. The Ag layer was modeled with a Lorentz oscillator accounting for the localized plasmon resonance that is converted to a Drude oscillator for increased thickness. A Tauc-Lorentz oscillator accounts for the interband transition. The energy of the Tauc-Lorentz is set at 3.8 eV corresponding to the interband transition 4d-5s [122]. The uniaxial model considers a different dielectric function for the in-plane and out-of-plane direction. The in-plane layer is modelled by a Tauc-Lorentz and Lorentz oscillator (occasionally a second Lorentz) for small thickness and with a Tauc-Lorentz and a Drude oscillator for larger thickness. The out-of-plane direction (z axis) is treated as bulk silver, approximated by a model with a Drude and a Tauc-Lorentz oscillator. Corrected to account for the differences from bulk silver, the broadening parameter of the Drude oscillator increases due to the increased surface scattering. Accordingly, the amplitude parameter decreases to account for the decreased effective electron density [38, 123]. An extra Lorentz oscillator with small amplitude is added to account for the “bump” observed at 3.6 eV, visible in Figure 4.8 for thickness of 29 nm and above.

Table 1 compares the resulting fit values of thickness and the corresponding mean squared error (MSE) of the two models for different samples. Both of the models perform better with increasing thickness. The uniaxial model has generally lower MSE values than the isotropic, indicating improved fitting with the treatment of in-plane and out-of-plane layers individually.

| Deposition time (mins) | Model | Thickness (nm) | MSE |
|------------------------|-----------|----------------|-----|
| 5 | Isotropic | 7.4± 0.04 | 33 |
| | Uniaxial | 7.29± 0.019 | 21 |
| 10 | Isotropic | 10.2± 0.11 | 43 |
| | Uniaxial | 11.7± 0.14 | 14 |
| 20 | Isotropic | 16.67± 0.12 | 32 |
| | Uniaxial | 18.47± 0.08 | 19 |
| 45 | Isotropic | 28.2± 0.13 | 23 |
| | Uniaxial | 29.46± 0.06 | 11 |
| 60 | Isotropic | 35± 0.17 | 12 |
| | Uniaxial | 32± 0.18 | 7 |
| 120 | Isotropic | 70± 0.44 | 14 |
| | Uniaxial | 76± 2.1 | 10 |

Table 1: Fitted thickness and corresponding MSE of the isotropic and uniaxial model for different thickness samples.

Figure 4.8 presents the fitting results of the uniaxial model. Figure 4.8 (left) shows the experimental and fitted Ψ and Δ values. The interband transition is expressed as the pronounced feature at Ψ - Δ graph visible at 3.8 eV. As the thickness increases, a volume plasmon is generated close to the plasma energy of silver, following the bulk plasmon condition of $\epsilon_1=0$. Figure 4.8 (middle) shows the real, ϵ_{xy1} , and imaginary, ϵ_{xy2} , part of the dielectric function of the in-plane layer. The localized surface plasmonic resonance represented by a Lorentz oscillator, red-shifts with increasing thickness. For thickness above 29 nm a better agreement is found with a Drude oscillator, since the central frequency of a potential Lorentz oscillator is outside of the investigated energy range. Figure 4.8 (right) shows the real, ϵ_{z1} , and imaginary, ϵ_{z2} , part of the dielectric function of the out-of-plane layer. As already discussed, it consists of a Drude and a Tauc-Lorentz oscillator with modified values to account for the differences from the bulk silver.

A surface plasmon polariton is generated at the interface of two materials at the condition that interface is between a dielectric and a metal, therefore the $\epsilon_1 < 0$. As it is seen in Figure 4.8, the real part of the dielectric function for the in-plane layer exhibits a metallic behavior in the form of a Drude for energies under 3.8 eV and thicknesses over 29 nm. This coincides with the appearance of a “tip” at 3.6 eV, presumably a surface plasmon polariton resonance. Oates et al. have demonstrated the strong dependence of this resonance on the angle of incidence [29].

Figure 4.9, shows details of Figure 4.8, i.e. the dielectric functions of the in-plane and out-of-plane layers of a thin (7 nm) and a thick (32 nm) silver layer. Here, one can see in detail the transition of the in-plane layer from (a) Lorentz oscillator to (c) Drude model. Also can be seen the decrease of the Drude broadening on the out-of-plane layer from (b) thinner to (d) thicker sample accounting to the increased electron mean free path (Eq. 2-19).

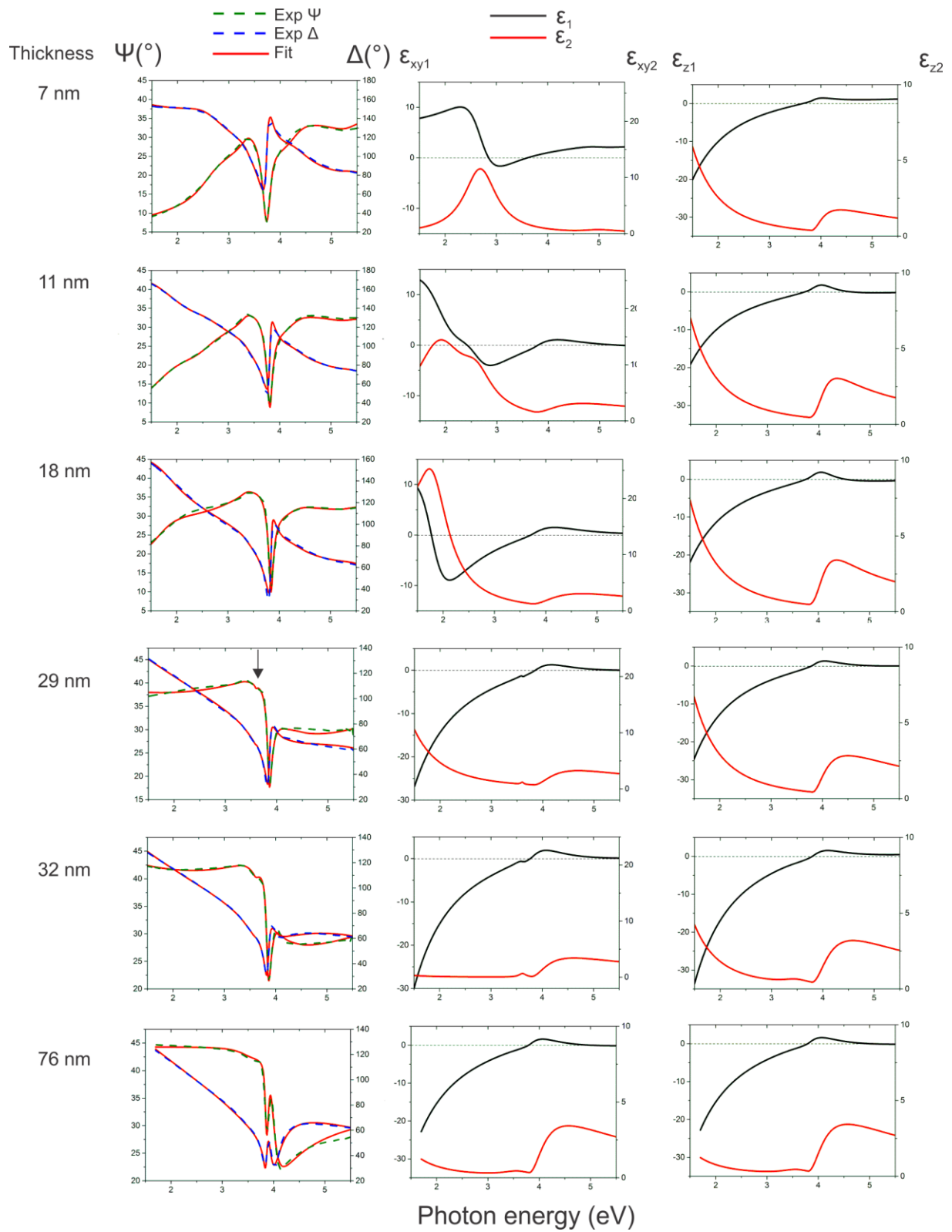


Figure 4.8: (left) experimental and fitted Ψ and Δ values with the corresponding (middle) ϵ_{xy} and (right) ϵ_z model layers of the uniaxial model for different Ag layer thicknesses. The arrow at 3.6 eV points to the surface plasmon polariton.

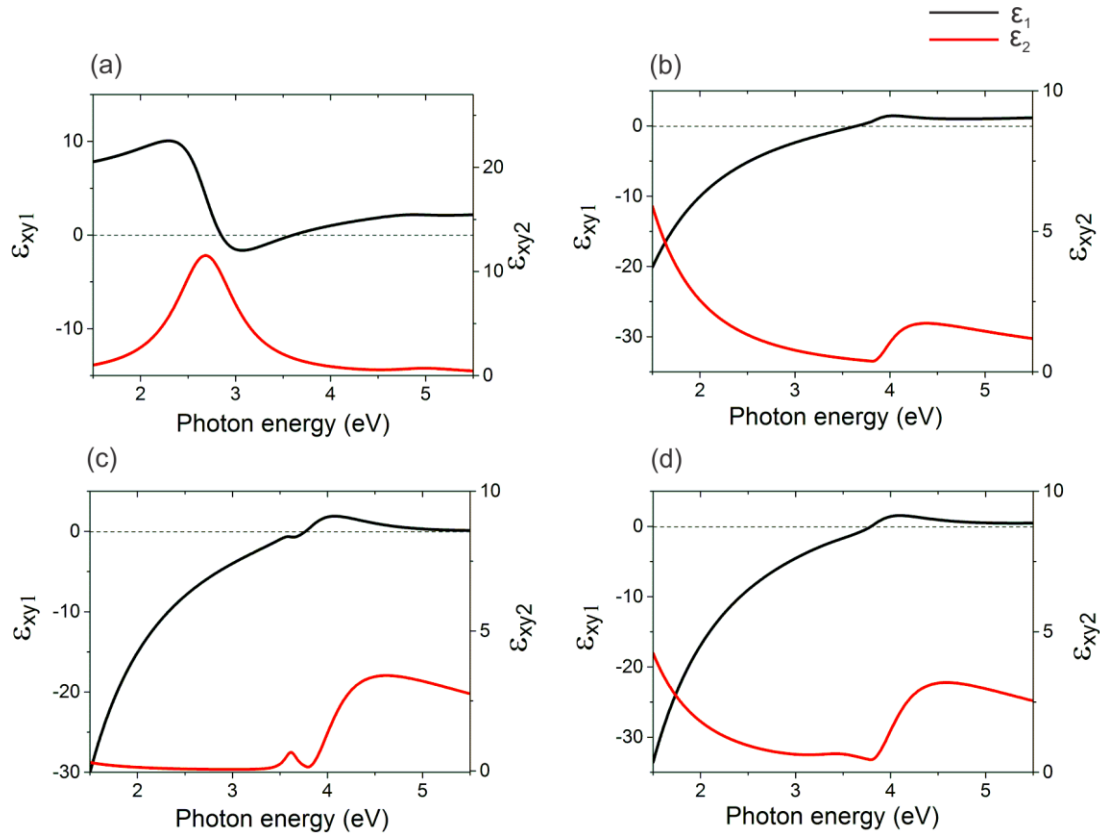


Figure 4.9: (a) ϵ_{xy} and (b) ϵ_z of a 7 nm Ag layer and (c) ϵ_{xy} , (d) ϵ_z of a 32 nm layer.

The presented results aim to discuss the uniaxial modelling approach and compare it with other approaches of optical modeling of metal island films. The fitting was performed for the angle of incidence of 70° . A more precise evaluation would require ellipsometric measurements of variable angles of incidence.

Silver on rippled silicon

Fitting for thickness determination of an optically anisotropic sample is lacking purpose since the different probing directions correspond to different effective thicknesses. Instead, to describe the thickness of such samples the nominal thickness is used, as it has been estimated from the deposition rate and time.

However, some degree of modeling was performed in order to extract the optical resonances responsible for the surface enhanced properties and to study their behavior. The ellipsometric data are modeled to extract the effective dielectric function, $\epsilon(\omega)=\epsilon_1(\omega)-i\epsilon_2(\omega)$ of the Ag island film by using a procedure similar to the one used in the modeling of silver on plain silicon. A biaxial model consisting of the optical layers Si/SiO₂(3 nm)/Ag was used to extract the effective functions of the Ag island film for the two separate probing directions, perpendicular and parallel to the ripples axes. The out-of-plane direction is treated in a similar way as in silver on plain silicon (see above). The in-plane layer was approximated by a Brendel Oscillator model, which is in essence a harmonic oscillator broadened by a Gaussian distribution [124]. The fitting procedure was performed by PD Dr.

Hinrichs at the In-Situ spectroscopy group of ISAS Berlin. Results and details on the subject are presented in chapter 6.1.

5 Self-assembled monolayer

A self-assembled monolayer (SAM) is a one-molecule thick layer comprised of highly-ordered monomers attached on a surface. The applications of SAMs have been increasing in the past decades spreading in a wide variety of fields, e.g. in organic electronics [125], photolithography [126], as protective coatings against corrosion and oxidation [127]. An important application of SAMs is in bioanalytics, where they chemically functionalize surfaces to allow the adsorption of e.g. proteins, DNA and antibodies [128]. Combined with metal island substrates, the increased sensitivity due to surface enhancement, acquires the additional selectivity due to the SAM, resulting in an efficient sensing device by SERS and SEIRA [129].

In the presented work the chosen SAM is 4-mercaptobenzonitrile (4-MBN). The monomer is comprised of a thiol head group that binds covalently to the metal, an organic-tail of a benzene ring and a terminal group of a triple CN bond (Figure 5.1). As an organo-thiol molecule, 4-MBN has high affinity to coinage metals [130]. The distance between the S and N atom is measured to be 7.3 Å (Avogadro, open-source molecular builder and visualization tool, [131]). The IR absorption peak of the CN bond does not overlap with the water bonds absorption, enabling the detection of the molecule even in IR setups without air purging and thereby maintaining the focus on potential simultaneous Raman and IR sensing devices. 4-MBN, similar to other aromatic nitriles, is also an important vibrational Stark effect reporter. The CN stretching mode frequency is shifted by changes of the electric field, thereby providing information on the electrostatic environment [101].

For the SAM formation the metal surface has to be incubated for several hours in a homogenous solution of the monomer in an organic solvent (Chapter 3.2). The head group binds to the surface and the van der Waals interactions of the organic tail groups bring the monomers together and promote organization. The molecular layer forms a tilt angle to the surface normal depending on factors such as the substrate, metal-S bond, the chemical environment of the solution. In literature, for thiophenol on Ag a tilt angle value of 24-27° was reported [132, 133].

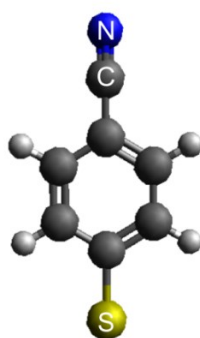


Figure 5.1: 4-mercaptobenzonitrile (4-MBN) molecule.

Figure 5.2 shows the calculated vibrational frequencies of an unbound 4-MBN molecule [134, 135]. The vibrational frequencies are shifted and the relative intensities altered compared to experimental measurements on the surface-bound molecule due to the

attachment of the molecule on the surface and the inherent error of the quantum mechanical approach. The peaks are assigned to normal mode vibrations of the benzene ring, except for the intense peak at 2317 cm^{-1} that is the stretching of the CN triple bond. Experimentally, this peak is observed around 2230 cm^{-1} . Figure 5.3 shows the Raman spectrum of unbound 4-MBN in powder form (above) and the SERS spectrum of the adsorbed 4-MBN monolayer on silver nano-islands (below). The CN related peak which is the strongest in the theoretical calculations and the unbound mode, has less intensity compared to the other peaks in the adsorbed 4-MBN. This is related to surface enhancement effects deriving from the orientation and local symmetry of the adsorbed molecule on the surface [136].

UV-Vis absorption measurements revealed that the electronically excited states of the molecule are in the UV region, therefore the Raman scattering is in non-resonant mode.

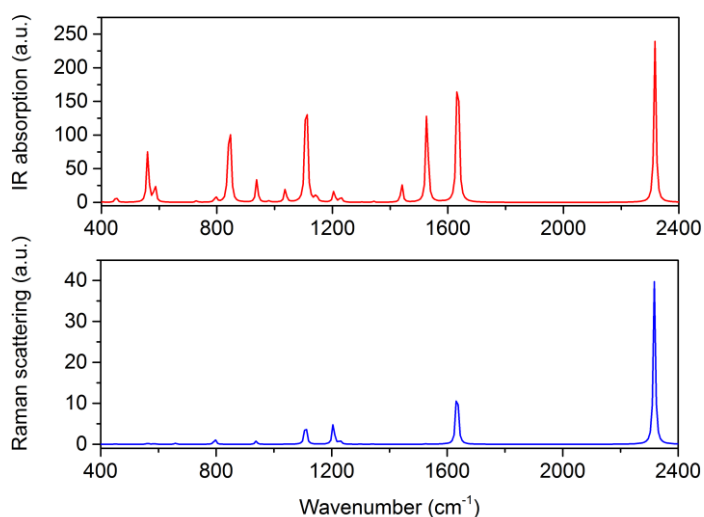


Figure 5.2: Calculated IR and Raman active vibrational frequencies.

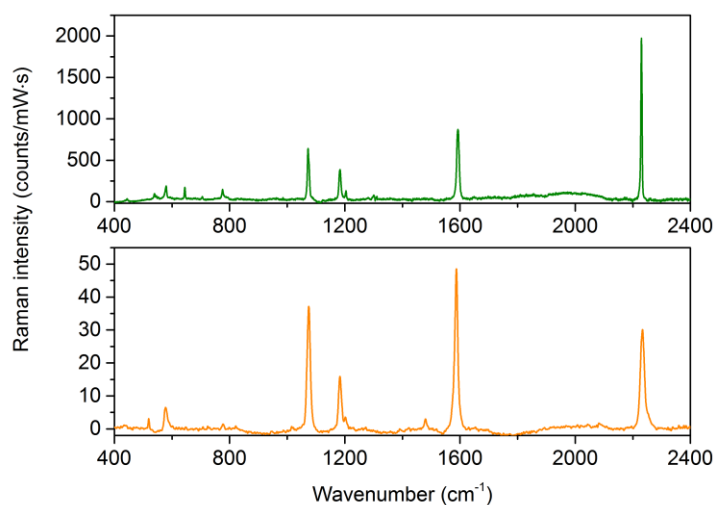


Figure 5.3: Raman spectra of unbound 4-MBN (above) and 4-MBN adsorbed on silver islands (below).

6 Optical characterization of anisotropic nanoparticle arrays

Chapter 6 presents comprehensive results regarding the optical properties, surface enhanced Raman scattering and infrared absorption responses of the anisotropic nanoparticle arrays. Polarization dependent measurements were used in order to bring out the optical anisotropic properties of the substrates.

6.1 Ellipsometry supported by computational electromagnetic calculations

The following part is a study of the optical properties of anisotropic Ag nanoparticle arrays by performing a qualitative comparison between experimental and theoretical results. Spectroscopic ellipsometry was used along with numerical calculations using finite-difference time-domain (FDTD) method and rigorous coupled wave analysis (RCWA) to reveal trends in the optical and geometrical properties of the nanoparticle arrays.

Background

Ellipsometry, as a polarization-dependent non-destructive technique, measures quantities highly important for the optical characterization of anisotropic photonic and plasmonic material surfaces. By using optical models for the spectra interpretation, detailed layer or structure information can be extracted. However, the complexity of the modeling scales with the complexity of the sample structure [137].

Computational calculations that solve the full vectorial Maxwell equations provide a quantitative description of optical properties and may guide the design of optical devices. Rigorous coupled wave analysis (RCWA) and finite-difference time-domain (FDTD) are common used methods for modeling periodic optical structures with predefined material refractive and absorption indices n and k . RCWA is a widely used frequency-domain method that describes two-dimensional periodic structures providing fast and accurate results in the far-field regime using Fourier harmonics, although approaches were recently developed to address the near-field limit as well [138-140]. On the other hand, the optical properties of complex systems in the near-field limit can be more effectively treated by mesh-based FDTD. FDTD is a time-domain method for solving the Maxwell equations that allows for accurate calculations of the electromagnetic field even for arbitrary structures but it is time and resource-demanding [141]. Under certain conditions FDTD methods can be applied for the calculation of far-field responses [142, 143].

Combining interpretation of ellipsometric spectra with the mentioned Maxwell equation solving methods is therefore expected to improve the evaluations by relating known structural parameters with optical properties leading to advanced characterization of nanostructures. There have been a few approaches investigating the use of numerical calculations in ellipsometric analyses [142, 144, 145]. In this work, ellipsometry together with FDTD and RCWA calculations were employed in order to analyze trends of the optical properties of arrays of anisotropic Ag nanoparticles. A first approach of numerical modeling for these structures was presented in [146].

Methods and results

Silicon(100) surface was patterned by ion beam irradiation following procedures described previously by Oates et al and Keller et al [96, 100]. The irradiation induces surface effects resulting in a rippled nanostructured surface with controlled ripple periodicity. The rippled substrate was placed in a high vacuum chamber and Ag was deposited by thermal evaporation at an oblique angle of 70° with respect to the surface normal. The pressure during deposition was 3×10^{-7} mbar.

The optical properties were measured with a rotating analyzer ellipsometer (SENTECH SE850) at 70° angle of incidence. The ellipsometric data are modeled to extract the effective dielectric function [147]. An optical layer model air/ 18 nm Ag island film/ 3 nm SiO₂/ Si was used. A biaxial model was used to extract the effective functions of the Ag island film for the two separate probing directions along the x and y axes. The out-of-plane direction (z axis) of the dielectric function is treated as a layer with equal silver and air fraction [38, 123]. The in-plane components of the dielectric function were described in the frame of a Brendel Oscillator model [124].

For the numerical methods [148], a statistics-based x/y-periodic Ag ellipsoid model (Figure 6.1) of the sample was built based on the mathematical average of the nanoparticles size, as estimated from SEM topographic information. The model also included the structural tilt of the rippled substrate that has been already described for this type of samples [38, 98]. The n and k data for silver were taken from Rakic [149]. All optical calculations, i.e. FDTD for the near-field and RCWA for the far-field limit, were performed using the commercially available RSoft Photonic Component Design Suite 2015.

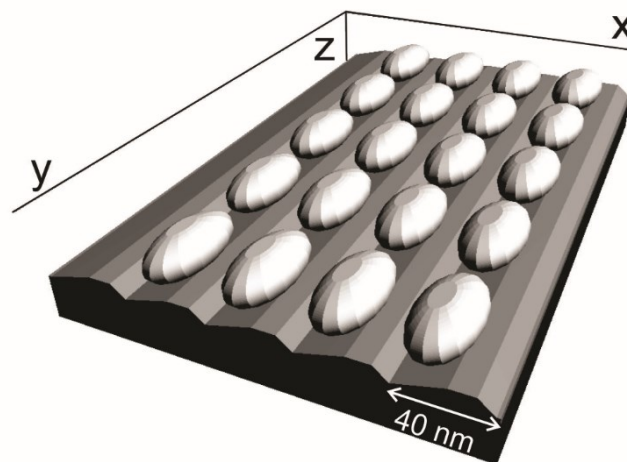


Figure 6.1: Statistics-based x/y-periodic Ag ellipsoid model of the sample. The size of the nanoparticles is 26 and 45 nm at the x and y directions, respectively. Reprinted with permission from [150].

During evaporation at oblique angle, Ag grows preferentially along the ripples forming arrays of nanorods. The pre-patterned silicon substrate has ripple periodicity of 40 nm and the nominal thickness of the Ag layer is 18 nm. Statistics for the nanoparticles were calculated by an SEM image with dimensions 2125 nm x 1593 nm (detail of the sample in

Figure 6.2, left). The nanoparticles cover about 50% of the total surface area. The nanoparticle size distribution reveals an arithmetic mean of length values of 26 nm for the short axis and 45 nm for the long axis, corresponding to an aspect ratio of 1.7 (Figure 6.2, right). The length distribution in the y direction is broader than in the x direction. This is attributed to the ripples that hinder the particle growth along the x axis.

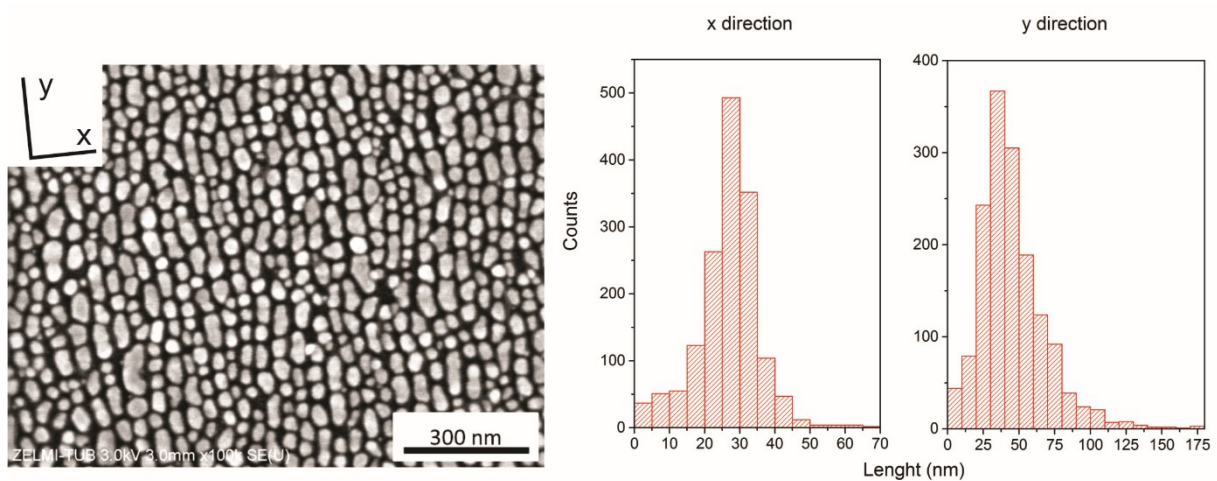


Figure 6.2: Left, SEM image showing Ag nanoparticles deposited along the silicon substrate ripples. The particle long axis of the islands is aligned parallel to the ripples. Right, particle size distribution for the x and y directions. Reprinted with permission from [150].

Contrary to top-down fabrication methods such as electron beam lithography, that create highly uniform but time- and cost-demanding structures [151], our sample is relatively time- and cost-effective albeit at the expense of a broader particle size dispersion. Fourier transformation converts the image from the spatial domain to the k -space [152]. The 2D-FFT shown in Figure 6.3, depicts two bright spots representing the spatial frequency of the periodic structure, along the x axis. The halo-like area accounts for the non-uniformity due to varying nanoparticle size. The restriction at the x axis that is induced by the ripples inserts a limitation to the nanoparticle length in that direction. Whereas such a restriction does not exist along the y axis, resulting in an array of anisotropically shaped nanoparticles.

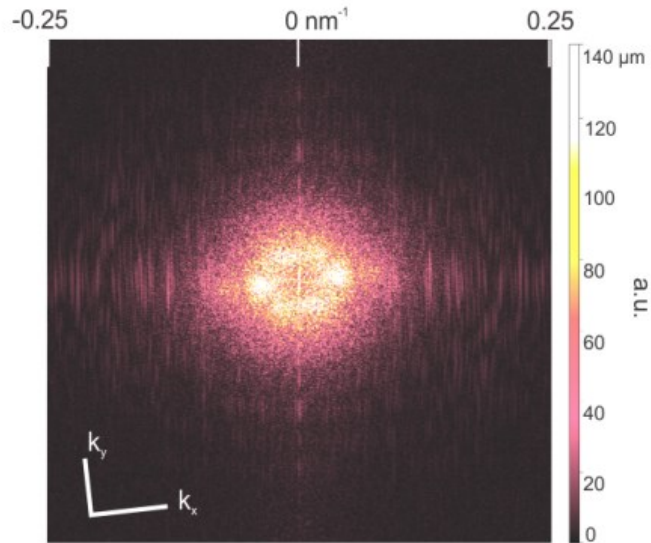


Figure 6.3: Fourier transformation of the SEM image showing increased periodicity at the x axis.

After confirming structural anisotropy, ellipsometric measurements were performed with the incident plane across and along the ripples in order to examine the optical anisotropy of the sample. The raw data at a specific incidence angle, Ψ and Δ , can be directly converted into the pseudo-absorption index $\langle k \rangle$ (Figure 6.4, left) describing the absorption of the sample as a whole. In order to extract the values of the silver layer alone, a model has to be used. The measured values were fitted with the model described in the Methods section. The MSE of the fitting was 3.03. The optical resonance for the x direction shows a peak at lower wavelengths while the resonance along the ripples (y direction) is red-shifted and more intense. Figure 6.4, right, shows the absorption index k presenting maxima at 468 nm and 667 nm for the x and y axis, respectively.

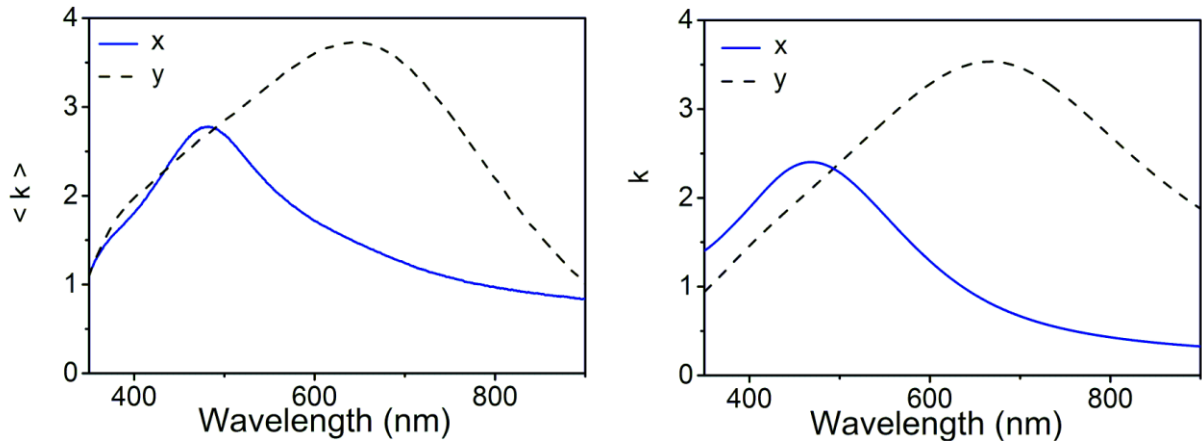


Figure 6.4: Left, ellipsometrically determined pseudo-absorption index for 70° angle of incidence of the sample for the two orthogonal directions, across (\perp) and along the ripples ($//$). Right, absorption index of the nanoparticle layer as determined from the described model. The maximum absorption appears at 468 nm and 667 nm for the x and y axis, respectively. Reprinted with permission from [150].

For the numerical calculations, an arithmetic mean-based periodic model was generated (Figure 6.1) from the experimentally determined surface topology (Figure 6.2), using ripple periodicity of 40 nm, SiO_2 layer of 3 nm thickness, ellipsoid height of 18 nm, particle coverage of 49.3%, ellipsoid aspect ratio 1.7, and x and y separation of the nearest neighbors of 9 nm and 11 nm, respectively.

FDTD near-field simulations show the two localized dipolar plasmon resonances, the physical origin of the two peaks seen in the measurements (Figure 6.5). Both $|E|_x$ and $|E|_y$ are normalized to maximum of $|E|_x$. The dipole in the y direction is stronger due to the geometry of elongated ellipsoids along the ripples and couples better to the incident E-field (E_{inc}). As a result, a stronger and broader far-field peak is obtained in the y direction and a smaller and narrower peak in the x direction, in line with the experimental data (Figure 6.4).

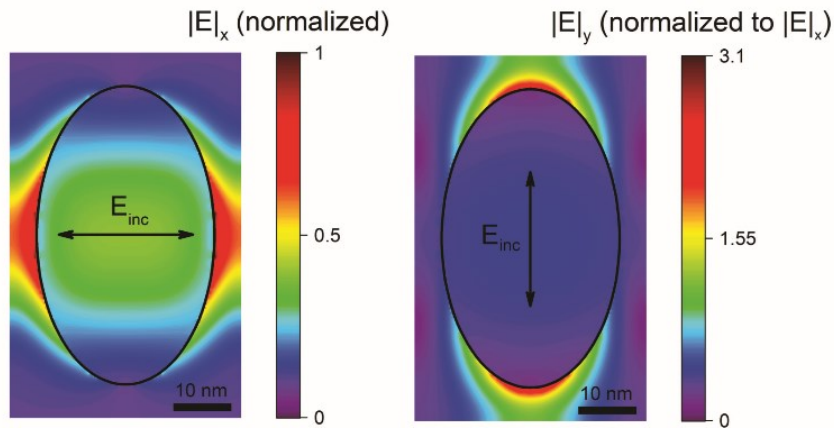


Figure 6.5: Near-field simulations showing the amplitude of the total near-field under periodic boundary conditions (z -direction cut through the unit cell) at the k_x (left) and k_y (right) maxima. Reprinted with permission from ref. [146].

Figure 6.6 shows the results of the far-field RCWA calculations, indicating how the electromagnetic coupling between the adjacent ellipsoids affects the absorption for x - and y - polarized E -field at normal incidence (left and right, respectively). In order to tune the nearest neighbors' coupling strength, the separation distance between the ellipsoids was varied in one direction leaving the other direction unchanged. Increasing the distances (higher separation) reduces the coupling, i.e. the overlap of the near-field hot spots shown in Figure 6.5. Here can be defined a strong coupling regime for about 3 nm separation distance, and a weak coupling regime for 45 nm separation distance.

The statistics-based periodic three-dimensional model (Figure 6.1) predicts a peak position in the x direction that is slightly red-shifted, at 498 nm, compared to the measured one at 468 nm taken from Figure 6.4, right. The red shift is maintained even in the weak coupling regime, at 45 nm separation distance. This finding suggests that the experimental dipolar plasmonic resonances in the x direction are decoupled. However, the decoupling could result from the asymmetric distribution of particle shape anisotropy shown in Figure 6.2 and consist of both localized, single particle plasmonic effects and weak or absent mutual electromagnetic coupling interactions. For a statistically-based periodic model it remains a challenge to distinguish the two contributions. The case is different for the y direction, where coupling effects are rather likely [153, 154]. Here, a better agreement between the statistics-based model calculations and experiments is obtained since the measured peak position almost coincides with the simulated one (667 and 673 nm, respectively).

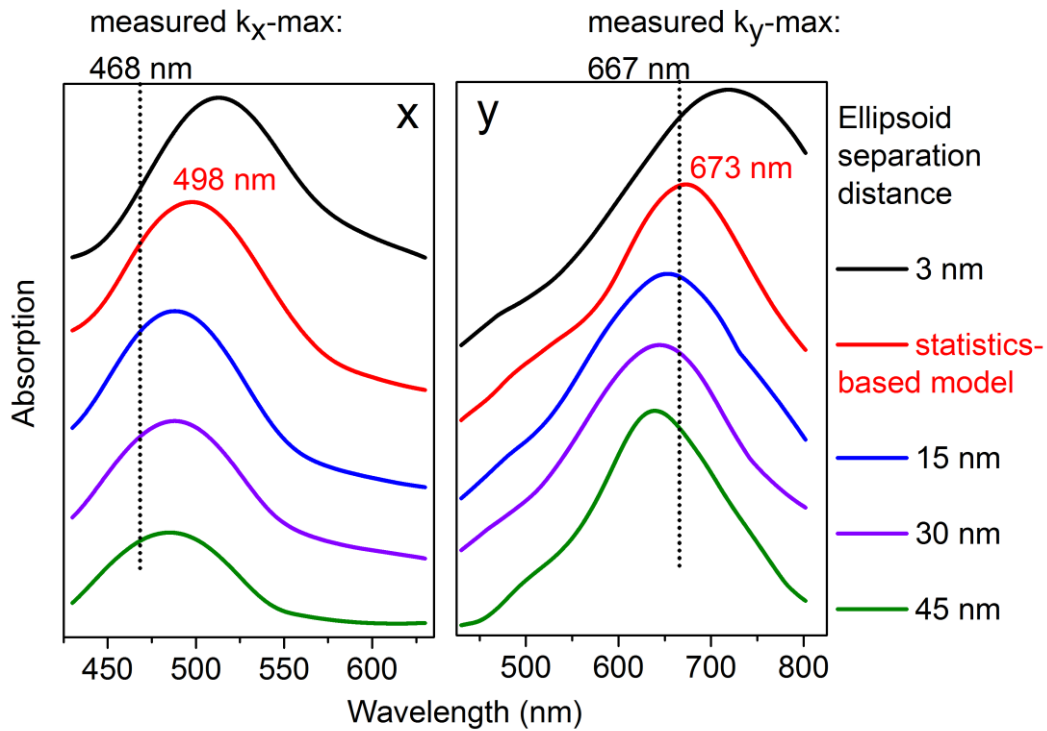


Figure 6.6: Far-field simulations (cascaded and normalized) of the absorption for x- (left) and y-polarized (right) normal incident field. The legend indicates the ellipsoid separation distance in the x- and y- direction. Measured maxima of k (taken from Fig. 4) are marked in the plots. Reprinted with permission from [150].

Conclusions

Optical data of anisotropic Ag nanoparticle arrays obtained by ellipsometry were studied and qualitatively interpreted by calculations of near- and far- field responses. The prepared silver nanoparticle arrays are described by a periodic model of Ag ellipsoids with two optical axes, the perpendicular (x) and parallel (y) to the ripples direction. From the comparison of experimental and simulated data some trends in the dependence of optical properties on the array structure can be concluded. Optical resonances in x and y directions can be attributed to localized plasmons with dipolar character, with the one in the parallel to ripples direction being stronger. The far- field calculations by RCWA compared to the ellipsometric data reveal that the resonances in the x direction are decoupled while the resonances in the y direction, at the dipole long axis, being in good agreement with the calculated data, contain presumably coupling effects. This work shows that the optical response measured by ellipsometry and interpreted by means of numerical modeling is sensitive to geometrical properties of the prepared nanoparticle arrays. A quantitative discussion requires a comprehensive theoretical and model optimization study and is an important issue for future work.

6.2 Raman scattering

The following part presents the case where the anisotropic resonances of silver nanoparticle arrays are used for surface enhanced Raman scattering. The enhancement factors exhibited are high and the resonances induce a polarization dependent SERS profile which extends up to NIR excitation wavelengths. The polarized dependent behavior and its applications are presented in detail.

Current status and limitations

Progress in analytical science relies upon highly specific detection of target molecules at very low quantities. Surface-enhanced Raman scattering (SERS) [63, 155] has become a well-established technique in this field as it improves the detection limit and is capable of probing very small amounts of molecules bound to plasmonic noble metal nanostructures [156]. SERS sensors exploit the large enhancements arising from the nanostructures. They come in a variety of structures including roughened electrodes, evaporated Ag nanorods, or colloid nanoparticles and they can even be embedded in microfluidic devices [157]. They are used to detect various analytes like bacteria, viruses, DNA, with glucose being a popular target molecule [158].

While SERS spectra of different molecules generally differ sufficiently to identify a certain target molecule, a considerable challenge remains for the quantitative analysis of specific molecular targets in the presence of related molecules. Here, the inherent specificity of a single SER experiment may not be sufficient and the analytical platform has to be expanded by combining different detection methods with complementary information on the same sample. Higher target specificity can be achieved, for example, when SERS analysis is performed using more than one laser excitation line. Using resonance Raman (RR) spectroscopy, this approach has been shown to be especially useful in the field of bioanalytics as multiple laser excitations can yield complementary information on different parts of the biomolecule displaying energetically separated electronic transitions [159-161]. To transfer the underlying principles to SERS spectroscopy requires the use of SERS-active support materials that exhibit plasmon resonances at different energies. Ideally, these energies should match electronic excitation energies of the adsorbate to selectively probe different chromophores by combining SERS and molecular RR effects (= SERR, i.e. surface enhanced resonance Raman).

Another analytical problem is to achieve selective detection of surface bound molecules only. This issue becomes especially important in organic solvents that exhibit intrinsically high Raman signals. Here even by using a confocal Raman setup, solution molecules may substantially interfere with the signals of the analyte. In this respect polarization-sensitive SER substrates have shown to significantly improve the discrimination between adsorbed and solubilized molecules [162].

An elegant solution to address these issues is based on anisotropic nanoparticles since here two different plasmonic resonance modes can be turned on and off by changing the exciting laser line and/or the polarization angle. A variety of fabrication techniques for generating

anisotropic nanoparticle platforms have been developed in the past [163, 164]. Top-down physical approaches such as arrays patterned by high resolution electron beam lithography provide precise control of the material nanostructure to dimensions of less than a nanometer [151, 165, 166]. However, the technique is time-demanding and expensive. Some of the earlier SERS substrates [167-170] were fabricated using evaporation of metals onto insulator surfaces resulting in self assembled nanoparticles. This technique represents a compromise between expense and simplicity, while providing reasonable control over the metallic nanostructure and good SERS enhancement [91, 164, 171-173].

Anisotropic nanostructures formed by metal evaporation can be further controlled by deposition onto substrate templates [98, 100, 174]. Rippled template surfaces generated by oblique-incidence low-energy ion beam sputtering are promising candidates, offering the potential to fabricate arrays of nanowires and nanorods [100, 175]. These arrays show strong optical anisotropy arising from the differences in the localized plasmon resonances of the particles in orthogonal directions in coupling between the particle plasmon resonances in orthogonal directions [38, 176, 177]. These resonances are the type leveraged to enhance Raman scattering cross-sections.

A number of groups have employed anisotropic materials as polarization-sensitive SERS substrates [106, 178-181], however, only a few of them applied multiple excitation wavelengths. For gold nanowire arrays, a $\cos^2\theta$ -dependence of the Raman scattering intensity was demonstrated, with the angle θ defined by the polarization vector of the exciting laser and the axis perpendicular to the wires [179, 182]. This relationship directly follows the absorption of the light in the film as determined by far-field measurements. Fazio et al. performed an analysis based on the Raman tensor of the molecule in the exciting field [179]. In a similar study, D'Andrea et al. compared the enhancement of the SER signal at two different excitation wavelengths [178], but with the absorbance at one direction constantly larger than in the orthogonal direction. The observed properties of the polarization studies on anisotropic materials have their basis on the behavior of dimers and trimers. Etchegoin et al. [74] have studied the polarized SERS properties of metal nanoparticle dimers and trimers. They demonstrated that the $\cos^2\theta$ -dependence is based on the direction of the dimer axis and is not related to the Raman tensor of the molecules. These theoretical approaches have been verified by numerous experiments on dimers that show the $\cos^2\theta$ relation, while in a trimer the polarized properties are more complex due to the coupling between the three particles [180, 183, 184].

Although the dependence of the SERS enhancement on the plasmon resonance frequency has been well documented, it has not been conclusively investigated in a polarized SERS experiment. In the studies on rippled substrates with two excitation wavelengths, so far mainly nanowires were employed.

In this work is demonstrated the simultaneous polarization- and wavelength-dependence of the SERS signal of the molecular adsorbate on the plasmon resonances of Ag nanoparticle arrays on rippled substrates. A $\cos^2\theta$ and $\sin^2\theta$ signal dependence is observed respectively, according to the wavelength of the exciting laser and the polarization. The dielectric function of the film is determined using spectroscopic ellipsometry showing unambiguously

that the SERS enhancement correlates with the direction of the Ag nanorods. Optimization of these properties aims for at increasing specificity in detection of target molecules.

Experimental details

The periodicity of the rippled substrate was 40 nm. The evaporation was at an oblique angle of 70 degrees with respect to the surface normal. The surface morphology was characterized by scanning electron microscopy. Image analysis was performed with ImageJ. The optical properties were measured with a SENTECH SE850 ellipsometer. The ellipsometry data are modelled to extract the effective dielectric function of the Ag film, using a procedure similar to that outlined in chapter 6.1 [38].

For the Raman measurements the 514 nm laser line of an Argon laser (Coherent Innova 300c Ar) and the 647 nm line of Krypton Laser (Sabre Innova Kr) were used. The laser power on the sample was 1.0 mW. The laser beam was focused onto the sample by a Nikon 20× objective with a numerical aperture of 0.35 and a spot size of approximately 2 μm in radius. All SERS spectra were normalized per mW laser power and per second of accumulation time. In all experiments, analyzer and polarizer were set in parallel polarization position. The effects of polarizer and analyzer configurations are shown in 'Parallel and cross-polarized configuration' part, below.

The Raman setup is equipped with a polarizer at the laser output. The beam is incident on the sample with a specified polarization direction, while the sample is mounted on a rotating stage. The scattered light is collected through the objective lens and guided to the detector. The light passes through an analyzer, positioned in a parallel polarization configuration Figure 6.7 depicts the setup and the direction of the laser polarization in relation to the sample geometry. θ is denoted as the angle between the polarization of the laser beam and the axis perpendicular to the ripples.

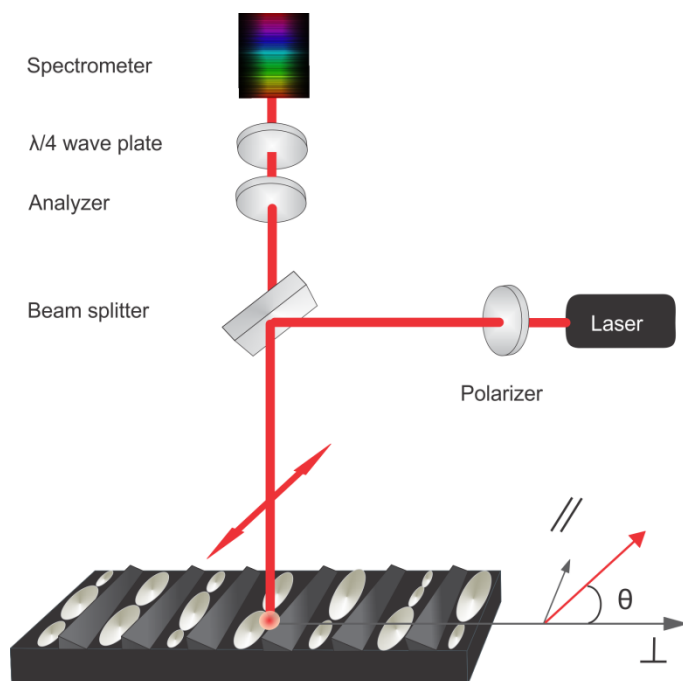


Figure 6.7: The Raman setup for polarized measurements. θ is defined as the angle between the laser polarization direction and the axis perpendicular to the ripples (\perp). Reprinted with permission from [146].

Results and discussion

The Ag islands grow preferentially along the ripples as demonstrated by scanning electron microscopy (SEM) in Figure 6.8. The resultant anisotropic distribution of nanoparticles and nanorods covers around 50% of the surface area. The dimensions vary between 150 nm to 20 nm for the long axis, with average length at 45 nm, and between 40nm (in the case of the longer particles) down to 20 nm for the short axis, with an average length of 26 nm. These results show aspect ratios ranging from 6:1 to 1:1 with an average ratio of 1.7.

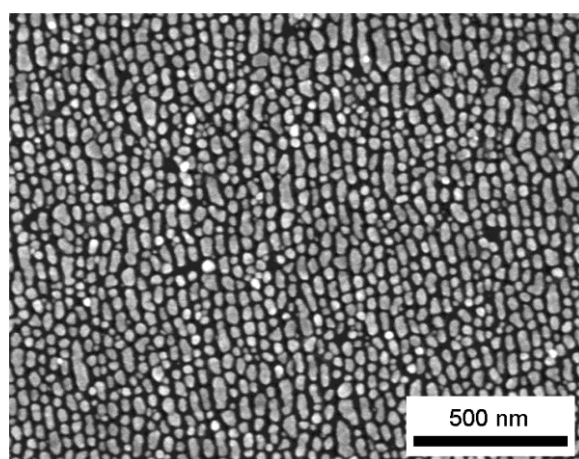


Figure 6.8: SEM image showing silver nanoparticles aligned along nanoripples on silicon. The long axis of the islands is aligned along the ripples. Reprinted with permission from [146].

Figure 6.9 shows the imaginary part ϵ_2^{eff} of the effective dielectric function parallel (\parallel) and perpendicular (\perp) to the long axis of the ripples. The ellipsometry data were analyzed using a three layer model outlined in methods part in 6.1. In the quantity ϵ_2^{eff} , plasmon peaks can be observed corresponding to the effective direction-dependent absorption of the Ag nanoparticle film. In the perpendicular direction, the plasmon resonance peak is centered at 514 nm. Parallel to the ripples, the plasmon resonance is substantially red-shifted to ca. 745 nm. The insets are corresponding to the (normalized) near-field calculations showing the two localized dipolar plasmon resonances.

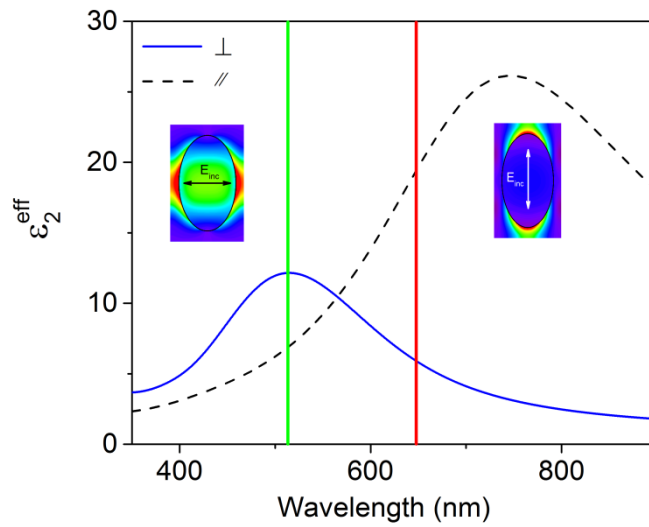


Figure 6.9: Optical resonances for the directions \perp (blue), with dipole excitation on the short axis, and \parallel (dashed black), with dipole excitation on the long axis. The vertical lines indicate the positions of the 514 nm and 647 nm excitation wavelengths used in the SER experiments. Reprinted with permission from [146].

Parallel and cross-polarized configuration

The analyzer was inserted in parallel polarization position in order to refine the scattered light and emphasize on the directional enhancement properties.

In theory [74], the signal in a backscattering configuration is proportional to $\cos^4\theta$ for a parallel polarized setup and $\cos^2\theta \times \sin^2\theta$ for the cross-polarized setup for which there are no observations experimentally except in Fazio et al [179].

Figure 6.10 shows the absolute height of the 1079 cm^{-1} peak for the parallel and cross polarized configuration at 514 nm excitation. The behavior of the parallel polarized peak was decided to be described as $\cos^2\theta$ and not as $\cos^4\theta$, as expected theoretically. The plot of those functions is similar and it would need a larger number of experimental angular positions to effectively distinguish between those trends.

Figure 6.11, left, shows the behavior on a similar sample, of the peak 1587 cm^{-1} , at excitation 514 nm , without the use of an analyzer for a 45° measuring step. While Figure 6.11, right, shows the same peak for a parallel polarized configuration, the counts on the left figure are increased by a factor of two compared to the right graph, since all the scattered light is collected. The behavior in both cases follows a $\cos^2\theta$ function.

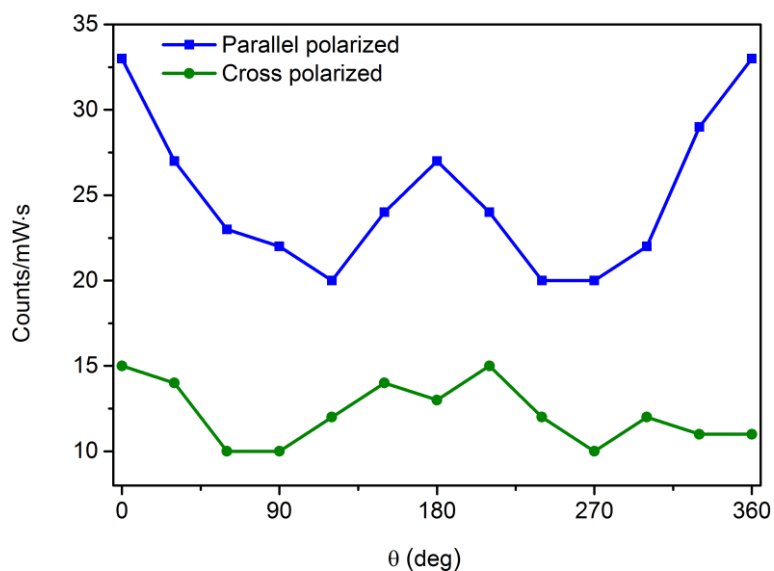


Figure 6.10: Normalized intensity of the 1079 cm^{-1} band of 4-MBN as function of θ obtained with 514 nm excitation. Top data (blue squares) stand for parallel polarized configuration and bottom data (green circles) stand for the cross polarized configuration.

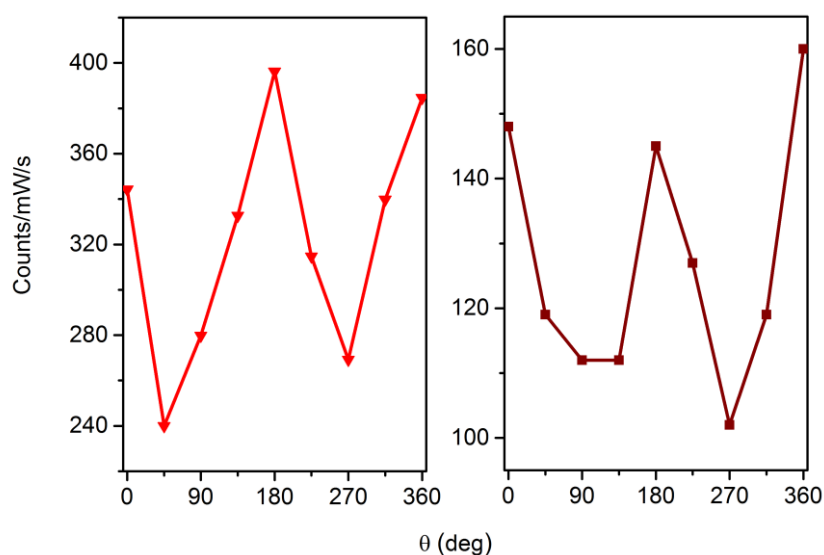


Figure 6.11: Normalized intensity of the 1587 cm^{-1} band of 4-MBN as function of θ obtained with 514 nm excitation without the use of analyzer (left), and analyzer set in parallel polarized position (right).

Multiple excitation wavelengths

Accordingly, for investigating the range of anisotropic properties in SERS spectroscopy, the excitation lines at 514 nm and 647 nm, close to the maxima of the two plasmon resonances, were employed. Additionally, a 758 nm excitation was employed. As a probe molecule 4-mercaptobenzonitrile (4-MBN) was chosen as it forms compact self-assembled monolayers on Ag and thus ensures a complete and defined coverage of the metal surface (Figure 6.12, left). Furthermore, electronic transitions of 4-MBN are at much higher energies than the plasmon resonances, such that any interference of molecular resonance enhancement with the SER effect is avoided.

Figure 6.12 shows the SERS spectra of 4-MBN obtained at 647 nm excitation with polarization direction along the islands long axis, i.e. parallel to the ripple direction. The most prominent bands are observed at 1079, 1182, and 1587 cm^{-1} and originate from modes of the substituted benzene ring, while the peak at 2238 cm^{-1} is due to the $\text{C}\equiv\text{N}$ stretching mode.

The average Raman enhancement factor (REF) was calculated for both laser wavelengths for the intensity of the peak at 1587 cm^{-1} (Details in 3.7). For 514 nm excitation a value of $\text{REF} = 1.5 \cdot 10^3$ is obtained, whereas for the 647 nm line an enhancement of $2 \cdot 10^4$ was determined. These enhancement factors were compared with the ones obtained using an electrochemically roughened electrode as SERS support. Here REF values of $7 \cdot 10^2$ and $2 \cdot 10^3$ were measured for 514 nm and 647 nm excitation respectively. It is thus concluded that the optical enhancement at 514 nm of the anisotropic rippled substrate is comparable to the electrode, but for the 647 nm excitation the rippled substrate performs better from the electrode by an order of magnitude.

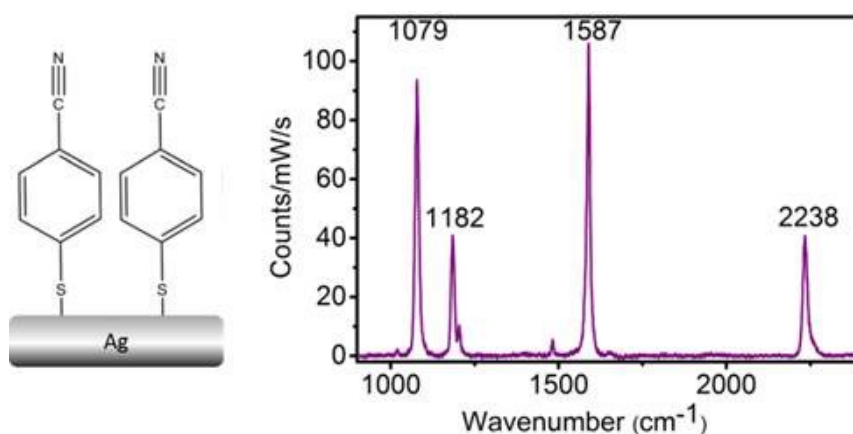


Figure 6.12: SERS spectra of 4-MBN obtained with 647 nm excitation on anisotropic sample with polarization direction along the islands long axis.

Reprinted with permission from [146].

Subsequently, SERS spectra at the two laser energies were measured as a function of θ , which is defined as the angle between the laser polarization direction and the axis perpendicular to the ripples (\perp). These SERS spectra were obtained upon sample rotation in

steps of 30°. The intensity scale of each spectrum was normalized to the same laser power and accumulation time and the resultant normalized intensities of the 1079 cm⁻¹ band were plotted as a function of θ (Figure 6.13).

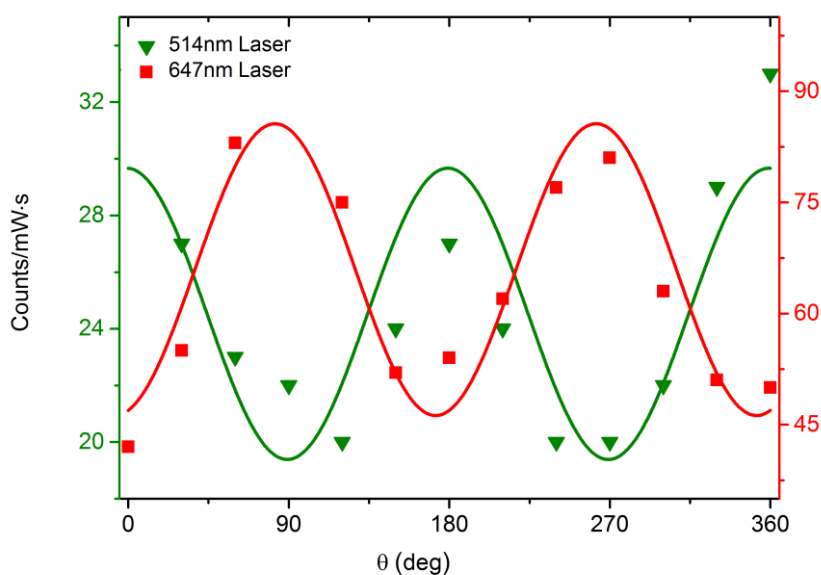


Figure 6.13: Normalized intensity of the 1079 cm⁻¹ band of 4-MBN as function of θ obtained with 514 nm (green triangles) and the 647 nm (red squares) excitation. The respective solid lines correspond to fits of a $\cos^2(\theta)$ (green) and $\sin^2(\theta)$ (red) function to the data. Reprinted with permission from [146].

Excitation at 514 nm is close to the surface plasmon resonance in the direction perpendicular to the ripples (\perp) (Figure 6.9). Thus, optimum enhancement is expected at $\theta = 0^\circ, 180^\circ,$ and 360° , which is in fact observed (Figure 6.13). Conversely, absorption parallel (\parallel) to the ripples is significantly weaker, corresponding to weaker SERS intensities at $\theta = 90^\circ$ and 270° . Likewise, at 647 nm excitation, the plasmon resonance is significantly stronger in the direction parallel to the ripples (\parallel) (Figure 6.9). Thus, under these conditions maximum SERS intensities are observed at $\theta = 90^\circ$ and 270° whereas minima are noted for $\theta = 0^\circ, 180^\circ$ and 360° . Consequently, the intensity data at 514 nm and 647 nm excitation (Figure 6.13) can be well described by a $\cos^2\theta$ and $\sin^2\theta$ function, respectively. The adjusted R-square values were determined to be 0.67 and 0.91 for 514 and 647 nm excitation, respectively, and the phase difference between the two curves is $97^\circ \pm 9$. Within the experimental error this value agrees very well with the expected phase shift of 90° for island films with ideally perpendicular oriented plasmon resonances. However, a small deviation from the theoretical value could also arise from the non-perfect sample geometry [38].

In order to confirm that this behavior is consistent throughout the spectral range and that it can be indeed leveraged for multiple laser excitation experiments, the procedure was reproduced at a sample with the parallel to the ripples resonance (\parallel) being in the NIR (Figure 6.14). Figure 6.15 shows an identical behavior to Figure 6.13, where during

polarization rotation the signal of the 514 nm excitation follows a $\cos^2\theta$ function, matching the perpendicular to ripples resonance. Respectively the signal of the 785 nm excitation follows a $\sin^2\theta$, maximizing when the polarization is parallel to the ripples direction, exciting the longitudinal resonance.

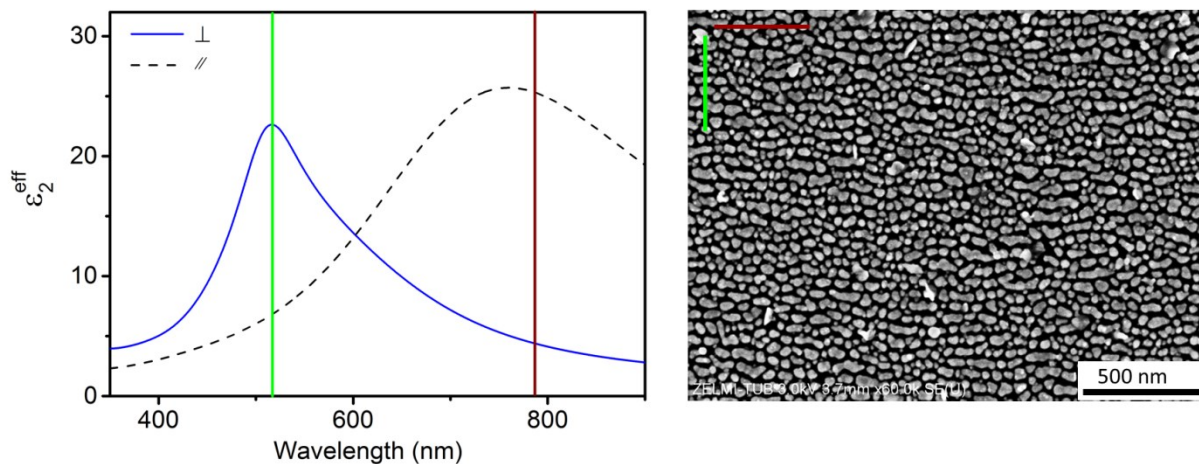


Figure 6.14: Left, optical resonances for the directions \perp (blue), with dipole excitation on the short axis, and \parallel (dashed black), with dipole excitation on the long axis. The vertical lines indicate the position of the 514 nm and 785 nm excitation wavelength used in the SER experiments. Right, SEM image of the corresponding geometry.

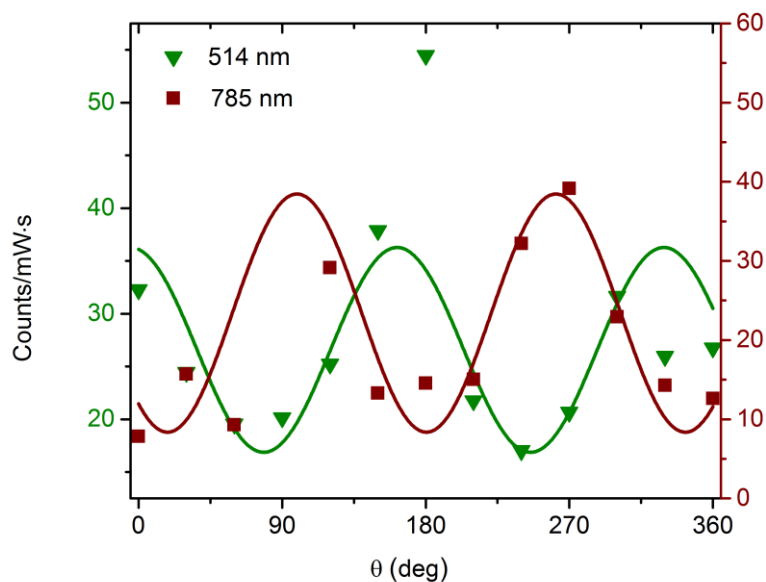


Figure 6.15: Normalized intensity of the 1079 cm^{-1} band of 4-MBN as function of θ obtained with 514 nm (green triangles) and the 785 nm (brown squares) excitation. The respective solid lines correspond to fits of a $\cos^2(\theta)$ (green) and $\sin^2(\theta)$ (brown) function to the data.

The observed $\cos^2\theta$ -dependence of the SERS intensity is in line with the expected and experimental behavior of dimers [74, 180] and with previous results for rippled substrates and nanowire-array systems [179, 181, 185] although in these studies only a single excitation wavelength was employed. D'Andrea et al. [178] has used polarized SERS enhancement at multiple excitation wavelengths before, but did not observe a reverse of the SERS signal for parallel and perpendicular directions, due to the resonance perpendicular to the nanowires being constantly larger.

Application

The polarization-dependence of the enhancement can be exploited for analytical applications when the substrate is in contact with a solution phase, since it facilitates the discrimination of Raman scattering from the solution compared to the SER signals from the adsorbed species. This is particularly true if the solvent exhibits an intense Raman spectrum such as many organic solvents.

An instructive example is given for 4-MBN adsorbed on rippled silicon with deposited Ag substrates in contact with cyclohexane excited by 514 nm wavelength (Figure 6.17, left). As a reference measurement the beam was focused on the surface of clean silicon placed in a cyclohexane solution. The spectrum (Figure 6.16, above) shows a prominent peak at 800 cm^{-1} being assigned to the C-C stretching mode of cyclohexane. Figure 6.16, bottom shows the spectrum of 4-MBN adsorbed on Ag, placed in cyclohexane. There is a substantial enhancement of the cyclohexane peaks by a factor of ~ 7 .

Figure 6.17, right, shows the intensities as a function of θ of the 4-MBN peak 1587 cm^{-1} and the cyclohexane 800 cm^{-1} peak. The intensity of the solvent band remains largely independent of θ , while the 4-MBN signal displays essentially the same polarization dependence as found for the Ag/4-MBN/air interface (Figure 6.13). Thus, variation of the polarization angle allows for distinguishing between adsorbed and bulk species.

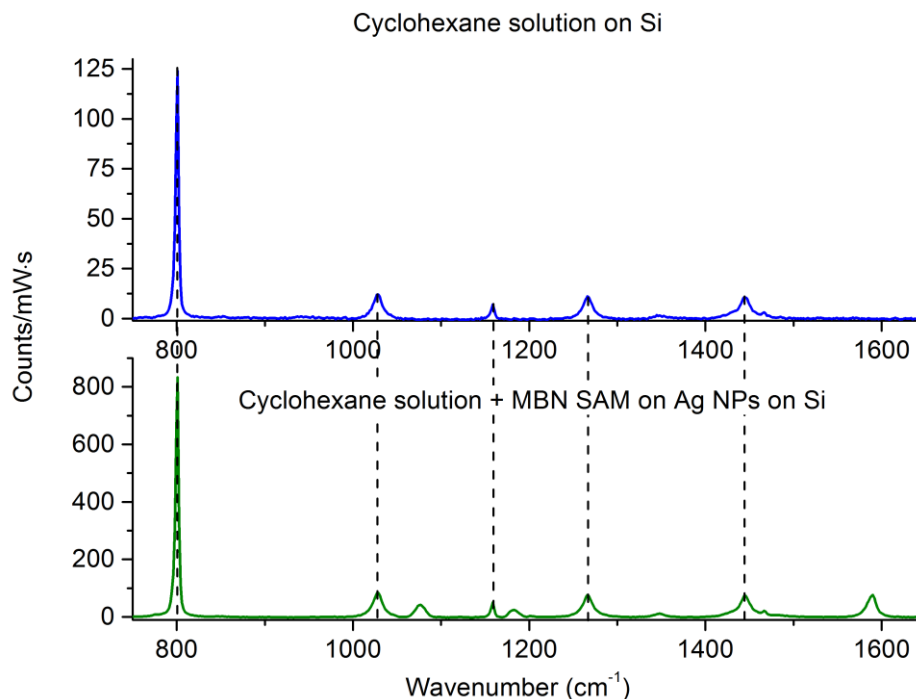


Figure 6.16: Top: Cyclohexane solution signal on Silicon surface for 514 nm excitation. Bottom: Cyclohexane solution and adsorbed 4-MBN signal of anisotropic Ag nanoparticles on rippled silicon surface for 514 nm excitation.

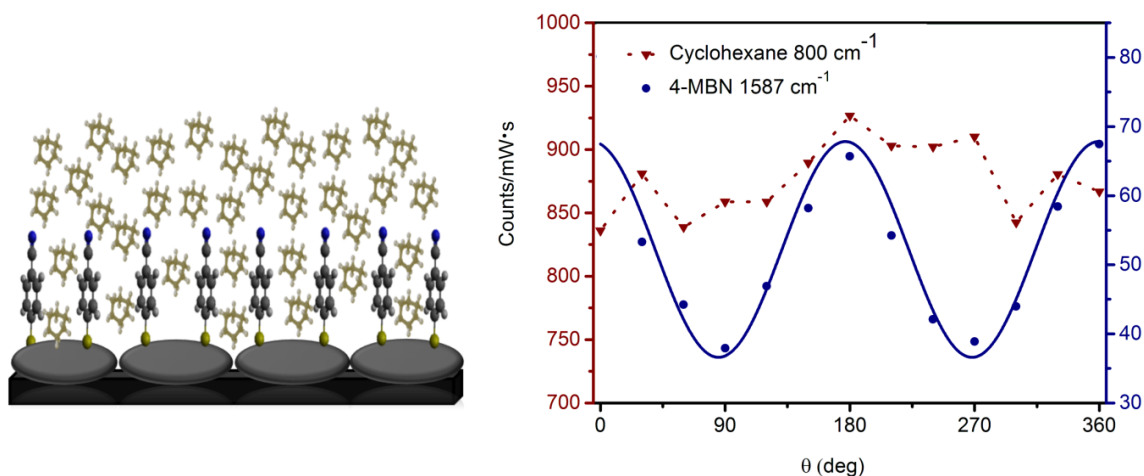


Figure 6.17: Left, Schematics of the Ag nanoparticles substrate with the adsorbed 4-MBN placed in the cyclohexane solution. Right, normalized intensities of the 1587 cm^{-1} SER band of adsorbed 4-MBN and the 800 cm^{-1} Raman band of cyclohexane as a function of θ , obtained with 514 nm excitation.

Conclusions

In conclusion, it is shown that SERS enhancement in optical anisotropic substrates can be controlled by varying substrate orientation (excitation beam polarization) and Raman excitation wavelengths. Upon rotation of the sample, optimum enhancement conditions can be established for resonant excitation of the parallel and perpendicular plasmon modes of the support material. Polarization and wavelength dependencies for the anisotropic substrates provide signal enhancement in a wide spectral range on a single substrate. This may open novel possibilities in (bio)chemical analytics and sensing, since the use of multiple laser excitation with polarization modulation is likely to increase the specificity of target detection. Whereas in this fundamental study, the interference with the molecular resonance enhancement of the adsorbate was intentionally avoided, the combination of molecular electronic resonance and plasmon enhancement ($RR + SER = SERR$) will substantially increase the Raman intensity of the adsorbate. This effect is of particular interest for the analytics of molecular mixtures of compounds that exhibit electronic transitions close to one of the plasmon resonances. Multiple laser excitation under optimum polarization conditions would then enhance the contrast compared to the optically transparent molecules. In addition, the well-defined polarization dependence of the SER intensity allows enhancement of the contrast between the signals from the adsorbed target molecules and those of the solution species. This feature is of potential interest for sensing in the environmental and medical field.

6.3 Infrared absorption

The following part demonstrates the polarization dependent surface enhanced infrared absorption properties of silver nano-islands and anisotropic silver nanoparticle arrays. The progression of the resonances from the visible to the IR range and their effect on the enhancement was measured with FTIR (polarized) microscopy along with IR ellipsometry, to affirm the polarization dependence of the substrate and its ability to be utilized for dual SERS and SEIRA measurements.

Background

SEIRA absorption has received less attention due to lower enhancement factors, that average around 10-100 [186]. Nevertheless, SEIRA does not face fluorescence issues. Also, when comparing an equally active IR and Raman mode, the corresponding cross-section of IR absorption is higher than Raman scattering, counterbalancing in certain cases the much higher SERS enhancement factors [81]. The enhancement resulting from the metallic support allows the ultra-fast detection of signals, enabling the real-time study of biological interaction mechanisms in in-situ experiments, detection of the molecule adsorption on the surface and its conformation [187, 188]. The contribution of SEIRA in electrochemistry has been crucial, e.g. the combination of SEIRA with cyclic voltammetry has helped in the study of redox states, molecular structure and reaction mechanisms of immobilized proteins [80, 189].

Pioneers of the field, the Osawa group worked mainly with evaporated metal islands observing maximum enhancement close to the percolation threshold [190]. Often used are various combinations of SEIRA with Attenuated Total Reflection (ATR) prisms [81], while another common SEIRA substrate is that of an electrochemically roughened electrode [20]. While an electrode is based on the large surface area as a binding site, there are also substrates with defined structures, i.e. nanoantennas, that claim high enhancement factors in hot-spots between the nanogaps of the antenna tips [12, 191]. These structures are fabricated with electron beam lithography and their tunable length is defining the range of the resonant peak in the IR region. Recently it has been shown that the nanoantenna resonant tuning can be scaled up for use in THz, presenting one order of magnitude enhancement [192]. In certain cases the use of Fano resonances is employed for the further increase of the enhancement, leading to lower than attomolar sensitivity [193].

The present chapter presents the application of SEIRA for 4-MBN adsorbed on evaporated silver islands as well as arranged Ag NP arrays. The main technique used for studying the SEIRA effect was FTIR reflection spectroscopy. Additionally, IR ellipsometry and polarization dependent IR microscopy have been used. Due to the increasing complexity of plasmonic structures [194], metamaterials [195] and solid-liquid interfaces [196], these techniques will prove increasingly useful in the future due to their sensitivity in measuring optical properties of thin layers with polarization dependency and increased lateral resolution. Polarized FTIR microscopy offers lateral resolution down to the diffraction limit. However, the low angle of incidence reduces the sensitivity especially for the study of thin films. The detection limit in some cases can be increased by the use of grazing angle of incidence or ATR techniques. Hinrichs et al. adapted a commercial polarized FTIR microscopy setup into measuring the ellipsometric values Ψ and Δ , opening a path for a

versatile setup that can perform both FTIR and ellipsometric measurements [102]. IR ellipsometry can improve the typically low sensitivity of IR, allowing the determination of nanometer scale thickness of molecular layers additionally to their molecular fingerprint [197]. Polarized FTIR spectroscopy and IR ellipsometry can provide information about the in-plane and out-of-plane optical properties of a structure, resonance response in various directions, determine tilt angles of organic layers as well as their thickness even in in-situ conditions [198].

The combination of surface enhancement with advancements in measuring techniques and sample handling, e.g. microfluidic cells [187, 199], is due to increase the interest in and impact of SEIRA for in-situ and ex-situ studies of biochemical interactions.

SEIRA on Ag nano-islands

The main method used for investigation of the surface enhancement in the IR region was by obtaining FTIR spectra in reflectance mode. Figure 6.18 shows the morphology and the imaginary part of the pseudodielectric function of Ag nano-islands, which exhibit SEIRA according to the FTIR spectrum presented in Figure 6.19.

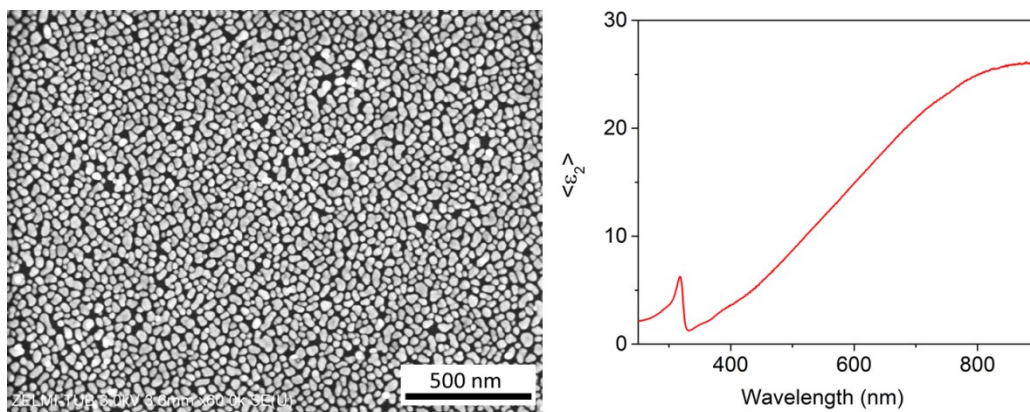


Figure 6.18: Morphology and imaginary part of pseudodielectric function of Ag nano-islands.

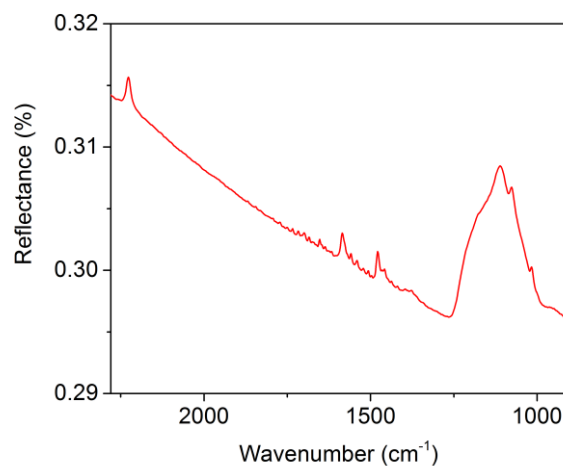


Figure 6.19: Corresponding SEIRA reflectance spectrum of 4-MBN adsorbed on Ag nano-islands.

Nanoparticles with average diameter of 50 nm and thickness of 30 nm induce a resonance peaking in the NIR range, at around 800 nm wavelength. The tail of the resonance extends to the mid-infrared, enhancing the vibrational signal of the molecule adsorbed on the metal surface. Specifically, the stretching of the nitrile group is identified at 2226 cm^{-1} , the benzene ring stretching at 1585 cm^{-1} , ring stretching combined with deformation at 1478 cm^{-1} and ring breathing at 1017 cm^{-1} (Figure 6.19)[199]. The peak around 1075 cm^{-1} is identified as a phonon of SiO_2 [200].

The control of the evaporation process can lead to smaller isolated nanoparticles or bigger, interconnected nano-islands, which exhibit red-shifted resonances and enhance further in the IR. Osawa claims that the greatest enhancement is achieved when the islands are densely packed but not touching [87]. Therefore, SEIRA efficiency can be tuned according to the sample preparation method.

IR Ellipsometry

Silver was deposited by evaporation under oblique angle on rippled silicon templates. The Ag nanoparticles grow preferentially along the ripples, introducing optical anisotropy in two orthogonal directions, perpendicular (\perp) and parallel (\parallel) to the ripple direction. SEM pictures in Figure 6.20 (a, b, c) show the morphology of the surface for increasing Ag deposition. The scale bar stands for 500 nm and the red bar declares the direction parallel to the ripples. It is observed that the Ag nanorods increase their length and width (Figure 6.20, a), maintaining the parallel to the ripples axis preferred direction (Figure 6.20, b). At increased thickness they grow even above the ripples and aggregate with neighboring nanoislands (Figure 6.20, c). The nominal thicknesses for samples a, b and c are 10 nm, 24 nm and 30 nm respectively. Figure 6.20 (d, e, f) show the imaginary part of the pseudodielectric function, $\langle \epsilon_2 \rangle$, of the corresponding samples measured by UV-Vis ellipsometry. Both of the resonances are initially in the visible region, while they red-shift at increased Ag thickness, ending up being both in the IR region. The resonance parallel to ripples red-shifts more drastically with increasing deposition compared to the one in the perpendicular direction. Figure 6.20 (g, h, i) show the $\tan\Psi$ for the respective samples, obtained by IR ellipsometry. The lines have been vertically translated slightly in order to facilitate comparison. The measured region corresponds to the range of 1500 nm to $10\text{ }\mu\text{m}$ and provides a quantitative view of the resonance advance in the IR. Note that the y axes values of (d,e,f) and (g,h,i) groups, Figure 6.20, are in $\langle \epsilon_2 \rangle$ and $\tan\Psi$, respectively, as $\langle \epsilon_2 \rangle$ offers a clearer overview of the resonances in the visible range. The graphs reveal a consistent extension of the resonances for the two optical orthogonal axes, parallel and perpendicular to the ripples, from the visible to the IR region. Those resonances are the origin of the molecular vibration enhancement in the fingerprint region, as it is shown in more detail in Figure 6.21.

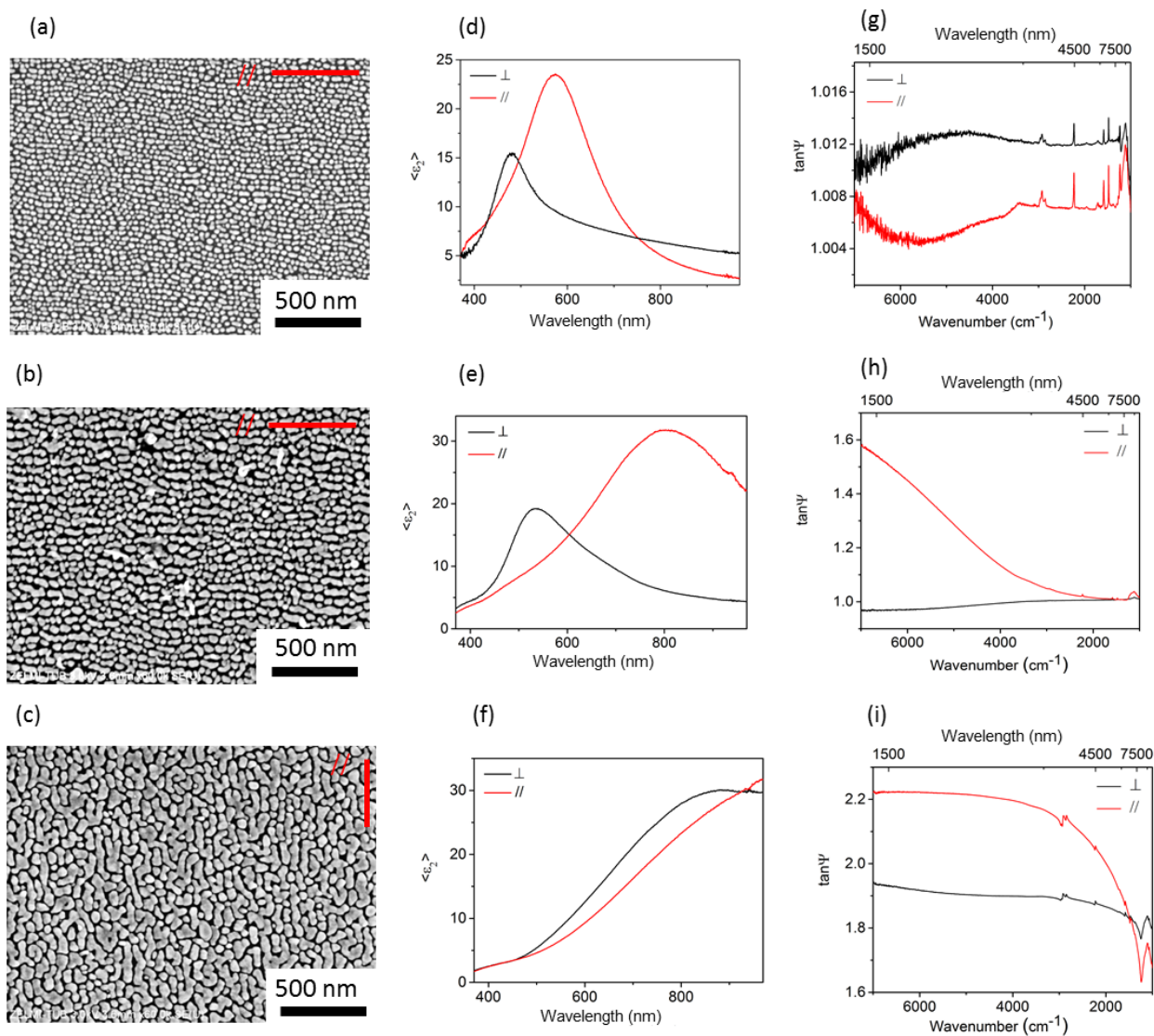


Figure 6.20: (a,b,c) SEM pictures of Ag NPs growing along the ripple axis (red bar) for increasing Ag deposition. (d,e,f) Pseudodielectric functions of the two optical axes (\perp & \parallel) for the samples corresponding to the SEM pictures. (g,h,i) $\tan\Psi$ at the IR region of the corresponding samples.

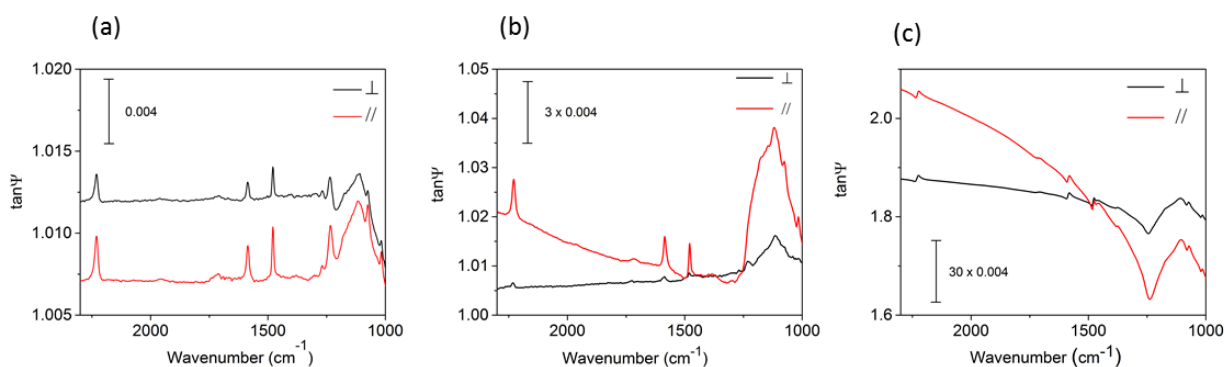


Figure 6.21: (a,b,c) $\tan\Psi$ of the two optical axes (\perp & \parallel) at the 4-MBN "fingerprint" region for the samples corresponding to the ones shown in Figure 6.20.

Figure 6.21 focuses on the spectral region of the molecular vibration, in order to demonstrate the effect of the plasmonic resonances on the enhancement of the signal. Figure 6.21 (a) appears flat and with low intensity compared to samples (b) and (c) where the resonance introduces a tilt in the curve and increase of the peak signal.

| Sample | EF \perp direction | EF \parallel direction |
|--------|----------------------|--------------------------|
| a | 20 | 34 |
| b | 13 | 100 |
| c | 156 | 170 |

Table 2: Enhancement factors estimated for the 2226 cm^{-1} 4-MBN peak in IR.

Table 2 presents the calculated enhancement factors of the 2226 cm^{-1} 4-MBN peak ($\text{C}\equiv\text{N}$ stretching). The calculation method is described in 3.7. The enhancement of the 4-MBN peaks follows the trend of the advancing resonances in the IR region. In the case of sample (a), even without a visible plasmonic resonance, the peak is by 20 to 34 times enhanced compared to peaks of 4-MBN monolayer on silicon. This enhancement can be a result of a very small resonance tail extending to the mid-IR. The increased absorption coefficient of the metal adds up to the weaker molecular absorption leading to signal enhancement [90, 188].

Part of the enhancement may also be a result of the orientation angle of the SAM on the Ag surface. The values of the 4-MBN vibrations for the EF calculations were extracted from the SAM adsorbed on a gold surface. The tilt angle of thiophenol SAM on gold surface with respect to the surface normal is 49° , while the tilt of thiophenol on silver is estimated at 24° by Frey et al. [132]. The increased vertical tilt of 4-MBN on silver provides improved coupling of the dipole moment of the nitrile function with the electric field at the surface normal and increases the enhancement due to the surface selection rules [101, 128, 132].

Sample (b) brings forth the effect of the substrates' anisotropy. As it is seen in Figure 6.21, b for the direction parallel to the ripples (red line), the 4-MBN peaks are placed on the edge of

the resonance and therefore being enhanced. On the contrary, perpendicular to the ripples (black line) there is only limited enhancement. This sample is an example of tuning for combined SERS and SEIRA activity. It presents a 100-fold enhancement of the IR absorption signal while the orthogonal direction bears a resonance in the visible range that is enhancing the Raman scattered signal. Additionally, the direction parallel to ripples, with the red-shifted resonance, can provide SERS at NIR excitation. The SERS signal for excitation wavelengths is shown in Figure 6.15.

Sample (c) though, has both of the resonances in the IR region leading to a great enhancement of the 4-MBN peaks for both excitation directions. The CN peak is enhanced by a factor of 170 compared to the peak without the existence of the Ag layer. The resonances introduce a distortion of the molecular bands. This asymmetry in the detected vibrational band, frequently named Fano-type profile, appears in the onset of percolation of metal island films [201]. The underlying mechanism includes a plasmonic resonance in the IR that introduces a broad continuum-like resonance interfering with a narrow discrete resonance, such as a molecular vibration [202]. Significant efforts have been performed in tuning the length of plasmonic gold nanoantennas in order to tune the Fano intensity, achieving lower than attomolar detection [193]. The connection of morphology with the band shape and the enhancement is further discussed in Chapter 7.

Polarized FTIR microscopy

While IR ellipsometry provides information on how the sample surface changes the polarization of light, the measuring spot is a few mm². In the case that increased spatial resolution is needed FTIR microscopy can be employed. For maintaining the ability to collect polarization information the IR microscope was modified as described in the experimental setup section, 3.5. As a counter-effect though, the increased spatial resolution in combination with the slit (OPA) and polarizer leads to decreased photon flux, raising the measuring time to 40.000 scans. The spot size is about 160µm. The lateral resolution potentially can go down to 40 µm of spot size with sufficient signal-to-noise ratio [102].

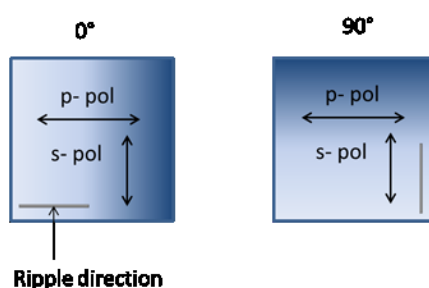


Figure 6.22: Polarization direction for sample rotation by 0° and 90° to the ripple direction.

Measurements were performed for two samples, an unrippled and a rippled silicon substrate with a gradient of thickness (details on the deposition of a gradient substrate are given in Chapter 7). The measured area has an average thickness of ~30 nm. One set of

measurements was the measurement of p- and s- polarization for the sample at 0° in reference to the ripple direction. The second was the measurement of p- and s- for the sample rotated by 90° to the ripple direction (Figure 6.22). Therefore the 0° -p and 90° -s orientations excite the direction along the ripples, while the 0° -s and 90° -p excite across the ripples.

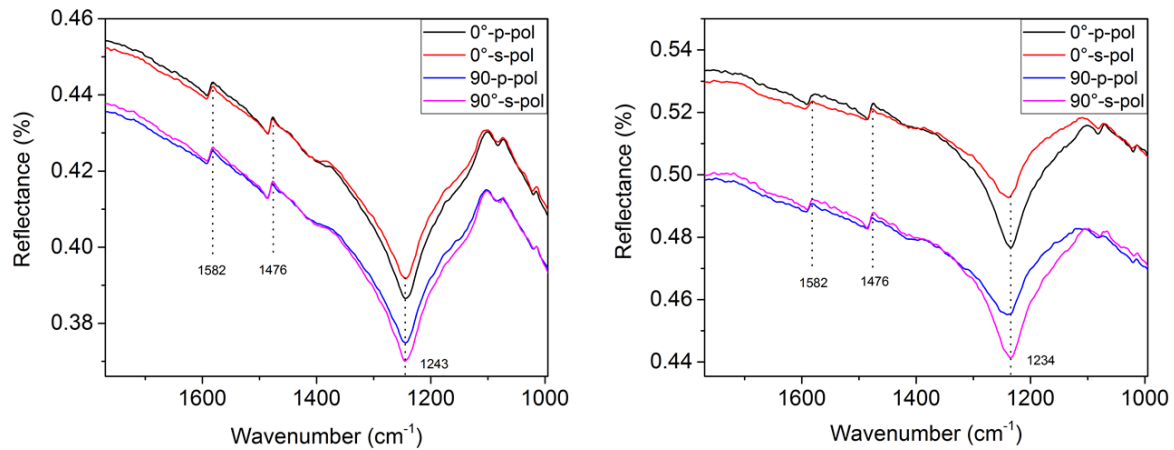


Figure 6.23: Polarized IR spectra for sample positions 0° and 90° of unrippled (left) and rippled (right) substrate.

Figure 6.23 shows the polarized IR spectra for the unrippled (left) and the rippled (right) samples. At the unrippled sample (Figure 6.23, left) the 4-MBN peaks, 1582cm^{-1} 1476cm^{-1} , have non-noticeable signal differences at the two polarizations. On the opposite, the band at 1243cm^{-1} (left figure) and 1234cm^{-1} (right figure) exhibits different signal intensity due to polarization direction. This band is associated with the layer of SiO_2 under the metal overlayer and is assumed to have the same origin as the Berreman mode [203, 204].

In the case of the rippled sample, as it is visible from Figure 6.23 (right), the 4-MBN peaks do not have the same height. This is a result of the anisotropy of the sample between the x and y axis. When the sample is at 0° position the p direction excites along the ripples where the nanorods are extending while the s polarization direction excites across the ripples and the signal difference is seemingly connected to the amount of deposited silver in the two directions. As it has been discussed in part 6.1, the direction parallel to the ripples bears a stronger, red-shifted resonance and therefore a stronger enhancement. Table 3 presents the calculated ratios of the peak heights for the two samples and the polarization sets in reference to the ripple direction. The ratio of the signal difference of 4-MBN peaks between the two polarization directions at the rippled sample amounts to 1.6. Of particular interest is the area associated with the SiO_2 band, having the same intensity ratio to the adjacent 4-MBN peak band. The connection of the molecular band intensity with the SiO_2 related band has been noted by Kratz et al. [199] and found to be dependent on the metal overlayer. The present results support these findings, that also introduce the possibility of using the SiO_2 related area as an internal calibration peak.

| Sample | peak | 1590 cm ⁻¹ | 1486 cm ⁻¹ | SiO ₂ (1250cm ⁻¹) | Error |
|-----------|---------|-----------------------|-----------------------|--|-------|
| Unrippled | 0° p/s | 1 | 1.2 | 1.1 | ±0.1 |
| | 90° s/p | 1.1 | 1.2 | 1.1 | ±0.1 |
| Rippled | 0° p/s | 1.4 | 1.5 | 1.6 | ±0.1 |
| | 90° s/p | 1.3 | 1.6 | 1.5 | ±0.1 |

Table 3: Ratio of the peak heights for the two polarization directions.

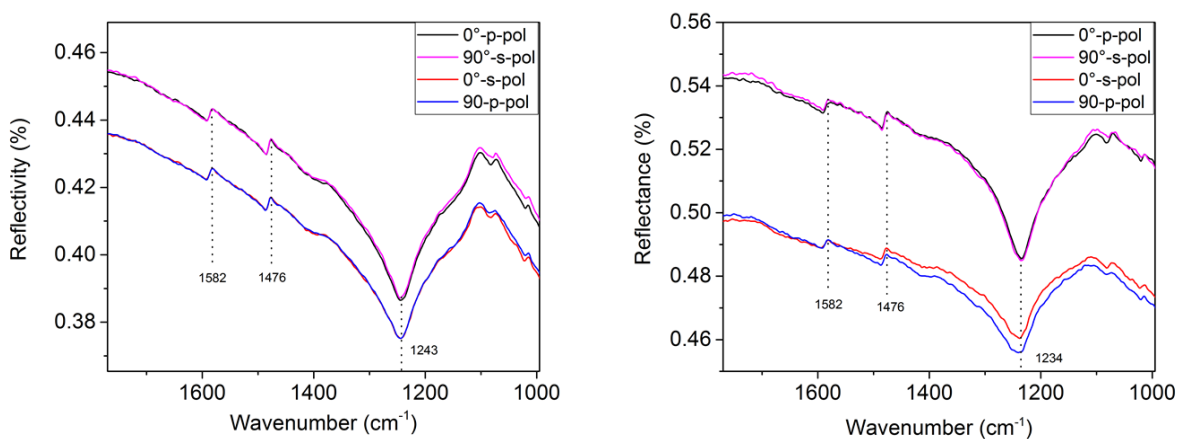


Figure 6.24: Polarized IR spectra for sample positions 0° and 90° of unrippled (left) and rippled (right) substrate. The spectra are coupled to show excitation at the same direction.

A different perspective in Figure 6.24 presents the data paired for excitation at the same direction (0°-p & 90°-s or 0°-s & 90°p). Figure 6.24 (left) shows that for an unrippled sample the signals are identical. Interestingly, in Figure 6.24 (right) the excitation direction across the ripples (0°-s & 90°p) shows difference, in the signal height, of the SiO₂ band. The results of Chapter 6.1 were pointing to a decoupling of the resonances in the direction across the ripples. A similar effect that has been noticed as well in ellipsometric measurements performed by Oates [38]. The current results support the explanation that the effect is due to the screening of the field by the shape of the underlying ripples.

Conclusions

The present chapter demonstrates the capacity of Ag nanoparticles evaporated on plain and rippled silicon to enhance the IR absorption signals of adsorbed molecules. Polarization measurements performed by a FTIR microscope exhibit the acquisition of polarization sensitive information in the IR with increased lateral resolution. The polarization dependence of the band due to the SiO₂ can be used as an intrinsic reference for sample orientation.

IR ellipsometry was performed in order to demonstrate the polarization dependent properties of the anisotropic silver nanoparticle arrays. The SEIRA effect can be isolated to one excitation direction or be active in both directions according to the plasmonic resonance tuning. The anisotropic resonances can work in synergy to provide both SERS

and SEIRA enhancements in the orthogonal directions (Figure 6.14, Figure 6.15 and Figure 6.21).

The signal enhancement was estimated to be 170 times larger than without the existence of the metal support, which is in accordance with reported values of SEIRA enhancement factors [186]. Of special interest is the area between 1000 and 1300 wavenumbers which is associated with the appearance of the localized field enhancement due to the SiO₂ and the Fano-shaped profiles. Kratz et al. noted that the enhancement of this area is following the similar enhancement to the 4-MBN bands and is not dependent on the existence of SAM, suggesting its use as a tool of a priori characterization of the enhancement [199]. Additionally, there are efforts in the tuning of anisotropic structures in order to achieve optimum enhancement by leveraging Fano-type signals [12, 204]. These conditions open up possibilities in the rational sample design where coupling of the resonances with the native oxide can bring forward increased sensitivity in IR detection of surface layers.

7 Gradient thickness silver islands as unified SERS and SEIRA substrates

The following chapter presents an alternative method developed to provide substrates with dual SERS and SEIRA properties. The substrates are in the form of gradient thickness of silver evaporated on plain and rippled silicon. Morphological, optical and vibrational spectroscopic characterization was performed in order to investigate the surface enhancing properties.

Motivation

The aim of the present thesis is to develop a new anisotropic plasmonic film fabrication method in order to combine SERS and SEIRA spectroscopy on a single substrate. The ultimate objective is that SERS and SEIRA can be measured at the same position by simply changing the polarization of the probe beam. The previous chapters elaborated on the experimental evidence that the substrates have indeed this capability. Even though Raman and IR are considered complementary methods [61], there is a gap in unified equipment that can perform dual measurements without the need to move the sample. The few exceptions of combinatorial existing devices include FT Raman and IR measurements with Raman excitation in the IR regime (FT-Raman Series RFT-6000 by Jasco Inc.TM). Sarua et al. have used a custom built setup for the study of thermal rise in semiconductors combining the high spatial resolution of Raman while being able to measure temperatures of materials that lack phonons in the examined range [205].

Analytical techniques are rapidly evolving in terms of detection limits as well as automated measuring procedures. The efficiency of combinatorial chemistry and materials science depends on the development of substrates that can maximize the amount of information for a variety of measuring techniques [206]. In the field of sensing there have been a number of combinatorial studies investigating the optimized structure for SERS enhancement [207], or the kinetics of SAMs via dip-pen nanolithography [208, 209], structural characterization and numerical methods studies in order to gain insight on the sensor response [150, 210], and combining SERS and SEIRA with electrochemical methods [80, 211].

In the previous chapters, the approach for a unified SERS and SEIRA substrate was based on optical anisotropy, where the resonance peaks in the visible range in one excitation direction can be used for surface enhanced Raman and subsequently the resonance in the orthogonal direction peaks in the IR range providing surface enhanced IR properties. The present chapter introduces an alternative solution to a unified SERS and SEIRA substrate, in the form of an evaporated silver layer with gradient thickness. The varying nanostructure along the sample provides numerous sites with optical and morphological properties that promote the corresponding surface enhancement of the analyte. These optimal sites can be used for combinatorial studies of Raman scattering and IR absorption as well as studies on optical and structural properties highlighting a versatile substrate for analytical purposes. The significant advantage of such a substrate is that there is no need for creating optimized samples, reducing reproducibility problems. Even though the concept of a gradient reagent concentration has been used in sensing materials for the realization of optical sensor arrays

[210] so far only a few studies have been performed on gradients of the metal plasmonic support. These studies examined separately the optical and structural attributes of gradient thickness silver layers contributing to the SERS signal [171, 212] or gradient thickness gold layer contributing to SEIRA [199].

Experimental details

The deposition of Ag in a vacuum chamber by thermal evaporation has a Gaussian profile. By placing a substrate further from the center of the evaporation cone, the deposition rate radially drops resulting in a sample with gradient thickness of the metal layer. Depending on the positioning of the substrate, the layer thickness can form a steep or more moderate slope allowing control over the morphology and subsequently the spectroscopic properties.

Following silver deposition on 10x10 mm² silicon substrates, 4-MBN was adsorbed on the surface according to the described procedure in 3.2. Subsequently the samples were scanned along the thickness gradient with various combinatorial techniques: Spectroscopic ellipsometry was used to extract the optical values and determine the thickness of the layer at each position. IR reflectance spectroscopy was applied for detecting surface enhanced IR absorption. SER spectroscopy with various excitation wavelengths was performed complementary to SEM imaging to correlate the topography of the layers with their enhancement properties. The measuring steps were alternating between 0.5 and 0.2 mm. As seen in Figure 7.1, every measuring technique has a different spot size, which is the limiting factor of the combinatorial methods resolution. The Raman measurement has a diameter of ~4 μm while the ellipsometer spot diameter with the use of micro-spots is 250 μm . Therefore the optical information obtained by ellipsometry is averaging over a number of areas with slightly different morphology.

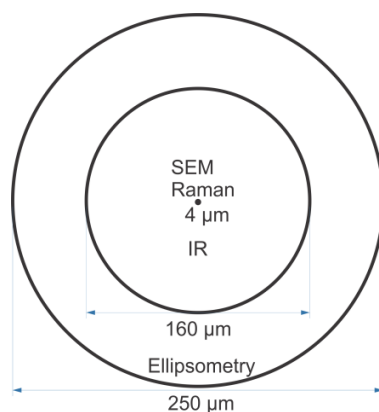


Figure 7.1: Spot-sizes of the combinatorial techniques used. The spots' diameters range from 250 μm for ellipsometry, 160 μm for IR to around 4 μm for Raman and SEM.

Gradient thickness Ag layer on plain silicon

Figure 7.2 (a) shows SEM images depicting the Ag growth at increasing deposition rate positions of the gradient film. The isolated nanoparticles in position 5 mm cover 20% of the area with an average size of 16 nm. In positions 5.5-6 mm the particle density increases to 53 % and 59 % of the area, correspondingly, with average size of 25 nm. Moving further along the line scan the density of the nanoparticles increases and they gradually start coalescing, lose their sphericity and form a percolated network of metal nano-islands.

Figure 7.2 (b) shows the imaginary part of the pseudodielectric function of the corresponding positions. At position 4 mm only silicon is present, while at position 5 the interband transition and plasmonic resonance due to the silver nanoparticles appear. Moving along the sample, the increase of the thickness of silver results in a broadened red-shifted resonance due to the increase of size and shape distribution of the nanoparticles and the decrease of interparticle distances. Figure 7.2 (c) gives an outlook of the resonance progression in the infrared region. The resonance at position 6 mm peaks in the visible region with part of the curve extending to the infrared. As the amount of deposited silver increases and fills the interspace gaps, the reflectance increases and the resonance moves to the mid-IR. With increasing volume filling factor there is a point after the percolation threshold where the behavior of the curve exhibits Drude contributions, as can be seen in Figure 10.1 (appendix). At that certain point the deposited silver behaves like a bulk material and becomes conductive.

Until position 8 mm of the presented sample, there is no shift to a solely Drude behavior as supported by Figure 10.2, appendix. The real part of the pseudodielectric function for the increasing thickness positions drops to negative values for a limited wavelength range while for the furthest presented position, 8 mm, it is negative for the visible and near-infrared and shows an upwards trend when moving to the infrared region.

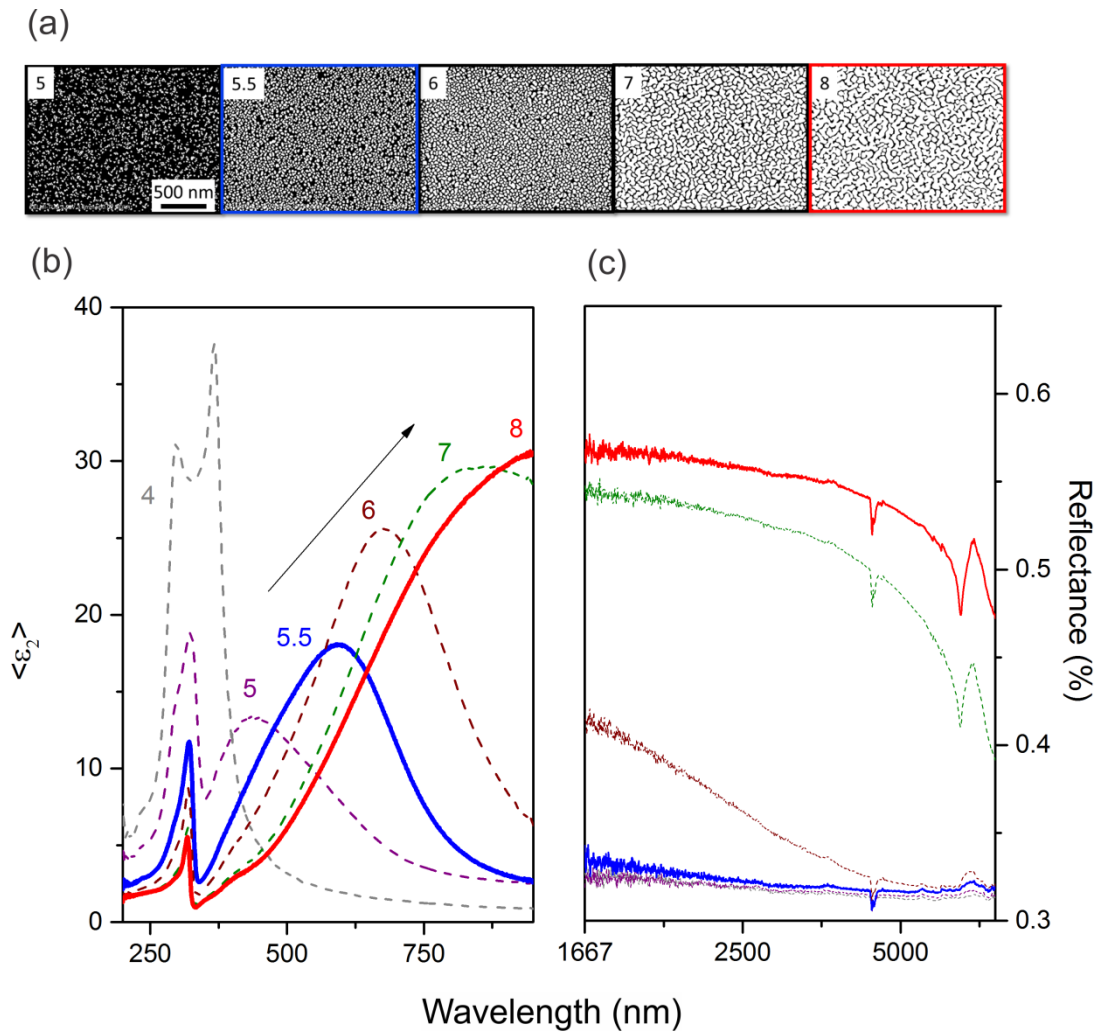


Figure 7.2: (a) SEM pictures along the gradient thickness depicting the growth of silver islands. (b) imaginary part of the pseudodielectric function showing the progression of the plasmon resonance for increasing thickness in the UV-Visible. (c) IR range measured by reflectance IR. The blue and red coloring corresponds to the positions that exhibit maximum SERS and maximum SEIRA signals for 4-MBN.

IR reflectance measurements as well as Raman scattering with an excitation wavelength of 647 nm were performed. Figure 7.3 presents the SERS and SEIRA signal height of the CN peak for positions with increasing deposition. As expected the SERS enhancement rises at an earlier position, reaching a maximum and then followed by the rise of the SEIRA enhancement upon moving to positions of increased deposition.

The positions corresponding to the SERS and SEIRA maxima are colored in Figure 7.2 with blue and red lines, correspondingly. Position at 5.5 mm, gives the best SERS signal corresponding to 53% area coverage and average nanoparticle diameter of 25 nm. Position 8 mm, with the best SEIRA signal has 77% area coverage and consists of silver islands of varying shapes and sizes. The SERS signal remains at the same levels for a distance of 1 mm and does not drop to zero until the edge of the sample. Similarly, the SEIRA signal increases

at a certain position and then remains at the same levels. This behavior is explained by observing that until the last position on the sample, the dielectric function is not that of a bulk metal (Figure 10.2, appendix).

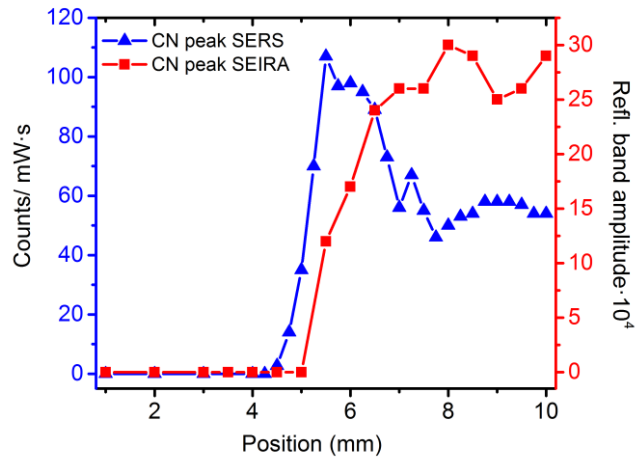


Figure 7.3: SERS and SEIRA signal of the CN peak for increasing thickness positions on the line scan.

Examining a sample placed in a different position in the emission cone a different signal profile is observed (Figure 7.4 (a)). In this case the SERS and SEIRA signals raise and drop in a distance of 2 mm, while their maxima are by 1 mm apart (versus the 2.5 mm maxima distance of the previous sample). Comparing the signal profiles of the samples leads to the suggestion that the substrate can have either defined separate areas of optimized SERS and SEIRA enhancement or can have a broader area where those features overlap. This ability is related to the steepness of the gradient, i.e. the deposition profile, and can be controlled by the positioning of the substrate during the evaporation process. The sample can be placed off center and at different depths from the evaporation cone. This results in a broad or narrow distribution of the evaporation rate and subsequently the amount of deposited material on the surface. Nevertheless, the difference in the steepness of the gradient does not appear to influence the maximum signal intensities for the different samples, that appear in the same range.

The surface enhancement properties are an interplay between the film nanostructure, its thickness and plasmonic resonance, which are all influenced by the deposition rate [114, 171, 213, 214]. Figure 7.4 (b) shows the fitted thickness of the positions on the sample, with the SERS and SEIRA active regions inside the highlighted section. The data have been modelled according to the model presented in 4.2. The mean squared error (MSE) is also indicated in the graph to give an estimation of the fitting quality. The positions of best SERS (2.4 mm) and SEIRA (3.4 mm) signals correspond to thicknesses of 12.5 nm and 21 nm, respectively. The data around this area are harder to fit, as can be seen from the increased MSE, since the area transits from isolated nanoparticles to semi-connected islands. At position 4 mm the Lorentzian of the in-plane layer is converted to a Drude function, signifying the transition from the dielectric to the metallic behavior. This change in the

model leads to the decrease of the MSE value and can also be verified by the negative declining value of the real part of the pseudodielectric function, in Figure 10.3 of the appendix [215].

Wei et al. have divided the growth zones into three sections according to their conductivity: the dielectric zone comprised by isolated nanoparticles, the transition zone of semi-connected islands showing super-linear deviation from Ohm's law and the metallic zone of a closed surface [114]. The SERS signal is diminished after the percolation threshold due to the formation of free charge carriers [212]. On the other hand, the SEIRA signal continues to have (decreasing) activity even beyond the percolation threshold, in accordance with findings of Kratz and Fahsold et al. [199, 216]. Heaps et al. mention that greater enhancements are achieved at the onset of percolation threshold with the bands assuming an asymmetrical (Fano-like) shape [201].

It is clear that the zone of percolation is a zone with diffused properties that cannot be precisely defined and quantified leading to diverse reports on the points of onset in certain behaviors. Nevertheless, the area around the percolation threshold with its complex optical and electrical properties is of special interest for various applications. Substrates that exploit these area properties have been proposed as dispersion-tunable devices for possible photovoltaic and metamaterial uses [217, 218]. Furthermore in these devices the increase of dipolar and multipolar interaction leads to a distortion of the resonance with the resulting asymmetric-line shape being used in IR detection [219, 220].

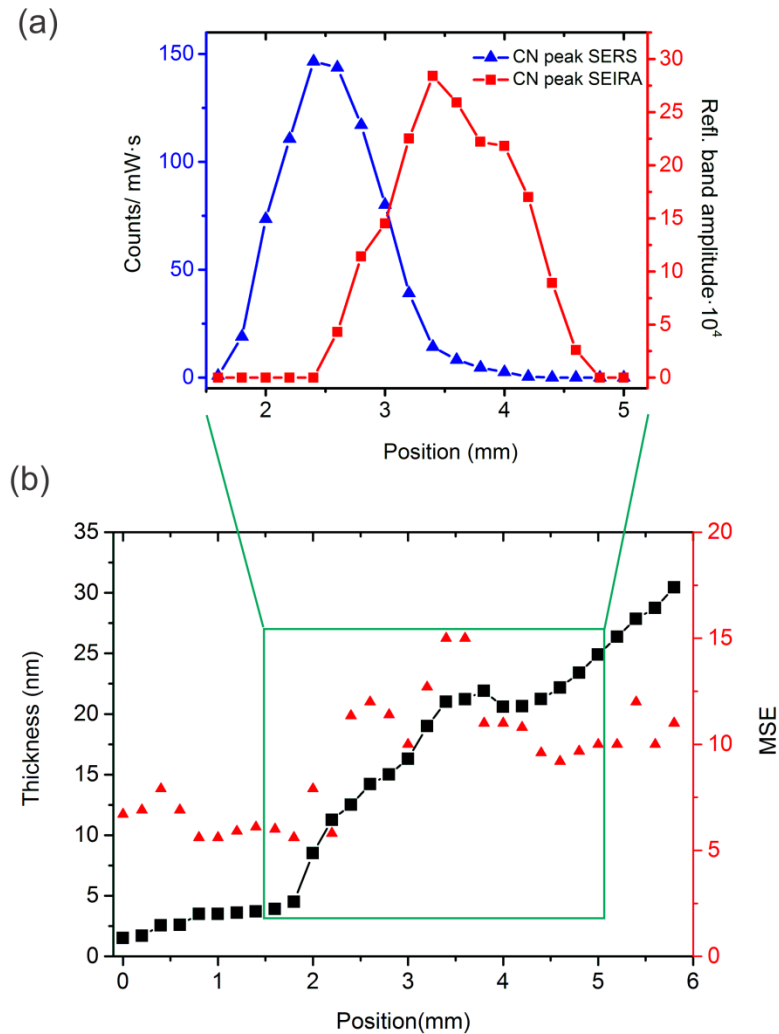


Figure 7.4: (a) The profile of SERS and SEIRA CN peak signal along the gradient thickness. (b) Fitted thickness of the Ag layer and the MSE of the fits according to Vis-ellipsometry measurements.

SERS with multiple excitation wavelength

The enhancement of an analyte is important for deciding the applicability of a substrate as sensing support. In chapter 6.2 the SERS enhancement of Ag nanoparticles on a Si rippled substrate was shown to be superior to that of an electrochemically roughened electrode. In chapter 6.3 enhancement factors for the IR regime were calculated with the use of IR-ellipsometry, showing satisfying enhancements up to a factor of 170. In the present chapter a Raman scattering line scan with different excitation wavelengths was performed in order to examine the signal profile across the different areas and determine the maximum enhancement factors that the certain substrate can provide.

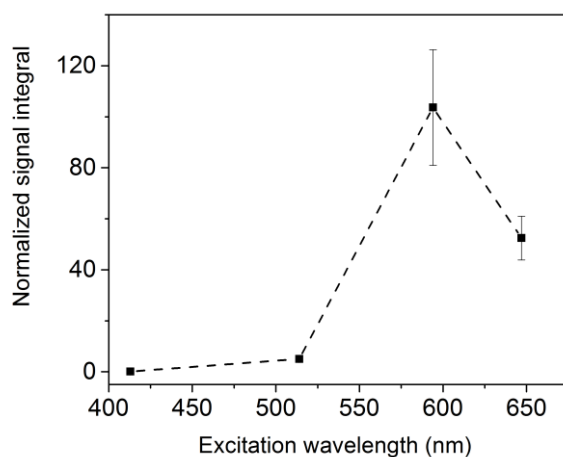


Figure 7.5: SERS CN vibration signal normalized to the signal in solution at different excitation wavelengths.

Figure 7.5 shows the SERS signal integral of the CN vibration normalized to that of a 100 mM 4-MBN solution in DMSO, in order to correct for the excitation wavelength dependency and detector sensitivity. Additionally, Table 4 presents the determined enhancement factors of the different excitation wavelengths. The EFs were calculated according to the method described in chapter 3.7, the calculation details are shown in 10.1.2, appendix.

According to Table 4, enhancements of 10^4 are achieved at excitation wavelengths 594 nm and 647 nm. The 4-MBN benzene ring mode at 1587 cm^{-1} exhibits greater enhancement than the CN vibration at 2238 cm^{-1} . As already demonstrated in Figure 5.3, the Raman signal of the CN vibration is stronger than that of the benzene ring mode in unbound 4-MBN. But the adsorption of the monolayer on the silver surface introduces surface enhancement effects that lead to relative weaker CN signal. Those effects are a combination of factors regarding the orientation of the molecule on the surface, the proximity of the respective vibration from the binding site and local symmetries of the vibrations according to their binding on Ag [136].

Another point of interest is that the EF at the 647 nm excitation is not greater than at the 594 nm, even though the plasmonic resonance is stronger at the longer wavelength. SERS is a near-field effect, deriving from hot-spot interactions. The near-field excitation is wavelength-dependent, i.e. different excitation wavelength results in different dipole interactions [221]. Depending on the local geometry, the connection of plasmonic resonance and EF may not always be linear. Especially in evaporated metal islands, which manifest fractal geometry [114].

| Excitation wavelength (nm) | 1587 cm ⁻¹ peak EF | 2238 cm ⁻¹ peak EF |
|----------------------------|-------------------------------|-------------------------------|
| 413 | 1.4·10 ² | 0.4·10 ² |
| 514 | 1.9·10 ³ | 0.9·10 ³ |
| 594 | 1.4·10 ⁴ | 1·10 ⁴ |
| 647 | 1.3·10 ⁴ | 0.7·10 ⁴ |

Table 4: SERS enhancement factors for different excitation wavelengths of the 1587 cm⁻¹ and 2238 cm⁻¹ vibrations of 4-MBN adsorbed on evaporated Ag nanoparticles.

Gradient thickness Ag layer on rippled silicon

In order to study possible template effects on the performance of the gradient thickness samples, the experiment was repeated with the use of rippled silicon instead of plain silicon as a support.

The ripple periodicity was 50 nm. The measuring steps for the ellipsometric and IR measurements were 0.5 mm and for the Raman measurements 0.25 mm, with excitation wavelength at 647 nm. The direction of the excitation was parallel to the ripples.

Figure 7.6 (a) shows the growth of the Ag nanoparticles for positions of increasing deposition rate. The nanoparticles grow preferentially along the ripples forming nanorods. The periodicity along the ripples is confirmed by the Fourier transform diagrams (Figure 7.6 (b)). Positions 4.5 and 5, where the nanorods are well-ordered, show two distinct spots at the x axis of the FFT. Moving further along the gradient, the nanorods outgrow the ripples and start coalescing, gradually resembling the morphology of a metal island network. The loss of periodicity is illustrated in the corresponding FFT pictures, where the spots convert into rings. Similar to Figure 7.2, Figure 7.6 (c) shows the progression of the imaginary part of the pseudodielectric function from low coverage positions with pronounced silicon absorption to the rise of a strong resonance that red-shifts moving to positions with increased coverage. Figure 7.6 (d) shows the corresponding evolution of the resonance in the infrared region.

Figure 7.7 presents the comparison of the SERS and SEIRA CN peak signal at positions with increasing deposition. The sample was deposited at identical conditions as the plain silicon sample presented in Figure 7.3, where a similar signal profile is observed. The SERS signal appears and reaches its maximum earlier than the SEIRA signal with their maxima having a distance of 2 mm. The fact that the SERS and SEIRA signals do not vanish until the last position illustrates a low gradient slope. A different profile of a rippled silicon substrate is shown in Figure 10.4, appendix. The corresponding SEM of the position with the highest

SERS signal (outlined in blue color) reveals a position that retains a degree of periodicity. The nanorods are of sizes 32 nm at the short axis and 42 at the long axis resulting in a 1.3 ratio and the area coverage of the metal is 63%. Accordingly, at the maximum SEIRA signal position, the island coverage is at 75% of the surface, forming a network of semi-connected islands. Even in this position there are hints of underlying periodicity as it is denoted by the elongated diffused elliptic area at the x direction of the FFT.

The presented results suggest that a gradient silver layer deposited on a rippled silicon substrate exhibits similar performance in terms of signal enhancement and signal profile across the sample with that of a plain silicon substrate. Therefore, an unnecessary step in the sample fabrication of a unified SERS and SEIRA substrate can be removed, reducing cost and preparation time. Nevertheless, the rippled silicon sample exhibits morphological and optical anisotropic properties that are useful for polarization-dependent experiments as demonstrated in Chapters 6.2 and 6.3. Therefore, the type of enhancement substrate can be chosen according to the needs of each study.

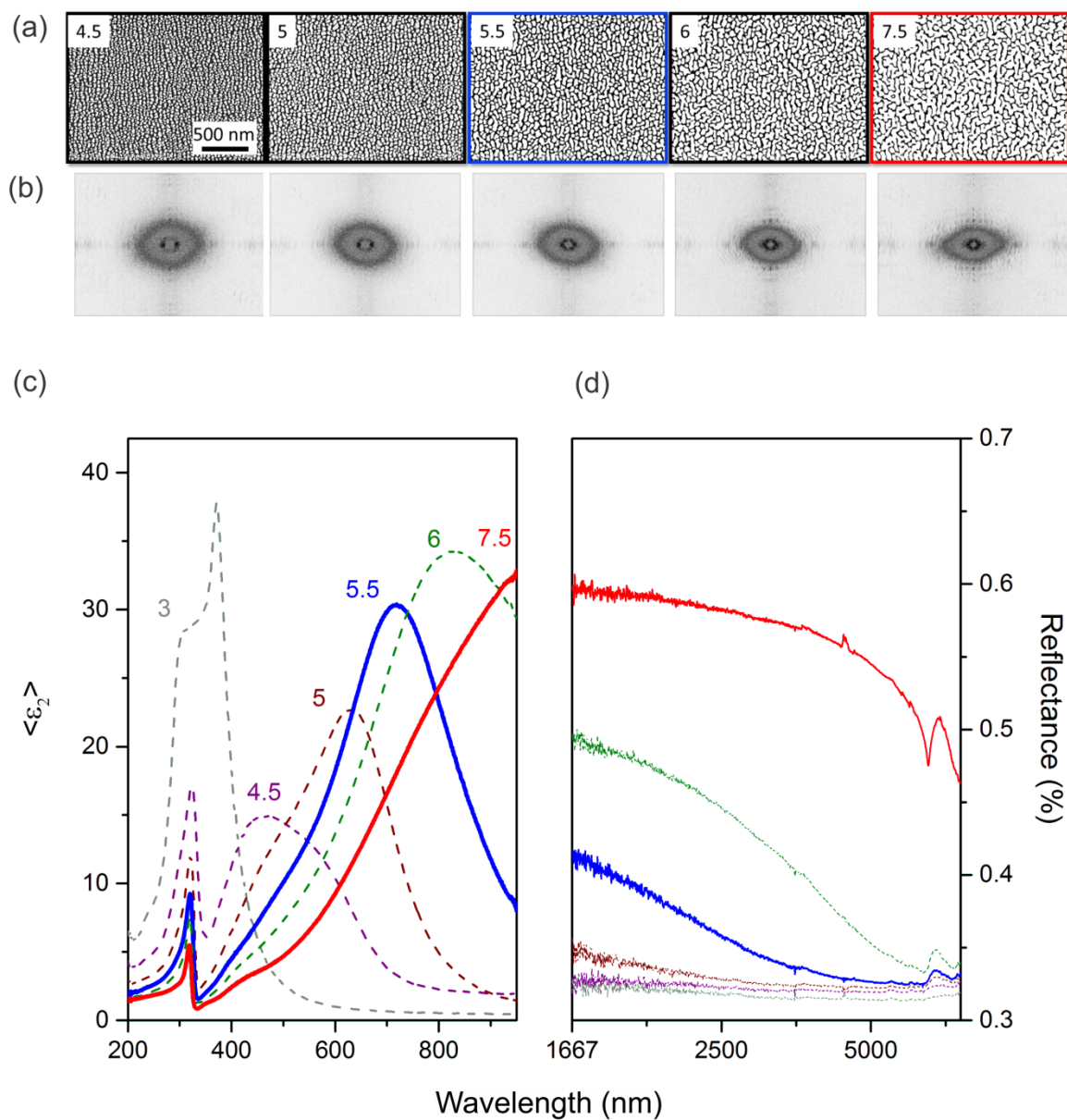


Figure 7.6: (a) SEM pictures along the gradient thickness depicting the growth of silver islands along with (b) the corresponding Fourier transformations. (c) The imaginary part of the pseudodielectric function showing the progression of the plasmon resonance for increasing thickness in the UV-Visible and (d) IR range measured by reflectance IR. The blue and red coloring corresponds to the positions that exhibit maximum SERS and maximum SEIRA signals for the molecule 4-MBN.

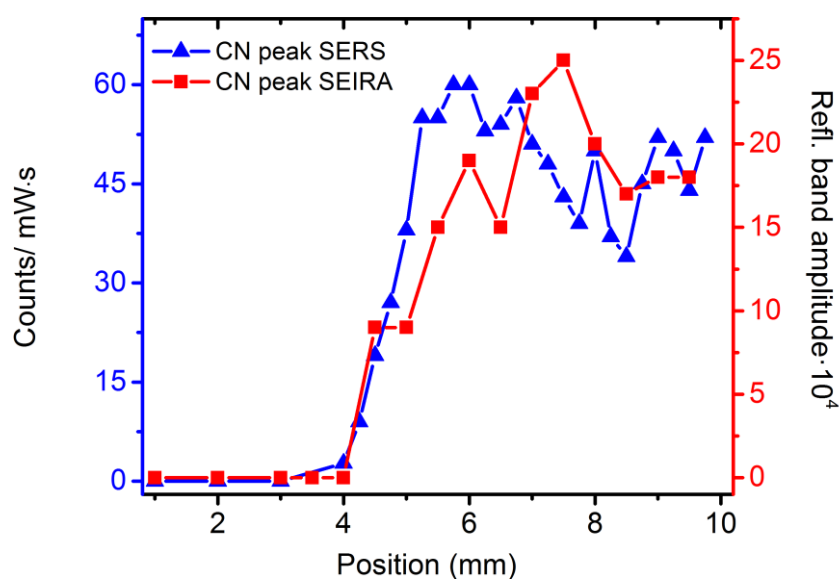


Figure 7.7: SERS and SEIRA signal of the CN peak for increasing thickness positions on the line scan.

Conclusions

In the present chapter, substrates with silver layer of gradient thickness that exhibit areas inducing Raman or IR surface enhancement were studied. The corresponding enhancement is connected to the nanostructure and the optical properties of the metal layer, exhibiting maximum SERS signals at thicknesses around 12.5 nm and maximum SEIRA signals close to the percolation threshold at around 21 nm. The use of a pre-patterned silicon substrate does not add up to the enhancement benefits, thus removing extra preparation steps unless there is the need for polarization dependent separation in the experiment.

The slope of the gradient can be controlled by the deposition process allowing the design of substrates with tailored surface enhancement properties. The need for reproducible, optimized structures is dismissed, as a line scan along the sample reveals areas where the analyte signal has a maximum enhancement in Raman scattering or IR absorption as well as overlapping areas with moderate enhancement for both effects. An additional advantage of this versatile platform is that, due to preparation, the chemical and physical treatment in every sample area is identical, in comparison to experiments using separate samples for each technique, reducing uncertainties and introducing better statistics for series of measurements.

With their considerable enhancement performance, the gradient silver island substrates are a strong candidate as sensing platforms unifying the two complementary techniques of Raman and IR on a single device.

8 Conclusions and outlook

Plasmonic substrates allowing simultaneous surface enhanced Raman scattering and infrared absorption were investigated in the present thesis. Their optical and morphological properties along with their fabrication methods were thoroughly studied with respect to their potential sensor applications. The novelty of the developed anisotropic nanoparticle arrays is the ability to provide complementary vibrational information of target analytes on a single spot.

The substrates are based on silver nanoparticles formed by evaporation on silicon. Two cases are investigated: silver deposited on plain silicon surface and silver deposited on pre-patterned, rippled silicon surface. The main focus of the research was the latter case, where the evaporation of silver on rippled silicon, at oblique angle of 70° with respect to the surface normal, leads to the formation of nanoparticle arrays. The rippled silicon was fabricated by bombardment of Ar^+ ions on polished Si (100) at 67° with respect to the surface normal. The deposited silver grows along the ripples forming arrays of nanorods, due to the ripples hindering the growth at the perpendicular direction. The structural anisotropy introduces optical anisotropy. According to near-field calculations, two localized plasmonic resonances in orthogonal directions are the physical origins of the resonances measured by ellipsometry. The direction across the ripples, at the short dipole axis, exhibits a smaller and narrower resonance while the direction along the ripples, at the long dipole axis, exhibits a red-shifted stronger and broader resonance. Far-field calculations point to decoupled resonances in the direction across the ripples and presumably coupling effects between resonances due to the elongation of the particles in the direction along the ripples. Ellipsometry was used to describe the optical activity of such substrates through the pseudodielectric function or by applying a model to extract the dielectric function of the silver layer. A biaxial model was used in order to extract the effective functions of the Ag nanoparticle arrays for the two separate probing directions along the x- and y- axes. The out-of-plane direction (z-axis) of the dielectric function is treated as a layer with equal silver and air fraction and the in-plane components of the dielectric function were described in the frame of a Brendel Oscillator model.

The deposition parameters control the morphology and the tuning of the resonances in the visible and IR range. It was concluded that ripple periodicity of 40-50 nm, even though it has increased surface roughness, is wide enough to guide the simultaneous growth along and across the ripples. For a nominal thickness of 18 nm of Ag, both resonances are in the visible range and can be leveraged for SERS purposes. Specifically, by using different excitation wavelengths corresponding to the resonance peaks and by changing the incoming polarization angle, the signal of the self-assembled monolayer (4-MBN) follows an alternating sinusoidal profile. The vibrational signal modulates according to the excitation of the resonances at the respective wavelength and polarization angle. This SERS behavior has been confirmed as well with NIR excitation sources exciting red-shifted resonances. The polarization dependence has been applied in order to distinguish between the Raman signal of surface-attached 4-MBN and that of the surrounding solution of cyclohexane,

demonstrating sensing potentiality. The SERS enhancement factors were calculated to be in the range of 10^4 .

The red-shift of the plasmonic resonances from the visible to the infrared range induces surface enhanced infrared absorption. The orthogonal directions, along and across the ripples were studied separately with IR ellipsometry, showing enhancement of the 4-MBN signals. Depending on the position of the resonances, the vibrational peaks are enhanced due to the tail of the resonance or by resonances red-shifted up to the MIR range leading to enhancement factors of 170 and Fano-shaped peak profiles. For nominal silver thickness of 24 nm, the plasmonic resonance at the direction across the ripples is confined to the visible range and at the direction along the ripples appears at the NIR, extending to the mid-IR. This configuration allowed for the dual detection of SERS and SEIRA, and in principle can be used for detection at a single spot by alternating the excitation wavelength and polarization.

In addition to developing an optimized substrate exhibiting SERS and SEIRA at orthogonal directions, an alternative solution for combining these properties is presented in the form of a gradient thickness substrate. Moving along the surface of a gradient thickness substrate the morphology exhibits isolated nanoparticles that increase in density, gradually coalescing, losing their sphericity and forming a percolated network of metal nano-islands. Therefore gradient substrates exhibit SERS and SEIRA properties at separate or partially overlapping areas along the sample surface. The proximity of those optimal positions can be controlled by the deposition parameters.

The presented unified SERS and SEIRA substrates, anisotropic nanoparticle arrays and gradient thickness nano-islands are versatile substrates in the cross-section of rationally designed sensing devices and cost-effectiveness. They provide complete vibrational information of an analyte and promote combinatorial use of the two techniques. The polarization dependency of the anisotropic substrates is an additional advantage in increasing the selectivity and specificity in biosensing applications.

A subsequent study on the present subject would be the application of substrates in in-situ environments and monitoring of real-time reactions. The investigated analyte, 4-MBN, is a non-resonant molecule. The sensitivity level would substantially increase with the use of a resonant molecule (surface enhanced resonance Raman). In combination with the wavelength and polarization dependencies, that enable multiple laser excitation experiments, the anisotropic substrates have the potential to discriminate between analytes or different areas of analytes in molecular mixtures. Adding up to sensing and molecule-specific analytics is the ability to differentiate between adsorbed and solution species, useful for investigations of surface chemistry.

Of particular interest for future studies would as well be the investigation on anisotropic nanoparticle arrays deposited on doped silicon and subsequently the possibility of this substrate being used in cyclic voltammetry as a new option for electroanalysis. As well interesting would be the investigation of the substrates with optical scanning probe techniques such as scanning near-field optical microscopy (SNOM) and tip-enhanced Raman scattering (TERS).

Finally, the techniques used in this work were those of linear optical spectroscopy. In addition to this field, there is a great potential in the non-linear spectroscopic techniques (e.g. coherent anti-Stokes Raman scattering, hyper-Raman scattering) combined with plasmonic nanostructures. The different selection rules and mechanisms can provide additional information on molecular vibrations, interface properties and help us observe ultrafast processes with great sensitivity.

9 Bibliography

- [1] R.M. Vazquez, R. Osellame, M. Cretich, M. Chiari, C. Dongre, H.J.W.M. Hoekstra, M. Pollnau, H. van den Vlekert, R. Ramponi, G. Cerullo, Optical sensing in microfluidic lab-on-a-chip by femtosecond-laser-written waveguides, *Anal Bioanal Chem*, 393 (2009) 1209-1216.
- [2] K.R. Rogers, C.L. Gerlach, Environmental biosensors - A status report, *Environ Sci Technol*, 30 (1996) A486-A491.
- [3] D. O'Hare, Biosensors and Sensor Systems, in: *Body sensor networks*, Springer London, 2014, pp. pp 55-115.
- [4] A.P. Turner, Biosensors: Fundamentals and applications - Historic book now open access, *Biosensors & bioelectronics*, 65 (2015) A1.
- [5] J. Wang, Electrochemical Glucose Biosensors, *Chem Rev*, 108 (2008) 814-825.
- [6] L.C. Clark, C. Lyons, Electrode systems for continuous monitoring in cardiovascular surgery, *Annals of the New York Academy of Sciences*, 102 (1962) 29-45.
- [7] P. Singh, SPR Biosensors: Historical Perspectives and Current Challenges, *Sensors and Actuators B: Chemical*, 229 (2016) 110-130.
- [8] K. Kneipp, Y. Wang, H. Kneipp, L.T. Perelman, I. Itzkan, R. Dasari, M.S. Feld, Single molecule detection using surface-enhanced Raman scattering (SERS), *Phys Rev Lett*, 78 (1997) 1667-1670.
- [9] P. Strobbia, E. Languirand, B.M. Cullum, Recent advances in plasmonic nanostructures for sensing: a review, *Opt Eng*, 54 (2015).
- [10] F. Siebert, P. Hildebrandt, Theory of Infrared Absorption and Raman Spectroscopy, in: *Vibrational Spectroscopy in Life Science*, Wiley-VCH Verlag GmbH & Co. KGaA, 2008, pp. 11-61.
- [11] Y. Weisheng, W. Zhihong, Y. Yang, C. Longqing, S. Ahad, W. Kimchong, W. Xianbin, Electron-beam lithography of gold nanostructures for surface-enhanced Raman scattering, *Journal of Micromechanics and Microengineering*, 22 (2012) 125007.
- [12] C. Huck, F. Neubrech, J. Vogt, A. Toma, D. Gerbert, J. Katzmann, T. Hartling, A. Pucci, Surface-Enhanced Infrared Spectroscopy Using Nanometer-Sized Gaps, *Acs Nano*, 8 (2014) 4908-4914.
- [13] J. Prinz, C. Heck, L. Ellerik, V. Merk, I. Bald, DNA origami based Au-Ag-core-shell nanoparticle dimers with single-molecule SERS sensitivity, *Nanoscale*, 8 (2016) 5612-5620.
- [14] J.J. Mock, M. Barbic, D.R. Smith, D.A. Schultz, S. Schultz, Shape effects in plasmon resonance of individual colloidal silver nanoparticles, *The Journal of Chemical Physics*, 116 (2002) 6755-6759.
- [15] F. Le, D.W. Brandl, Y.A. Urzhumov, H. Wang, J. Kundu, N.J. Halas, J. Aizpurua, P. Nordlander, Metallic nanoparticle arrays: A common substrate for both surface-enhanced Raman scattering and surface-enhanced infrared absorption, *Acs Nano*, 2 (2008) 707-718.
- [16] C. D'Andrea, J. Bochterle, A. Toma, C. Huck, F. Neubrech, E. Messina, B. Fazio, O.M. Marago, E. Di Fabrizio, M.L. de la Chapelle, P.G. Gucciardi, A. Pucci, Optical Nanoantennas for Multiband Surface-Enhanced Infrared and Raman Spectroscopy, *Acs Nano*, 7 (2013) 3522-3531.
- [17] V. Prokopec, M. Dendisova-Vyskovska, A. Kokaislova, J. Cejkova, M. Clupek, P. Matejka, Spectroscopic study of SERS- and SEIRA-activity of copper large-scaled surface substrates prepared by electrochemical deposition: What is the role of oxidation-reduction cycle treatment?, *J Mol Struct*, 993 (2011) 410-419.
- [18] M.A. Cooper, *Label-Free Biosensors: Techniques and Applications*, Cambridge University Press, Cambridge, 2009.
- [19] N. Heidary, T. Utesch, M. Zerball, M. Horch, D. Millo, J. Fritsch, O. Lenz, R. von Klitzing, P. Hildebrandt, A. Fischer, M.A. Mroginski, I. Zebger, Orientation-Controlled Electrocatalytic Efficiency of an Adsorbed Oxygen-Tolerant Hydrogenase, *Plos One*, 10 (2015).
- [20] J. Kozuch, C. Steinem, P. Hildebrandt, D. Millo, Combined Electrochemistry and Surface-Enhanced Infrared Absorption Spectroscopy of Gramicidin A Incorporated into Tethered Bilayer Lipid Membranes, *Angew Chem Int Edit*, 51 (2012) 8114-8117.
- [21] M. Sezer, P. Kielb, U. Kuhlmann, H. Mohrmann, C. Schulz, D. Heinrich, R. Schlesinger, J. Heberle, I.M. Weidinger, Surface Enhanced Resonance Raman Spectroscopy Reveals Potential

- Induced Redox and Conformational Changes of Cytochrome c Oxidase on Electrodes, *J Phys Chem B*, 119 (2015) 9586-9591.
- [22] I. Newton, A Letter of Mr. Isaac Newton, Professor of the Mathematicks in the University of Cambridge; Containing His New Theory about Light and Colors: Sent by the Author to the Publisher from Cambridge, Febr. 6. 1671/72; In Order to be Communicated to the R. Society, *Philosophical Transactions*, 6 (1671) 3075-3087.
- [23] H. Kuzmany, *Solid-State Spectroscopy*, Springer, 1999.
- [24] H. Fujiwara, *Principles of Optics*, in: *Spectroscopic Ellipsometry*, John Wiley & Sons, Ltd, 2007, pp. 13-48.
- [25] G.H. Tompkins, A.E. Irene, *Handbook of ellipsometry*, William Andrew Publishing, 2005.
- [26] M. Losurdo, Applications of ellipsometry in nanoscale science: Needs, status, achievements and future challenges, *Thin Solid Films*, 519 (2011) 2575-2583.
- [27] A. Furchner, E. Bittrich, P. Uhlmann, K.J. Eichhorn, K. Hinrichs, In-situ characterization of the temperature-sensitive swelling behavior of poly(N-isopropylacrylamide) brushes by infrared and visible ellipsometry, *Thin Solid Films*, 541 (2013) 41-45.
- [28] N. Esser, M. Rakel, C. Cobet, W.G. Schmidt, W. Braun, M. Cardona, VUV-ellipsometry on GaN: Probing conduction band properties by core level excitations, *Phys Status Solidi B*, 242 (2005) 2601-2609.
- [29] T.W.H. Oates, H. Wormeester, H. Arwin, Characterization of plasmonic effects in thin films and metamaterials using spectroscopic ellipsometry, *Prog Surf Sci*, 86 (2011) 328-376.
- [30] R.M.A. Azzam, N.M. Bashara, Generalized Ellipsometry for Surfaces with Directional Preference - Application to Diffraction Gratings, *J Opt Soc Am*, 62 (1972) 1375-1375.
- [31] C. Cobert, *Ellipsometry: A Survey of Concept*, in: *Ellipsometry of Functional Organic Surfaces and Films*, Springer, 2014.
- [32] D.E. Aspnes, Expanding horizons: new developments in ellipsometry and polarimetry, *Thin Solid Films*, 455 (2004) 3-13.
- [33] G.A. Niklasson, C.G. Granqvist, Optical-Properties and Solar Selectivity of Coevaporated Co-Al₂O₃ Composite Films, *J Appl Phys*, 55 (1984) 3382-3410.
- [34] H.A. Lorentz, Versuch einer Theorie der elektrischen und optischen Erscheinungen in bewegten Körpern, in, E.J.Brill, Leiden :, 1895.
- [35] P. Drude, Zur Elektronentheorie der Metalle, *Annalen der Physik*, 306 (1900) 566-613.
- [36] G.E. Jellison, F.A. Modine, Parameterization of the optical functions of amorphous materials in the interband region, *Appl Phys Lett*, 69 (1996) 371-373.
- [37] P.G. Etchegoin, E.C. Le Ru, M. Meyer, An analytic model for the optical properties of gold, *The Journal of Chemical Physics*, 125 (2006) 164705.
- [38] T.W.H. Oates, M. Ranjan, S. Facsko, H. Arwin, Highly anisotropic effective dielectric functions of silver nanoparticle arrays, *Opt Express*, 19 (2011) 2014-2028.
- [39] G. Arfken, H. Weber, *Mathematical Methods for Physicists*, Academic Press, 2001.
- [40] E. Margapoti, *Plasmonics: Fundamentals and Applications*, in: *Lecture notes*, TU München, 2012.
- [41] S.A. Maier, *Plasmonics: Fundamentals and Applications*, Springer, 2007.
- [42] R.F. Aroca, Plasmon enhanced spectroscopy, *Phys Chem Chem Phys*, 15 (2013) 5355-5363.
- [43] D.E. Aspnes, Plasmonics and effective-medium theories, *Thin Solid Films*, 519 (2011) 2571-2574.
- [44] P.G. Etchegoin, E.C. Le Ru, Basic Electromagnetic Theory of SERS, in: *Surface Enhanced Raman Spectroscopy*, Wiley-VCH Verlag GmbH & Co. KGaA, 2010, pp. 1-37.
- [45] E. Petryayeva, U.J. Krull, Localized surface plasmon resonance: Nanostructures, bioassays and biosensing-A review, *Anal Chim Acta*, 706 (2011) 8-24.
- [46] J.M. Pitarke, V.M. Silkin, E.V. Chulkov, P.M. Echenique, Theory of surface plasmons and surface-plasmon polaritons, *Rep Prog Phys*, 70 (2007) 1-87.
- [47] H. Raether, *Surface-Plasmons on Smooth and Rough Surfaces and on Gratings*, Springer Tr Mod Phys, 111 (1988) 1-133.
- [48] F. Wang, Y.R. Shen, General properties of local plasmons in metal nanostructures, *Phys Rev Lett*, 97 (2006).

- [49] G. Mie, Beiträge zur Optik trüber Medien, speziell kolloidaler Metallösungen, *Annalen der Physik*, 330 (1908) 377-445.
- [50] E. Stefan Kooij, B. Poelsema, Shape and size effects in the optical properties of metallic nanorods, *Phys Chem Chem Phys*, 8 (2006) 3349-3357.
- [51] S. Link, M.A. El-Sayed, Shape and size dependence of radiative, non-radiative and photothermal properties of gold nanocrystals, *Int Rev Phys Chem*, 19 (2000) 409-453.
- [52] A.T. Young, Rayleigh scattering, *Appl Optics*, 20 (1981) 533-535.
- [53] B. Schrader, *Infrared and Raman spectroscopy*, VCH Publishing.
- [54] M.J. Baker, S.R. Hussain, L. Lovergne, V. Untereiner, C. Hughes, R.A. Lukaszewski, G. Thieffin, G.D. Sockalingum, Developing and understanding biofluid vibrational spectroscopy: a critical review, *Chem Soc Rev*, 45 (2016) 1803-1818.
- [55] L.A. Woodward, *Introduction to the Theory of Molecular Vibrations & Vibrational Spectroscopy* Oxford University Press
- [56] N.o.N.M.A. 2014., Sir Venkata Raman - Facts, in, Web. 19 Jul 2016.
- [57] F. Siebert, P. Hildebrandt, *Vibrational Spectroscopy in Life Science*, Wiley-VCH Verlag GmbH & Co, 2008.
- [58] M. Sezer, PhD Thesis, Spectro-Electrochemical Investigations on Immobilised Heme Proteins, Technical University Berlin, 2011
- [59] H.K. Ly, PhD Thesis, Application of Surface Enhanced Raman Spectroscopy to Biological Systems, Technical University Berlin, 2012
- [60] D.A. Long, Introduction to Theoretical Treatments of Incoherent Light Scattering, in: *The Raman Effect*, John Wiley & Sons, Ltd, 2002, pp. 19-29.
- [61] G. Keresztury, Raman Spectroscopy: Theory, in: *Handbook of Vibrational Spectroscopy*, John Wiley & Sons, Ltd, 2006.
- [62] J. Kneipp, H. Kneipp, K. Kneipp, SERS - a single-molecule and nanoscale tool for bioanalytics, *Chem Soc Rev*, 37 (2008) 1052-1060.
- [63] D.L. Jeanmaire, R.P. Vanduyne, Surface Raman Spectroelectrochemistry .1. Heterocyclic, Aromatic, and Aliphatic-Amines Adsorbed on Anodized Silver Electrode, *J Electroanal Chem*, 84 (1977) 1-20.
- [64] M. Fleischmann, P.J. Hendra, Mcquilla.Aj, Raman-Spectra of Pyridine Adsorbed at a Silver Electrode, *Chem Phys Lett*, 26 (1974) 163-166.
- [65] J.R. Lombardi, R.L. Birke, A Unified Approach to Surface-Enhanced Raman Spectroscopy, *The Journal of Physical Chemistry C*, 112 (2008) 5605-5617.
- [66] E.C. Le Ru, E. Blackie, M. Meyer, P.G. Etchegoin, Surface enhanced Raman scattering enhancement factors: a comprehensive study, *J Phys Chem C*, 111 (2007) 13794-13803.
- [67] S. Nie, S.R. Emory, Probing Single Molecules and Single Nanoparticles by Surface-Enhanced Raman Scattering, *Science*, 275 (1997) 1102-1106.
- [68] A.B. Zrimsek, A.-I. Henry, R.P. Van Duyne, Single Molecule Surface-Enhanced Raman Spectroscopy without Nanogaps, *The Journal of Physical Chemistry Letters*, 4 (2013) 3206-3210.
- [69] A.B. Zrimsek, N.L. Wong, R.P. Van Duyne, Single Molecule Surface-Enhanced Raman Spectroscopy: A Critical Analysis of the Bianalyte versus Isotopologue Proof, *The Journal of Physical Chemistry C*, 120 (2016) 5133-5142.
- [70] P.G. Etchegoin, E.C. Le Ru, A perspective on single molecule SERS: current status and future challenges, *Phys Chem Chem Phys*, 10 (2008) 6079-6089.
- [71] E.C. Le Ru, P.G. Etchegoin, Quantifying SERS enhancements, *Mrs Bull*, 38 (2013) 631-640.
- [72] X. Wang, W. Shi, G. She, L. Mu, Surface-Enhanced Raman Scattering (SERS) on transition metal and semiconductor nanostructures, *Phys Chem Chem Phys*, 14 (2012) 5891-5901.
- [73] E.C. Le Ru, P.G. Etchegoin, Chapter 7 - Metallic colloids and other SERS substrates, in: *Principles of Surface-Enhanced Raman Spectroscopy*, Elsevier, Amsterdam, 2009, pp. 367-413.
- [74] P.G. Etchegoin, C. Galloway, E.C. Le Ru, Polarization-dependent effects in surface-enhanced Raman scattering (SERS), *Phys Chem Chem Phys*, 8 (2006) 2624-2628.
- [75] W.W. Coblentz, *Investigations of Infra-Red Spectra*, Carnegie institution of Washington, 1905.

- [76] A. Thorne, Spectrophysics, in, Springer, 1988, pp. 171-201.
- [77] J. Kozuch, PhD Thesis, Structure-Function Relationships of Membrane Proteins - Spectroelectrochemical Investigation of Artificial Membranes, Technical University Berlin, 2013
- [78] P.R. Griffiths, Introduction to Vibrational Spectroscopy, in: Handbook of Vibrational Spectroscopy, John Wiley & Sons, Ltd, 2006.
- [79] A. Hartstein, J.R. Kirtley, J.C. Tsang, Enhancement of the Infrared-Absorption from Molecular Monolayers with Thin Metal Overlayers, Phys Rev Lett, 45 (1980) 201-204.
- [80] M. Sezer, D. Millo, I.M. Weidinger, I. Zebger, P. Hildebrandt, Analyzing the catalytic processes of immobilized redox enzymes by vibrational spectroscopies, Iubmb Life, 64 (2012) 455-464.
- [81] K. Ataka, J. Heberle, Biochemical applications of surface-enhanced infrared absorption spectroscopy, Anal Bioanal Chem, 388 (2007) 47-54.
- [82] L.X. Wang, X.E. Jiang, Bioanalytical Applications of Surface-enhanced Infrared Absorption Spectroscopy, Chinese J Anal Chem, 40 (2012) 975-981.
- [83] A. Hornemann, D. Eichert, S. Flemig, G. Ulm, B. Beckhoff, Qualifying label components for effective biosensing using advanced high-throughput SEIRA methodology, Phys Chem Chem Phys, 17 (2015) 9471-9479.
- [84] M. Osawa, Surface-Enhanced Infrared Absorption Spectroscopy, in: Handbook of Vibrational Spectroscopy, John Wiley & Sons, Ltd, 2006.
- [85] M. Osawa, Dynamic Processes in Electrochemical Reactions Studied by Surface-Enhanced Infrared Absorption Spectroscopy (SEIRAS), Bulletin of the Chemical Society of Japan, 70 (1997) 2861-2880.
- [86] M.S. Anderson, Enhanced infrared absorption with dielectric nanoparticles, Appl Phys Lett, 83 (2003) 2964-2966.
- [87] M. Osawa, Surface-enhanced infrared absorption, Top Appl Phys, 81 (2001) 163-187.
- [88] M. Osawa, M. Ikeda, Surface-Enhanced Infrared-Absorption of Para-Nitrobenzoic Acid Deposited on Silver Island Films - Contributions of Electromagnetic and Chemical Mechanisms, J Phys Chem-Us, 95 (1991) 9914-9919.
- [89] F.M. Hoffmann, Infrared reflection-absorption spectroscopy of adsorbed molecules, Surface Science Reports, 3 (1983) 107-192.
- [90] M. Osawa, K. Ataka, K. Yoshii, Y. Nishikawa, Surface-Enhanced Infrared-Spectroscopy - the Origin of the Absorption Enhancement and Band Selection Rule in the Infrared-Spectra of Molecules Adsorbed on Fine Metal Particles, Appl Spectrosc, 47 (1993) 1497-1502.
- [91] G. Moula, R. Rodriguez-Oliveros, P. Albella, J.A. Sanchez-Gil, R.F. Aroca, Plasmonics and single-molecule detection in evaporated silver-island films, Annalen Der Physik, 524 (2012) 697-704.
- [92] M. Ohring, Chapter 9 - Film Structure, in: Materials Science of Thin Films (Second Edition), Academic Press, San Diego, 2002, pp. 495-558.
- [93] J.A. Venables, Introduction to Surface and Thin Film Processes, Cambridge University Press, 2000.
- [94] Bauer, Phänomenologische Theorie der Kristallabscheidung an Oberflächen. I, in: Zeitschrift für Kristallographie, 1958, pp. 372.
- [95] M. Ranjan, PhD Thesis, Metal Nanoparticles/Nanowires Self-assembly on Ripple Patterned Substrate, Technical University Dresden, 2010
- [96] A. Keller, S. Facsko, Ion-Induced Nanoscale Ripple Patterns on Si Surfaces: Theory and Experiment, Materials, 3 (2010) 4811-4841.
- [97] R.M. Bradley, J.M.E. Harper, Theory of Ripple Topography Induced by Ion-Bombardment, J Vac Sci Technol A, 6 (1988) 2390-2395.
- [98] T.W.H. Oates, A. Keller, S. Facsko, A. Mucklich, Aligned silver nanoparticles on rippled silicon templates exhibiting anisotropic plasmon absorption, Plasmonics, 2 (2007) 47-50.
- [99] B. Schreiber, Anisotropic optical properties of arranged gold nanoparticles, (2014).
- [100] T.W.H. Oates, A. Keller, S. Noda, S. Facsko, Self-organized metallic nanoparticle and nanowire arrays from ion-sputtered silicon templates, Appl Phys Lett, 93 (2008).

- [101] G. Schkolnik, J. Salewski, D. Millo, I. Zebger, S. Franzen, P. Hildebrandt, Vibrational Stark Effect of the Electric-Field Reporter 4-Mercaptobenzonitrile as a Tool for Investigating Electrostatics at Electrode/SAM/Solution Interfaces, *Int J Mol Sci*, 13 (2012) 7466-7482.
- [102] K. Hinrichs, A. Furchner, J. Rappich, T.W.H. Oates, Polarization-Dependent and Ellipsometric Infrared Microscopy for Analysis of Anisotropic Thin Films, *J Phys Chem C*, 117 (2013) 13557-13563.
- [103] C.A. Schneider, W.S. Rasband, K.W. Eliceiri, NIH Image to ImageJ: 25 years of image analysis, *Nat Methods*, 9 (2012) 671-675.
- [104] D. Necas, P. Klapetek, Gwyddion: an open-source software for SPM data analysis, *Cent Eur J Phys*, 10 (2012) 181-188.
- [105] H.K. Ly, C. Kohler, A. Fischer, J. Kabuss, F. Schlosser, M. Schoth, A. Knorr, I.M. Weidinger, Induced Surface Enhancement in Coral Pt Island Films Attached to Nanostructured Ag Electrodes, *Langmuir*, 28 (2012) 5819-5825.
- [106] A.D. McFarland, M.A. Young, J.A. Dieringer, R.P. Van Duyne, Wavelength-scanned surface-enhanced Raman excitation spectroscopy, *J Phys Chem B*, 109 (2005) 11279-11285.
- [107] L.J. Wan, M. Terashima, H. Noda, M. Osawa, Molecular orientation and ordered structure of benzenethiol adsorbed on gold(111), *J Phys Chem B*, 104 (2000) 3563-3569.
- [108] S. Trasatti, R. Parsons, Interphases in Systems of Conducting Phases (Recommendations 1985), *Pure Appl Chem*, 58 (1986) 437-454.
- [109] E.C. Le Ru, E. Blackie, M. Meyer, P.G. Etchegoin, Surface Enhanced Raman Scattering Enhancement Factors: A Comprehensive Study, *The Journal of Physical Chemistry C*, 111 (2007) 13794-13803.
- [110] P.W. Voorhees, The Theory of Ostwald Ripening, *J Stat Phys*, 38 (1985) 231-252.
- [111] J. Tang, P. Photopoulos, A. Tserapi, D. Tsoukalas, Two-dimensional nanoparticle self-assembly using plasma-induced Ostwald ripening, *Nanotechnology*, 22 (2011).
- [112] T.W.H. Oates, D.R. McKenzie, M.M.M. Bilek, Percolation threshold in ultrathin titanium films determined by in situ spectroscopic ellipsometry, *Physical Review B*, 70 (2004).
- [113] T.C. Zhang, Z.X. Mei, Y. Guo, Q.K. Xue, X.L. Du, Influence of growth temperature on formation of continuous Ag thin film on ZnO surface by ultra-high vacuum deposition (vol 42, 065303, 2009), *J Phys D Appl Phys*, 42 (2009).
- [114] H.Y. Wei, H. Eilers, From silver nanoparticles to thin films: Evolution of microstructure and electrical conduction on glass substrates, *J Phys Chem Solids*, 70 (2009) 459-465.
- [115] K.P. Vijayakumar, C. Purushothaman, Effect of Annealing on the Reflectivity of Silver Films, *Thin Solid Films*, 82 (1981) 225-227.
- [116] T.W.H. Oates, M. Losurdo, S. Noda, K. Hinrichs, The effect of atmospheric tarnishing on the optical and structural properties of silver nanoparticles, *J Phys D Appl Phys*, 46 (2013).
- [117] W.M. Moore, P.J. Codella, Oxidation of silver films by atomic oxygen, *The Journal of Physical Chemistry*, 92 (1988) 4421-4426.
- [118] C. Liang, C. Yang, N. Huang, Tarnish protection of silver by octadecanethiol self-assembled monolayers prepared in aqueous micellar solution, *Surface and Coatings Technology*, 203 (2009) 1034-1044.
- [119] H. Qi, D. Alexson, O. Glembocki, S.M. Prokes, The effect of size and size distribution on the oxidation kinetics and plasmonics of nanoscale Ag particles, *Nanotechnology*, 21 (2010).
- [120] T.W.H. Oates, Aligned metallic nanoparticles on rippled surfaces: Optical characterization using generalized ellipsometry, *Appl Surf Sci*, 258 (2012) 9278-9282.
- [121] H. Wormeester, E.S. Kooij, B. Poelsema, Effective dielectric response of nanostructured layers, *Phys Status Solidi A*, 205 (2008) 756-763.
- [122] H.H.U. Yang, J. D'Archangel, M.L. Sundheimer, E. Tucker, G.D. Boreman, M.B. Raschke, Optical dielectric function of silver, *Physical Review B*, 91 (2015).
- [123] R. Verre, K. Fleischer, C. Smith, N. McAlinden, J.F. McGilp, I.V. Shvets, Probing the out-of-plane optical response of plasmonic nanostructures using spectroscopic ellipsometry, *Physical Review B*, 84 (2011).
- [124] R. Brendel, D. Bormann, An Infrared Dielectric Function Model for Amorphous Solids, *J Appl Phys*, 71 (1992) 1-6.

- [125] M. Alt, J. Schinke, S. Hillebrandt, M. Hansel, G. Hernandez-Sosa, N. Mechau, T. Glaser, E. Mankel, M. Hamburger, K. Deing, W. Jaegermann, A. Pucci, W. Kowalsky, U. Lemmer, R. Lovrincic, Processing Follows Function: Pushing the Formation of Self-Assembled Mono layers to High-Throughput Compatible Time Scales, *ACS Appl Mater Inter*, 6 (2014) 20234-20241.
- [126] J.C. Love, L.A. Estroff, J.K. Kriebel, R.G. Nuzzo, G.M. Whitesides, Self-assembled monolayers of thiolates on metals as a form of nanotechnology, *Chem Rev*, 105 (2005) 1103-1169.
- [127] F. Sinapi, I. Lejeune, J. Delhalle, Z. Mekhalif, Comparative protective abilities of organothiols SAM coatings applied to copper dissolution in aqueous environments, *Electrochim Acta*, 52 (2007) 5182-5190.
- [128] G. Schkolnik, PhD Thesis, Vibrational Stark Spectroscopy as a Tool for Probing Electrostatics at Protein Surfaces and Self Assembled Monolayers, Technical University Berlin, 2012
- [129] C.K. Klutse, A. Mayer, J. Wittkamper, B.M. Cullum, Applications of Self-Assembled Monolayers in Surface-Enhanced Raman Scattering, *Journal of Nanotechnology*, 2012 (2012) 10.
- [130] P.E. Laibinis, G.M. Whitesides, D.L. Allara, Y.T. Tao, A.N. Parikh, R.G. Nuzzo, Comparison of the Structures and Wetting Properties of Self-Assembled Monolayers of Normal-Alkanethiols on the Coinage Metal-Surfaces, Cu, Ag, Au, *J Am Chem Soc*, 113 (1991) 7152-7167.
- [131] M.D. Hanwell, D.E. Curtis, D.C. Lonie, T. Vandermeersch, E. Zurek, G.R. Hutchison, Avogadro: an advanced semantic chemical editor, visualization, and analysis platform, *J Cheminformatics*, 4 (2012).
- [132] S. Frey, V. Stadler, K. Heister, W. Eck, M. Zharnikov, M. Grunze, B. Zeysing, A. Terfort, Structure of thioaromatic self-assembled monolayers on gold and silver, *Langmuir*, 17 (2001) 2408-2415.
- [133] S.W. Han, S.J. Lee, K. Kim, Self-assembled monolayers of aromatic thiol and selenol on silver: Comparative study of adsorptivity and stability, *Langmuir*, 17 (2001) 6981-6987.
- [134] Gaussian Software, version 09, <http://gaussian.com/>.
- [135] M. Stolarski, Prof. Dr. P. Hildebrandt's group, TU Berlin, Personal communication.
- [136] S.K. Saikin, R. Olivares-Amaya, D. Rappoport, M. Stopa, A. Aspuru-Guzik, On the chemical bonding effects in the Raman response: Benzenethiol adsorbed on silver clusters, *Phys Chem Chem Phys*, 11 (2009) 9401-9411.
- [137] H. Fujiwara, Principles of Spectroscopic Ellipsometry, in: *Spectroscopic Ellipsometry*, John Wiley & Sons, Ltd, 2007, pp. 81-146.
- [138] M.G. Moharam, E.B. Grann, D.A. Pommet, T.K. Gaylord, Formulation for Stable and Efficient Implementation of the Rigorous Coupled-Wave Analysis of Binary Gratings, *J Opt Soc Am A*, 12 (1995) 1068-1076.
- [139] M. Weismann, D.F.G. Gallagher, N.C. Panoiu, Accurate near-field calculation in the rigorous coupled-wave analysis method, *J Optics-Uk*, 17 (2015).
- [140] M.G. Moharam, T.K. Gaylord, Rigorous Coupled-Wave Analysis of Metallic Surface-Relief Gratings, *J Opt Soc Am A*, 3 (1986) 1780-1787.
- [141] F.M. Kahnert, Numerical methods in electromagnetic scattering theory, *J Quant Spectrosc Ra*, 79 (2003) 775-824.
- [142] Y.S. Foo, K.T. Cheung, C.H. To, J.A. Zapien, On the development of Finite-Difference Time-Domain for modeling the spectroscopic ellipsometry response of 1D periodic structures, *Thin Solid Films*, 571 (2014) 356-363.
- [143] M.K. Callens, H. Marsman, L. Penninck, P. Peeters, H. de Groot, J.M. ter Meulen, K. Neyts, RCWA and FDTD modeling of light emission from internally structured OLEDs, *Opt Express*, 22 (2014) A589-A600.
- [144] K.T. Cheung, Y. Foo, C.H. To, J.A. Zapien, Towards FDTD modeling of spectroscopic ellipsometry data at large angles of incidence, *Appl Surf Sci*, 281 (2013) 2-7.
- [145] C.H. Lin, H.L. Chen, W.C. Chao, C.I. Hsieh, W.H. Chang, Optical characterization of two-dimensional photonic crystals based on spectroscopic ellipsometry with rigorous coupled-wave analysis, *Microelectron Eng*, 83 (2006) 1798-1804.
- [146] D. Gkogkou, B. Schreiber, T. Shaykhutdinov, H.K. Ly, U. Kuhlmann, U. Gernert, S. Facsko, P. Hildebrandt, N. Esser, K. Hinrichs, I.M. Weidinger, T.W.H. Oates, Polarization- and Wavelength-

- Dependent Surface-Enhanced Raman Spectroscopy Using Optically Anisotropic Rippled Substrates for Sensing, *ACS Sensors*, 1 (2016) 318-323.
- [147] K. Hinrichs, In-situ Spectroscopy Group, ISAS, Personal communication.
- [148] T. Shaykhutdinov, In-Situ Spectroscopy Group, ISAS, Personal communication.
- [149] A.D. Rakic, A.B. Djuricic, J.M. Elazar, M.L. Majewski, Optical properties of metallic films for vertical-cavity optoelectronic devices, *Appl Optics*, 37 (1998) 5271-5283.
- [150] D. Gkogkou, T. Shaykhutdinov, T.W.H. Oates, U. Gernert, B. Schreiber, S. Facsko, P. Hildebrandt, I.M. Weidinger, N. Esser, K. Hinrichs, Characterization of anisotropically shaped silver nanoparticle arrays via spectroscopic ellipsometry supported by numerical optical modeling, *Appl Surf Sci*.
- [151] J.F. Betz, W.W. Yu, Y. Cheng, I.M. White, G.W. Rubloff, Simple SERS substrates: powerful, portable, and full of potential, *Phys Chem Chem Phys*, 16 (2014) 2224-2239.
- [152] G. Arfken, 15 - Integral transforms, in: *Mathematical Methods for Physicists* (Third Edition), Academic Press, 1985, pp. 794-864.
- [153] P.K. Jain, S. Eustis, M.A. El-Sayed, Plasmon coupling in nanorod assemblies: Optical absorption, discrete dipole approximation simulation, and exciton-coupling model, *J Phys Chem B*, 110 (2006) 18243-18253.
- [154] X.L. Wang, P. Gogol, E. Cambri, B. Palpant, Near- and Far-Field Effects on the Plasmon Coupling in Gold Nanoparticle Arrays, *J Phys Chem C*, 116 (2012) 24741-24747.
- [155] M. Fleischmann, P.J. Hendra, A.J. Mcquillan, Raman-Spectra of Pyridine Adsorbed at a Silver Electrode, *Chem Phys Lett*, 26 (1974) 163-166.
- [156] P. Hildebrandt, M. Stockburger, Surface-Enhanced Resonance Raman-Spectroscopy of Rhodamine-6g Adsorbed on Colloidal Silver, *J Phys Chem-Us*, 88 (1984) 5935-5944.
- [157] A.F.J. Cusano A., Giordano M., and Cutolo A., *Optochemical Nanosensors*, in: Taylor & Francis, 2012, pp. Pages 385-400.
- [158] R.A. Tripp, R.A. Dluhy, Y.P. Zhao, Novel nanostructures for SERS biosensing, *Nano Today*, 3 (2008) 31-37.
- [159] B.R. Wood, P. Caspers, G.J. Puppels, S. Pandiancherri, D. McNaughton, Resonance Raman spectroscopy of red blood cells using near-infrared laser excitation, *Anal Bioanal Chem*, 387 (2007) 1691-1703.
- [160] A. Rygula, K. Majzner, K.M. Marzec, A. Kaczor, M. Pilarczyk, M. Baranska, Raman spectroscopy of proteins: a review, *J Raman Spectrosc*, 44 (2013) 1061-1076.
- [161] T. Siebert, B. Guchhait, Y.L. Liu, R. Costard, T. Elsaesser, Anharmonic Backbone Vibrations in Ultrafast Processes at the DNA-Water Interface, *J Phys Chem B*, 119 (2015) 9670-9677.
- [162] J.R. Anema, A.G. Brolo, Use of polarization-dependent SERS from scratched gold films to monitor the electrochemically-driven desorption and readsorption of cysteine, *J Electroanal Chem*, 649 (2010) 159-163.
- [163] Q. Li, *Anisotropic Nanomaterials: Preparation, Properties, and Applications*, Springer International Publishing, 2015.
- [164] Y.P. Zhao, S.B. Chaney, S. Shanmukh, R.A. Dluhy, Polarized surface enhanced raman and absorbance spectra of aligned silver nanorod arrays, *J Phys Chem B*, 110 (2006) 3153-3157.
- [165] X.M. Lin, Y. Cui, Y.H. Xu, B. Ren, Z.Q. Tian, Surface-enhanced Raman spectroscopy: substrate-related issues, *Anal Bioanal Chem*, 394 (2009) 1729-1745.
- [166] M. Kahl, E. Voges, S. Kostrewa, C. Viets, W. Hill, Periodically structured metallic substrates for SERS, *Sensor Actuat B-Chem*, 51 (1998) 285-291.
- [167] C.A. Murray, Using surface enhanced Raman scattering to study vibrations of adsorbates on thin metallic overlayers on silver, *Journal of Electron Spectroscopy and Related Phenomena*, 29 (1983) 371-382.
- [168] M. Moskovits, Surface-Enhanced Spectroscopy, *Rev Mod Phys*, 57 (1985) 783-826.
- [169] J.P. Davies, S.J. Pachuta, R.G. Cooks, M.J. Weaver, Surface-Enhanced Raman-Scattering from Sputter-Deposited Silver Surfaces, *Anal Chem*, 58 (1986) 1290-1294.
- [170] H. Seki, Sers of Pyridine on Ag Island Films Prepared on a Sapphire Substrate, *J Vac Sci Technol*, 18 (1981) 633-637.

- [171] T.W.H. Oates, H. Sugime, S. Noda, Combinatorial Surface-Enhanced Raman Spectroscopy and Spectroscopic Ellipsometry of Silver Island Films, *J Phys Chem C*, 113 (2009) 4820-4828.
- [172] J. Perumal, K.V. Kong, U.S. Dinish, R.M. Bakker, M. Olivo, Design and fabrication of random silver films as substrate for SERS based nano-stress sensing of proteins, *Rsc Adv*, 4 (2014) 12995-13000.
- [173] G. Santoro, S. Yu, M. Schwartzkopf, P. Zhang, S.K. Vayalil, J.F.H. Risch, M.A. Rubhausen, M. Hernandez, C. Domingo, S.V. Roth, Silver substrates for surface enhanced Raman scattering: Correlation between nanostructure and Raman scattering enhancement, *Appl Phys Lett*, 104 (2014).
- [174] D. Babonneau, S. Camelio, L. Simonot, F. Pailloux, P. Guerin, B. Lamongie, O. Lyon, Tunable plasmonic dichroism of Au nanoparticles self-aligned on rippled Al₂O₃ thin films, *Epl-Europhys Lett*, 93 (2011).
- [175] L. Anghinolfi, R. Moroni, L. Mattera, M. Canepa, F. Bisio, Flexible Tuning of Shape and Arrangement of Au Nanoparticles in 2-Dimensional Self-Organized Arrays: Morphology and Plasmonic Response, *J Phys Chem C*, 115 (2011) 14036-14043.
- [176] F. Bisio, G. Gonella, G. Maidecchi, R. Buzio, A. Gerbi, R. Moroni, A. Giglia, M. Canepa, Broadband plasmonic response of self-organized aluminium nanowire arrays, *J Phys D Appl Phys*, 48 (2015).
- [177] M. Ranjan, S. Facsko, M. Fritzsche, S. Mukherjee, Plasmon resonance tuning in Ag nanoparticles arrays grown on ripple patterned templates, *Microelectron Eng*, 102 (2013) 44-47.
- [178] C. D'Andrea, B. Fazio, P.G. Gucciardi, M.C. Giordano, C. Martella, D. Chiappe, A. Toma, F.B. de Mongeot, F. Tantussi, P. Vasanthakumar, F. Fuso, M. Allegrini, SERS Enhancement and Field Confinement in Nanosensors Based on Self-Organized Gold Nanowires Produced by Ion-Beam Sputtering, *J Phys Chem C*, 118 (2014) 8571-8580.
- [179] B. Fazio, C. D'Andrea, F. Bonaccorso, A. Irrera, G. Calogero, C. Vasi, P.G. Gucciardi, M. Allegrini, A. Toma, D. Chiappe, C. Martella, F.B. de Mongeot, Re-radiation Enhancement in Polarized Surface-Enhanced Resonant Raman Scattering of Randomly Oriented Molecules on Self-Organized Gold Nanowires, *Acs Nano*, 5 (2011) 5945-5956.
- [180] T. Shegai, Z.P. Li, T. Dadoosh, Z.Y. Zhang, H.X. Xu, G. Haran, Managing light polarization via plasmon-molecule interactions within an asymmetric metal nanoparticle trimer, *P Natl Acad Sci USA*, 105 (2008) 16448-16453.
- [181] M. Ranjan, S. Facsko, Anisotropic surface enhanced Raman scattering in nanoparticle and nanowire arrays, *Nanotechnology*, 23 (2012).
- [182] A.G. Brolo, E. Arctander, C.J. Addison, Strong polarized enhanced Raman scattering via optical tunneling through random parallel nanostructures in Au thin films, *J Phys Chem B*, 109 (2005) 401-405.
- [183] T. Itoh, K. Hashimoto, Y. Ozaki, Polarization dependences of surface plasmon bands and surface-enhanced Raman bands of single Ag nanoparticles, *Appl Phys Lett*, 83 (2003) 2274-2276.
- [184] H.X. Xu, M. Kall, Polarization-dependent surface-enhanced Raman spectroscopy of isolated silver nanoaggregates, *Chemphyschem*, 4 (2003) 1001-1005.
- [185] Z.G. Dai, X.H. Xiao, L. Liao, J.J. Ying, F. Mei, W. Wu, F. Ren, W.Q. Li, C.Z. Jiang, Enhanced and polarization dependence of surface-enhanced Raman scattering in silver nanoparticle array-nanowire systems, *Appl Phys Lett*, 102 (2013).
- [186] R.F. Aroca, D.J. Ross, C. Domingo, Surface-enhanced infrared spectroscopy, *Appl Spectrosc*, 58 (2004) 324a-338a.
- [187] R. Adato, H. Altug, In-situ ultra-sensitive infrared absorption spectroscopy of biomolecule interactions in real time with plasmonic nanoantennas, *Nat Commun*, 4 (2013).
- [188] K. Ataka, S.T. Stripp, J. Heberle, Surface-enhanced infrared absorption spectroscopy (SEIRAS) to probe monolayers of membrane proteins, *Bba-Biomembranes*, 1828 (2013) 2283-2293.
- [189] P. Kielb, M. Sezer, S. Katz, F. Lopez, C. Schulz, L. Gorton, R. Ludwig, U. Wollenberger, I. Zebger, I.M. Weidinger, Spectroscopic Observation of Calcium-Induced Reorientation of

Cellobiose Dehydrogenase Immobilized on Electrodes and its Effect on Electrocatalytic Activity, *Chemphyschem*, 16 (2015) 1960-1968.

[190] Y. Nishikawa, K. Fujiwara, K. Ataka, M. Osawa, Surface-enhanced infrared external reflection spectroscopy at low reflective surfaces and its application to surface analysis of semiconductors, glasses, and polymers, *Anal Chem*, 65 (1993) 556-562.

[191] L.V. Brown, K. Zhao, N. King, H. Sobhani, P. Nordlander, N.J. Halas, Surface-Enhanced Infrared Absorption Using Individual Cross Antennas Tailored to Chemical Moieties, *J Am Chem Soc*, 135 (2013) 3688-3695.

[192] K. Weber, M.L. Nesterov, T. Weiss, M. Scherer, M. Hentschel, J. Vogt, C. Huck, W. Li, M. Dressel, H. Giessen, F. Neubrech, Wavelength Scaling in Antenna-Enhanced Infrared Spectroscopy: Towards the Far-IR and THz Region, *ACS Photonics*, (2016).

[193] F. Neubrech, A. Pucci, T.W. Cornelius, S. Karim, A. Garcia-Etxarri, J. Aizpurua, Resonant Plasmonic and Vibrational Coupling in a Tailored Nanoantenna for Infrared Detection, *Phys Rev Lett*, 101 (2008).

[194] Y.J. Zhong, S.D. Malagari, T. Hamilton, D. Wasserman, Review of mid-infrared plasmonic materials, *J Nanophotonics*, 9 (2015).

[195] T.W.H. Oates, T. Shaykhutdinov, T. Wagner, A. Furchner, K. Hinrichs, Mid-infrared gyrotropy in split-ring resonators measured by Mueller matrix ellipsometry, *Opt Mater Express*, 4 (2014) 2646-2655.

[196] A. Kroning, A. Furchner, D. Aulich, E. Bittrich, S. Rauch, P. Uhlmann, K.J. Eichhorn, M. Seeber, I. Luginov, S.M. Kilbey, B.S. Lokitz, S. Minko, K. Hinrichs, In Situ Infrared Ellipsometry for Protein Adsorption Studies on Ultrathin Smart Polymer Brushes in Aqueous Environment, *ACS Appl Mater Inter*, 7 (2015) 12430-12439.

[197] A. Röseler, E.-H. Korte, Infrared Spectroscopic Ellipsometry, in: *Handbook of Vibrational Spectroscopy*, John Wiley & Sons, Ltd, 2006.

[198] A. Furchner, Spectroscopic infrared ellipsometry on functional polymer films, Technical University Berlin, 2014

[199] C. Kratz, T.W.H. Oates, K. Hinrichs, Optimization and quantification of surface enhanced infrared absorption using gradient gold island films, *Thin Solid Films*.

[200] I.I. Shaganov, T.S. Perova, R.A. Moore, K. Berwick, Spectroscopic characteristics of SiO and SiO₂ solid films: Assignment and local field effect influence, *J Mater Sci-Mater El*, 12 (2001) 351-355.

[201] D.A. Heaps, P.R. Griffiths, Band shapes in the infrared spectra of thin organic films on metal nanoparticles, *Vib Spectrosc*, 42 (2006) 45-50.

[202] V. Giannini, Y. Francescato, H. Amrania, C.C. Phillips, S.A. Maier, Fano Resonances in Nanoscale Plasmonic Systems: A Parameter-Free Modeling Approach, *Nano Lett*, 11 (2011) 2835-2840.

[203] K. Hinrichs, A. Furchner, G.G. Sun, M. Gensch, J. Rappich, T.W.H. Oates, Infrared ellipsometry for improved laterally resolved analysis of thin films, *Thin Solid Films*, 571 (2014) 648-652.

[204] F. Neubrech, D. Weber, D. Enders, T. Nagao, A. Pucci, Antenna Sensing of Surface Phonon Polaritons, *J Phys Chem C*, 114 (2010) 7299-7301.

[205] A. Sarua, Combined Infrared and Raman temperature measurements on device structures, in: *CS MANTECH Conference*, Vancouver, British Columbia, Canada, 2006.

[206] R.A. Potyrailo, V.M. Mirsky, Combinatorial and high-throughput development of sensing materials: The first 10 years, *Chem Rev*, 108 (2008) 770-813.

[207] B.E. Baker, N.J. Kline, P.J. Treado, M.J. Natan, Solution-based assembly of metal surfaces by combinatorial methods, *J Am Chem Soc*, 118 (1996) 8721-8722.

[208] A. Ivanisevic, K.V. McCumber, C.A. Mirkin, Site-directed exchange studies with combinatorial libraries of nanostructures, *J Am Chem Soc*, 124 (2002) 11997-12001.

[209] C.A. Mirkin, Dip-pen nanolithography: Automated fabrication of custom multicomponent, sub-100-nanometer surface architectures, *Mrs Bull*, 26 (2001) 535-538.

- [210] R.A. Potyrailo, L. Hassib, Analytical instrumentation infrastructure for combinatorial and high-throughput development of formulated discrete and gradient polymeric sensor materials arrays, *Review of Scientific Instruments*, 76 (2005) 062225.
- [211] H.K. Ly, M. Sezer, N. Wisitruangsakul, J.J. Feng, A. Kranich, D. Millo, I.M. Weidinger, I. Zebger, D.H. Murgida, P. Hildebrandt, Surface-enhanced vibrational spectroscopy for probing transient interactions of proteins with biomimetic interfaces: electric field effects on structure, dynamics and function of cytochrome c, *Febs J*, 278 (2011) 1382-1390.
- [212] E. Vogel, W. Kiefer, V. Deckert, D. Zeisel, Laser-deposited Silver Island films: An investigation of their structure, optical properties and SERS activity, *J Raman Spectrosc*, 29 (1998) 693-702.
- [213] U. Kreibig, L. Genzel, Optical absorption of small metallic particles, *Surface Science*, 156 (1985) 678-700.
- [214] V.L. Schlegel, T.M. Cotton, Silver-Island Films as Substrates for Enhanced Raman-Scattering - Effect of Deposition Rate on Intensity, *Anal Chem*, 63 (1991) 241-247.
- [215] A.J. de Vries, E.S. Kooij, H. Wormeester, A.A. Mewe, B. Poelsema, Ellipsometric study of percolation in electroless deposited silver films, *J Appl Phys*, 101 (2007).
- [216] G. Fahsold, A. Bartel, O. Krauth, N. Magg, A. Pucci, Infrared optical properties of ultrathin Fe films on MgO(001) beyond the percolation threshold, *Physical Review B*, 61 (2000) 14108-14113.
- [217] A.Q. Chen, M. Deutsch, Tunable asymmetric reflectance in silver films near the percolation threshold, *J Appl Phys*, 109 (2011).
- [218] T.W.H. Oates, L. Ryves, M.M.M. Bilek, Dielectric functions of a growing silver film determined using dynamic in situ spectroscopic ellipsometry, *Opt Express*, 16 (2008) 2302-2314.
- [219] A. Priebe, M. Sinther, G. Fahsold, A. Pucci, The correlation between film thickness and adsorbate line shape in surface enhanced infrared absorption, *J Chem Phys*, 119 (2003) 4887-4890.
- [220] O. Krauth, G. Fahsold, N. Magg, A. Pucci, Anomalous infrared transmission of adsorbates on ultrathin metal films: Fano effect near the percolation threshold, *J Chem Phys*, 113 (2000) 6330-6333.
- [221] V.A. Markel, V.M. Shalaev, P. Zhang, W. Huynh, L. Tay, T.L. Haslett, M. Moskovits, Near-field optical spectroscopy of individual surface-plasmon modes in colloid clusters, *Physical Review B*, 59 (1999) 10903-10909.

10 Appendix

10.1.1 Supplementary graphs to Chapter 7

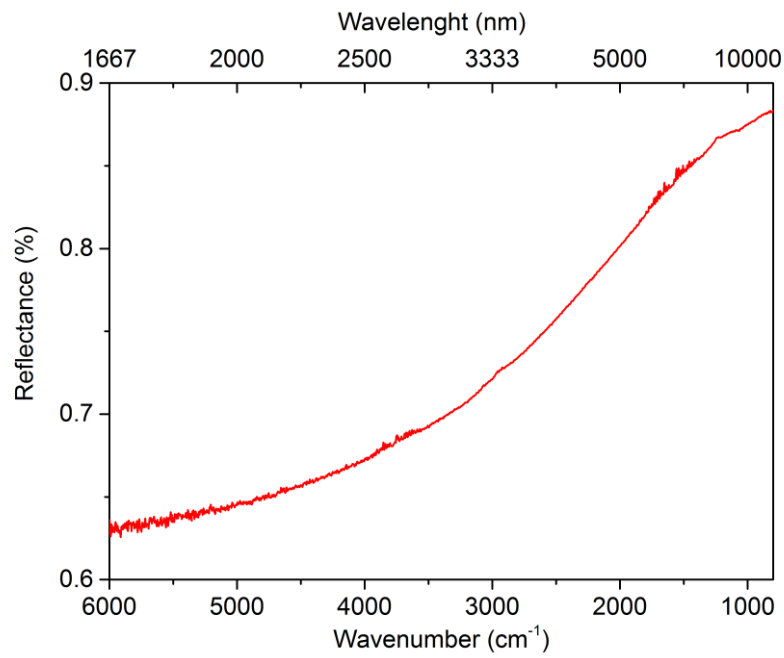


Figure 10.1: IR reflectance measurement of bulk evaporated Ag layer exhibiting Drude behavior.

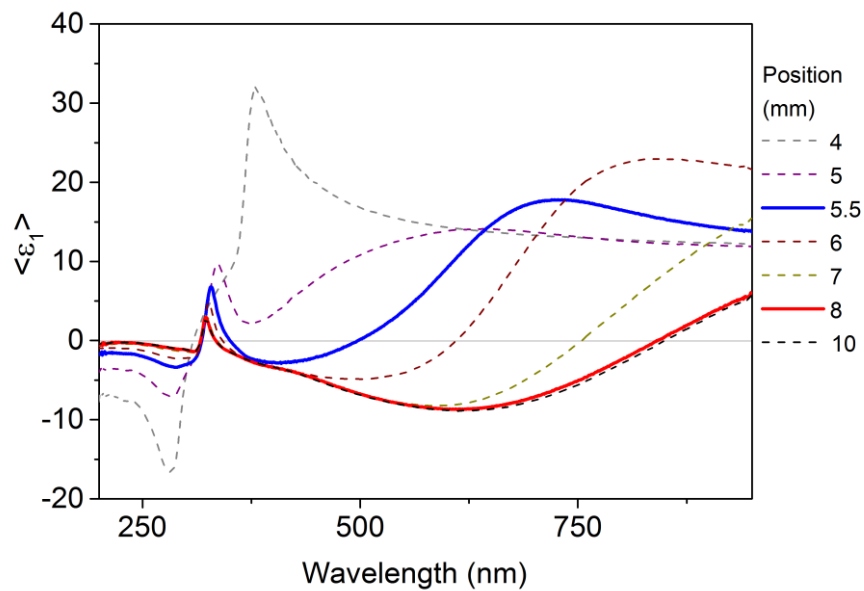


Figure 10.2: Real part of the pseudodielectric function of positions with increasing Ag thickness, as shown in Figure 7.2.

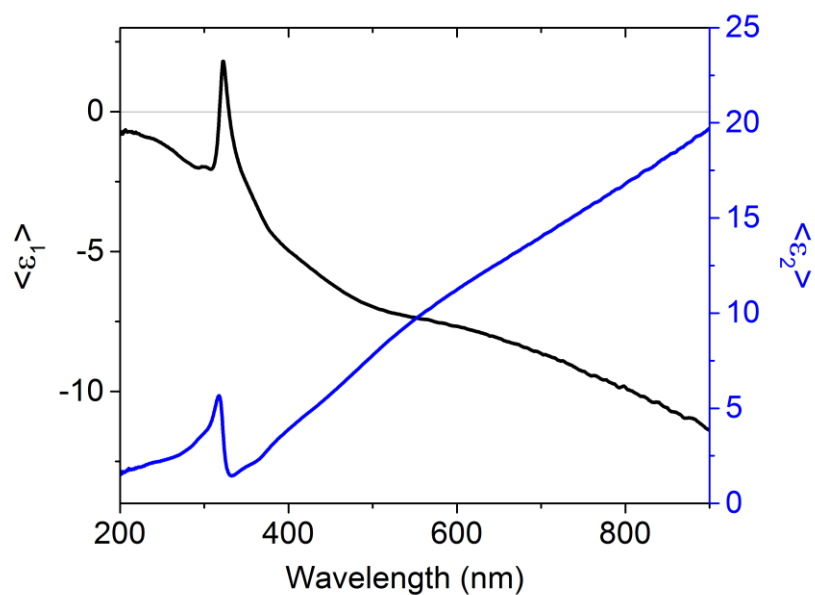


Figure 10.3: Real (black line) and imaginary part (blue line) of the pseudodielectric function of a thick Ag layer.

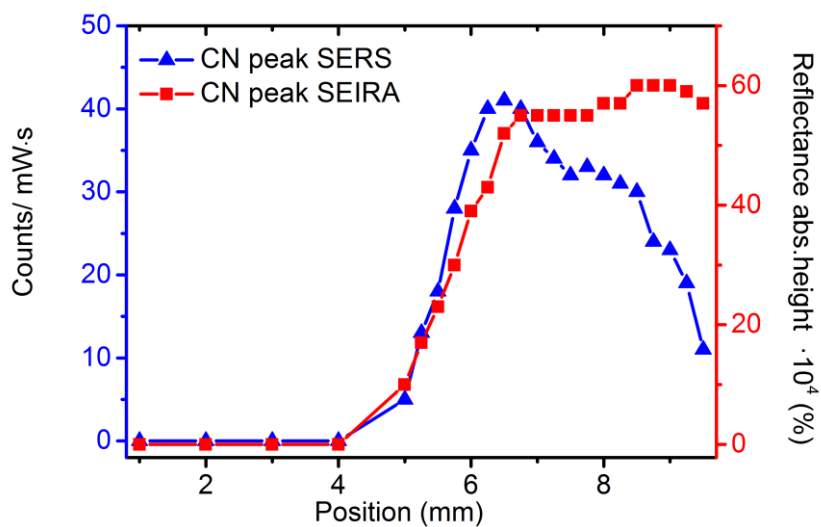


Figure 10.4: Absolute height of SERS and SEIRA signal of the CN peak for increasing thickness positions on the line scan of a gradient Ag layer on rippled silicon substrate.

10.1.2 EF calculation of Chapter 7

The enhancement factor calculation was based on position with thickness 14 nm and particle diameter 35 nm, as estimated by SEM. The calculation of the surface area of half-spheroids leads to the calculation of $RF=0.9$.

11 List of figures

| | |
|---|----|
| Figure 2.1: Representation of linear light polarization (top), in the case of equal wave amplitude of the E_x and E_y fields and phase difference 0 or π . In the general case (bottom), the resulting light polarization is elliptical. | 6 |
| Figure 2.2: Reflection and transmission of the electric field E at the planar interface . The p -polarization component is parallel to the plane of the paper and the s -polarization perpendicular to it. | 7 |
| Figure 2.3: Principle of ellipsometry. Linearly polarized light is reflected off the sample's surface resulting in elliptically polarized light. The amplitude ratio and phase difference of p - and s - components are the measured ellipsometric quantities Ψ and Δ | 9 |
| Figure 2.4: Extinction cross section of Mie scattering for a single Ag sphere in vacuum (Calculated by MiePlot v4.5 @Philip Laven) | 13 |
| Figure 2.5: Near-field coupling between metallic nanoparticles, resulting in blue (a) or red (b) shifting of the dipole resonance frequency. | 14 |
| Figure 2.6: Jablonski diagram of transitions in vibrational spectroscopy [54]. | 15 |
| Figure 2.7: A 'hot-spot' created in the cavity between a dimer and the rapid change of enhancement factor with the distance. Adapted from [70]. | 18 |
| Figure 2.8: Extinction (black), absorption (red), and scattering (blue) spectra calculated for Ag nanoparticles of different shapes. (f) shows extinction spectra of rectangular bars with aspect ratios of 2 (black), 3 (red), and 4 (blue). Note that the nonspherical particles typically exhibit multiple, red-shifted resonance peaks. Reprinted with permission from [45]. | 20 |
| Figure 2.9: Electromagnetic mechanism of SEIRA. The electric field of incident IR light induces a dipole p in the metal island generating an enhanced local electric field around the particles. Also, the molecular vibrations induce an additional dipole δp and perturb the optical properties of the metal. | 23 |
| Figure 2.10: Heterogenous nucleation on substrate surface by vapor deposition. | 24 |
| Figure 3.1: Ag evaporation schematics | 27 |
| Figure 3.2: The Raman measuring setup following the laser path. M: reflection mirror, P: Polarizer, A: Analyzer. The beam polarization is indicated by the arrows. | 29 |
| Figure 3.3: Polarization directions of the IR beam that passes through the polarizer. | 30 |
| Figure 4.1: Ag layer thickness (black squares) and growth rate (blue triangles) as a function of deposition time. | 36 |
| Figure 4.2: SEM image of evaporated Ag layer of nominal thickness 40 nm. | 36 |
| Figure 4.3: AFM topography of Ag nano-islands before (left) and after (middle) annealing for 1 hour at 300°. Right, is the corresponding imaginary part of the pseudodielectric function. | 37 |
| Figure 4.4: Optical response due to time degradation of Ag nanoparticles after 4-MBN adsorption. | 38 |
| Figure 4.5: Left, AFM topography of a rippled substrate. The Fourier transform, inset, illustrates the strong periodicity. The colored arrows note the direction of the incoming ion beam and the Ag evaporation. Right, the ripple amplitude along a line scan. The ripple periodicity is ~ 25 nm. | 39 |
| Figure 4.6: SEM images depicting the growth of silver on ripples with periodicity ~ 25 nm. The nominal thickness is 8 nm (left) and 16 nm (right). | 39 |
| Figure 4.7: Left, imaginary part of the pseudodielectric function corresponding to the excitation direction perpendicular (blue solid line) and parallel (black dashed line) to the ripples. Right, SEM image of the corresponding topography. | 40 |
| Figure 4.8: (left) experimental and fitted Ψ and Δ values with the corresponding (middle) ϵ_{xy} and (right) ϵ_z model layers of the uniaxial model for different Ag layer thicknesses. | 43 |
| Figure 4.9: (a) ϵ_{xy} and (b) ϵ_z of a 7 nm Ag layer and (c) ϵ_{xy} , (d) ϵ_z of a 32 nm layer. | 44 |
| Figure 5.1: 4-mercaptobenzonitrile (4-MBN) molecule. | 46 |
| Figure 5.2: Calculated IR and Raman active vibrational frequencies. | 47 |
| Figure 5.3: Raman spectra of unbound 4-MBN (above) and 4-MBN adsorbed on silver islands (below). | 47 |

| | |
|--|----|
| Figure 6.1: Statistics-based x/y-periodic Ag ellipsoid model of the sample. The size of the nanoparticles is 26 and 45 nm at the x and y directions, respectively. Reprinted with permission from [150]. | 49 |
| Figure 6.2: Left, SEM image showing Ag nanoparticles deposited along the silicon substrate ripples. The particle long axis of the islands is aligned parallel to the ripples. Right, particle size distribution for the x and y directions. Reprinted with permission from [150]. | 50 |
| Figure 6.3: Fourier transformation of the SEM image showing increased periodicity at the x axis. | 51 |
| Figure 6.4: Left, ellipsometrically determined pseudo-absorption index for 70° angle of incidence of the sample for the two orthogonal directions, across (\perp) and along the ripples (\parallel). Right, absorption index of the nanoparticle layer as determined from the described model. The maximum absorption appears at 468 nm and 667 nm for the x and y axis, respectively. Reprinted with permission from [150]. | 52 |
| Figure 6.5: Near-field simulations showing the amplitude of the total near-field under periodic boundary conditions (z-direction cut through the unit cell) at the k_x (left) and k_y (right) maxima. Reprinted with permission from ref. [146]. | 53 |
| Figure 6.6: Far-field simulations (cascaded and normalized) of the absorption for x- (left) and y-polarized (right) normal incident field. The legend indicates the ellipsoid separation distance in the x- and y- direction. Measured maxima of k (taken from Fig. 4) are marked in the plots. Reprinted with permission from [150]. | 54 |
| Figure 6.7: The Raman setup for polarized measurements. ϑ is defined as the angle between the laser polarization direction and the axis perpendicular to the ripples (\perp). Reprinted with permission from [146]. | 58 |
| Figure 6.8: SEM image showing silver nanoparticles aligned along nanoripples on silicon. The long axis of the islands is aligned along the ripples. Reprinted with permission from [146]. | 58 |
| Figure 6.9: Optical resonances for the directions \perp (blue), with dipole excitation on the short axis, and \parallel (dashed black), with dipole excitation on the long axis. The vertical lines indicate the positions of the 514 nm and 647 nm excitation wavelengths used in the SER experiments. Reprinted with permission from [146]. | 59 |
| Figure 6.10: Normalized intensity of the 1079 cm^{-1} band of 4-MBN as function of ϑ obtained with 514 nm excitation. Top data (blue squares) stand for parallel polarized configuration and bottom data (green circles) stand for the cross polarized configuration. | 60 |
| Figure 6.11: Normalized intensity of the 1587 cm^{-1} band of 4-MBN as function of ϑ obtained with 514 nm excitation without the use of analyzer (left), and analyzer set in parallel polarized position (right). | 60 |
| Figure 6.12: SERS spectra of 4-MBN obtained with 647 nm excitation on anisotropic sample with polarization direction along the islands long axis. Reprinted with permission from [146]. | 61 |
| Figure 6.13: Normalized intensity of the 1079 cm^{-1} band of 4-MBN as function of ϑ obtained with 514 nm (green triangles) and the 647 nm (red squares) excitation. The respective solid lines correspond to fits of a $\cos^2(\vartheta)$ (green) and $\sin^2(\vartheta)$ (red) function to the data. Reprinted with permission from [146]. | 62 |
| Figure 6.14: Left, optical resonances for the directions \perp (blue), with dipole excitation on the short axis, and \parallel (dashed black), with dipole excitation on the long axis. The vertical lines indicate the position of the 514 nm and 785 nm excitation wavelength used in the SER experiments. Right, SEM image of the corresponding geometry. | 63 |
| Figure 6.15: Normalized intensity of the 1079 cm^{-1} band of 4-MBN as function of ϑ obtained with 514 nm (green triangles) and the 785 nm (brown squares) excitation. The respective solid lines correspond to fits of a $\cos^2(\vartheta)$ (green) and $\sin^2(\vartheta)$ (brown) function to the data. | 63 |
| Figure 6.16: Top: Cyclohexane solution signal on Silicon surface for 514 nm excitation. Bottom: Cyclohexane solution and adsorbed 4-MBN signal of anisotropic Ag nanoparticles on rippled silicon surface for 514 nm excitation. | 65 |
| Figure 6.17: Left, Schematics of the Ag nanoparticles substrate with the adsorbed 4-MBN placed in the cyclohexane solution. Right, normalized intensities of the 1587 cm^{-1} SER band of adsorbed 4-MBN and the 800 cm^{-1} Raman band of cyclohexane as a function of ϑ , obtained with 514 nm excitation. | 65 |
| Figure 6.18: Morphology and imaginary part of pseudodielectric function of Ag nano-islands. | 68 |
| Figure 6.19: Corresponding SEIRA reflectance spectrum of 4-MBN adsorbed on Ag nano-islands. | 68 |

| | |
|---|-----|
| Figure 6.20: (a,b,c) SEM pictures of Ag NPs growing along the ripple axis (red bar) for increasing Ag deposition. (d,e,f) Pseudodielectric functions of the two optical axes (\perp & \parallel) for the samples corresponding to the SEM pictures. (g,h,i) $\tan\Psi$ at the IR region of the corresponding samples. | 70 |
| Figure 6.21: (a,b,c) $\tan\Psi$ of the two optical axes (\perp & \parallel) at the 4-MBN "fingerprint" region for the samples corresponding to the ones shown in Figure 6.20. | 71 |
| Figure 6.22: Polarization direction for sample rotation by 0° and 90° to the ripple direction. | 72 |
| Figure 6.23: Polarized IR spectra for sample positions 0° and 90° of unrippled (left) and rippled (right) substrate. | 73 |
| Figure 6.24: Polarized IR spectra for sample positions 0° and 90° of unrippled (left) and rippled (right) substrate. The spectra are coupled to show excitation at the same direction. | 74 |
| Figure 7.1: Spot-sizes of the combinatorial techniques used. The spots' diameters range from $250\ \mu\text{m}$ for ellipsometry, $160\ \mu\text{m}$ for IR to around $4\ \mu\text{m}$ for Raman and SEM. | 77 |
| Figure 7.2: (a) SEM pictures along the gradient thickness depicting the growth of silver islands. (b) imaginary part of the pseudodielectric function showing the progression of the plasmon resonance for increasing thickness in the UV-Visible. (c) IR range measured by reflectance IR. The blue and red coloring corresponds to the positions that exhibit maximum SERS and maximum SEIRA signals for 4-MBN. | 79 |
| Figure 7.3: SERS and SEIRA signal of the CN peak for increasing thickness positions on the line scan. | 80 |
| Figure 7.4: (a) The profile of SERS and SEIRA CN peak signal along the gradient thickness. (b) Fitted thickness of the Ag layer and the MSE of the fits according to Vis-ellipsometry measurements. | 82 |
| Figure 7.5: SERS CN vibration signal normalized to the signal in solution at different excitation wavelengths. . | 83 |
| Figure 7.6: (a) SEM pictures along the gradient thickness depicting the growth of silver islands along with (b) the corresponding Fourier transformations. (c) The imaginary part of the pseudodielectric function showing the progression of the plasmon resonance for increasing thickness in the UV-Visible and (d) IR range measured by reflectance IR. The blue and red coloring corresponds to the positions that exhibit maximum SERS and maximum SEIRA signals for the molecule 4-MBN. | 86 |
| Figure 7.7: SERS and SEIRA signal of the CN peak for increasing thickness positions on the line scan. | 87 |
| Figure 10.1: IR reflectance measurement of bulk evaporated Ag layer exhibiting Drude behavior. | 102 |
| Figure 10.2: Real part of the pseudodielectric function of positions with increasing Ag thickness, as shown in Figure 7.2. | 102 |
| Figure 10.3: Real (black line) and imaginary part (blue line) of the pseudodielectric function of a thick Ag layer. | 103 |
| Figure 10.4: Absolute height of SERS and SEIRA signal of the CN peak for increasing thickness positions on the line scan of a gradient Ag layer on rippled silicon substrate. | 103 |

Acknowledgments

First of all, I would like to thank my supervisors Prof. Dr. Norbert Esser and Prof. Dr. Peter Hildebrandt for entrusting me with this project. They gave me the freedom to make my own decisions, learn by trial and error but they were always there to put me into the right track whenever I got stuck. I am grateful for their kind support during these years. I had always the luck to have wonderful supervisors, and professors Esser and Hildebrandt affirmed my decision to work under them.

I extend my appreciation to Prof. Dr. Birgit Kanngießner and Prof. Dr. Janina Kneipp for accepting to act as chairwoman and examiner for the defense of the thesis.

Great acknowledgments to Dr. Tom Oates, who trained me into the research process and directed my enthusiasm with patience. I am grateful to PD Dr. Karsten Hinrichs that stepped in after Tom's leave. With his meticulous eye he sought to constantly improve me and his thoughtfulness guided me to the end of this project. Additionally, I thank him for performing the biaxial modeling of the ellipsometric measurements.

A great thank you as well to Prof. Dr. Inez Weidinger that found always time to listen to my experimental and theoretical difficulties and came up with inspired solutions for everything. I always enjoyed our lively discussions.

This whole project would not have been brought together without the help of the School of Analytical Sciences Adlershof. My appreciation to Prof. Dr. Kneipp, Prof. Dr. Panne, Ms. Schultens and the rest of SALSA staff that worked hard into bringing this school to existence. I feel blessed that I had the chance to be a part of this whole endeavor and help it grow, as also for having this unique opportunity to meet people from all over the world, make friends with them and expand my horizons on the diversity of cultures, yet the alikeness of the core human feelings.

I would like to give my thanks to my collaborators from the Ion Beam Center in Dresden, Dr. Facsco and Benjamin Schreiber for preparing rippled silicon templates for me as well as allowing me to prepare them on my own in their facilities. Also, thanks to Ulrich Gernert from the TUB ZELMI lab for allowing me to indulge in my love for Scanning Electron Microscopy.

I want to express my gratitude for my colleague Christoph Kratz, that we worked side by side since the beginning. He was always there to engage into scientific conversations and share his scientific knowledge as well as to offer experimental assistance. Through the contrast of his meticulous methods and my passionate chaotic ways, I believe we made a nice team. Likewise, thanks to Dr. Andreas Furchner, who apart from performing measurements with the IR ellipsometry setup for this thesis, he willingly assisted me whenever I met problems regarding ellipsometry and was there to answer all my questions. Thanks to Timur Shaykhutdinov for performing the Maxwell-solver calculations and the pleasant collaboration during the publications. To Kristina Lovrek for lighting up the office with her joyful spirits and Özgür Savvas for his kindness and assistance in technical and language matters. Thank you to Dr. Cordula Walder for the hard task of translating the abstract in German. Essentially I extend my gratitude to everybody from the scientific,

administration and technical part of ISAS, which during these years helped me understand and solve all kinds of situations or simply made working there a pleasant experience.

Accordingly, I want to extend my gratitude to the people from the Biophysical chemistry group in TU. To Dr. Ly for showing me the ropes of the Raman lab and performing the silver electrode measurements and Dr. Kozuch for his childlike enthusiastic, curiosity-driven approach to science. To Dr. Kuhlmann for keeping the lab up and running when everything went wrong. To Michael Stolarski for the 4-MBN vibrational calculations. Also, thanks to Sagie Katz and Patrycja Kielb for always being available to offer help on expense of their own lab time. Generally, I would like to extend my warm gratitude to all of the beautiful people constituting the Hilde-group (including the amazing Hilde-band), for creating this friendly and warm environment that made me feel like belonging in a family. A multiculti, patchwork family that treats its members with respect and love.

Talking about family, I am obliged to my parents for sacrificing themselves so that I could get a chance in education and therefore a chance to a better life. Thanks to my friends that managed not be annoyed by my constant complaining and always encouraged me. Last but not least, my warmest appreciation for Corinna Sauer for her patient, loving support and for continuing to believe in me even when I did not.

Ich bedanke mich herzlich!

Σας ευχαριστώ πολύ!

Statement of authorship

This doctoral thesis will be submitted for the degree of Doctor rerum naturalium (Dr. rer. nat.). I hereby certify that this thesis was composed by myself about my work during the doctoral research period. All the collaborations and support from agencies and people have been specifically acknowledged. All references supporting this work have been quoted properly. I promise that this thesis does not contain any work extracted from a thesis, or research paper previously presented for another doctoral degree at this or other universities. I have prepared this thesis specifically for the degree of Dr. rer. nat., under supervision of Prof. Dr. Norbert Esser at the Leibniz-Institut für Analytische Wissenschaften – ISAS – e. V. Berlin and of Prof. Dr. Peter Hildebrandt at the Physical Chemistry / Biophysical Chemistry Department of Technical University Berlin during the period of October 2013 to March 2017.